ADVANCED STEEL CONSTRUCTION

An International Journal

Volume 10 Number 2

June 2014

CONTENTS

Technical Papers

Website: *http://www.hkisc.org*
ISSN 1816-112X
Science Citation Index Expanded, Materials Science Citation Index and ISI Alerting

Cover: Flower Dome Conservatories @Gardens by The Bay, Singapore

ADVANCED STEEL CONSTRUCTION

VOL.10, NO.2 (2014)

ADVANCED STEEL CONSTRUCTION

an International Journal

ISSN 1816-112X

Volume 10 Number 2 *June 2014*

ADVANCED STEEL CONSTRUCTION
an international journal

ISSN 1816-112X

Science Citation Index Expanded, Materials Science Citation Index and ISI Alerting

Advanced Steel Construction
an international journal

Cover: Flower Dome Conservatories @Gardens by The Bay, Singapore
The two arch structures behind the big trees. Grand Award of IStructE-UK/Structural Division-HKIE 2013. Stability design by second-order direct analysis without effective length, jointly by The National University of Singapore and The Hong Kong Polytechnic University

General Information
Advanced Steel Construction, an international journal

Aims and scope

The International Journal of Advanced Steel Construction provides a platform for the publication and rapid dissemination of original and up-to-date research and technological developments in steel construction, design and analysis. Scope of research papers published in this journal includes but is not limited to theoretical and experimental research on elements, assemblages, systems, material, design philosophy and codification, standards, fabrication, projects of innovative nature and computer techniques. The journal is specifically tailored to channel the exchange of technological know-how between researchers and practitioners. Contributions from all aspects related to the recent developments of advanced steel construction are welcome.

Instructions to authors

Submission of the manuscript. Authors may submit double-spaced manuscripts preferably in MS Word by emailing to one of the chief editors as follows for arrangement of review. Alternatively papers can be submitted on a diskette to one of the chief editors.

Asian Pacific , African and organizing editor : Professor S.L. Chan, Email: ceslchan@polyu.edu.hk
American editor : Professor W.F. Chen, Email: waifah@hawaii.edu
European editor : Professor R. Zandonini, Email: riccardo_zandonini@ing.unitn.it

All manuscripts submitted to the journal are recommended to accompany with a list of four potential reviewers suggested by the author(s). This list should include the complete name, address, telephone and fax numbers, email address, and at least five keywords that identify the expertise of each reviewer. This scheme will improve the process of review.

Style of manuscript

General. Author(s) should provide full postal and email addresses and fax number for correspondence. The manuscript including abstract, keywords, references, figures and tables should be in English with pages numbered and typed with double line spacing on single side of A4 or letter-sized paper. The front page of the article should contain:

a) a short title (reflecting the content of the paper);
b) all the name(s) and postal and email addresses of author(s) specifying the author to whom correspondence and proofs should be sent;
c) an abstract of 100-200 words; and
d) 5 to 8 keywords.

The paper must contain an introduction and a conclusion. The length of paper should not exceed 25 journal pages (approximately 15,000 words equivalents).

Tables and figures. Tables and figures including photographs should be typed, numbered consecutively in Arabic numerals and with short titles. They should be referred in the text as Figure 1, Table 2, etc. Originally drawn figures and photographs should be provided in a form suitable for photographic reproduction and reduction in the journal.

Mathematical expressions and units. The Systeme Internationale (SI) should be followed whenever possible. The numbers identifying the displayed mathematical expression should be referred to in the text as Eq. (1), Eq. (2).

References. References to published literature should be referred in the text, in the order of citation with Arabic numerals, by the last name(s) of the author(s) (e.g. Zandonini and Zanon [3]) or if more than three authors (e.g. Zandonini et al. [4]). References should be in English with occasional allowance of 1-2 exceptional references in local languages and reflect the current state-of-technology. Journal titles should be abbreviated in the style of the Word List of Scientific Periodicals. References should be cited in the following style [1, 2, 3].

Journal: [1] Chen, W.F. and Kishi, N., "Semi-rigid Steel Beam-to-column Connections, Data Base and Modelling", Journal of Structural Engineering, ASCE, 1989, Vol. 115, No. 1, pp. 105-119.
Book: [2] Chan, S.L. and Chui, P.P.T., "Non-linear Static and Cyclic Analysis of Semi-rigid Steel Frames", Elsevier Science, 2000.
Proceedings: [3] Zandonini, R. and Zanon, P., "Experimental Analysis of Steel Beams with Semi-rigid Joints", Proceedings of International Conference on Advances in Steel Structures, Hong Kong, 1996, Vol. 1, pp. 356-364.

Proofs. Proof will be sent to the corresponding author to correct any typesetting errors. Alternations to the original manuscript at this stage will not be accepted. Proofs should be returned within 48 hours of receipt by Express Mail, Fax or Email.

Copyright. Submission of an article to "Advanced Steel Construction" implies that it presents the original and unpublished work, and not under consideration for publication nor published elsewhere. On acceptance of a manuscript submitted, the copyright thereof is transferred to the publisher by the Transfer of Copyright Agreement and upon the acceptance of publication for the papers, the corresponding author must sign the form for Transfer of Copyright.

Permission. Quoting from this journal is granted provided that the customary acknowledgement is given to the source.

Page charge and Reprints. There will be no page charges if the length of paper is within the limit of 25 journal pages. A total of 30 free offprints will be supplied free of charge to the corresponding author. Purchasing orders for additional offprints can be made on order forms which will be sent to the authors. These instructions can be obtained at the Hong Kong Institute of Steel Construction, Journal website: http://www.hkisc.org

The International Journal of Advanced Steel Construction is published quarterly by learnt society, The Hong Kong Institute of Steel Construction, c/o Department of Civil & Environmental Engineering, The Hong Kong Polytechnic University, Hung Hom, Kowloon, Hong Kong.

Subscription inquiries and change of address. Address all subscription inquiries and correspondence to Member Records, IJASC. Notify an address change as soon as possible. All communications should include both old and new addresses with zip codes and be accompanied by a mailing label from a recent issue. Allow six weeks for all changes to become effective.

The Hong Kong Institute of Steel Construction
HKISC
c/o Department of Civil and Environmental Engineering,
The Hong Kong Polytechnic University,
Hunghom, Kowloon, Hong Kong, China.
Tel: 852- 2766 6047 Fax: 852- 2334 6389
Email: *ceslchan@polyu.edu.hk* Website: *http://www.hkisc.org/*
ISSN 1816-112X
Science Citation Index Expanded, Materials Science Citation Index and ISI Alerting

ISSN 1816-112X

Science Citation Index Expanded, Materials Science Citation Index and ISI Alerting

Advanced Steel Construction
an international journal

VOLUME 10 NUMBER 2 JUNE 2014

Technical Papers

DESIGN OF PR FRAMES WITH TOP AND SEAT ANGLE CONNECTIONS USING THE DIRECT ANALYSIS METHOD

Rampal Singh[1] and Eric M. Lui[2,*]

[1] *Graduate Assistant*
[2] *Meredith Professor*
Department of Civil and Environmental Engineering, Syracuse University, Syracuse, NY 13244-1240, USA
**(Corresponding author: E-mail: emlui@syr.edu)*

Received: 9 August 2012; Revised: 2 February 2013; Accepted: 18 February 2013

ABSTRACT: Partially restrained (PR) connections are connections that possess stiffness and moment characteristics that fall between the extreme cases of pinned and rigid. This paper proposes a design methodology for PR frames that takes into consideration the semi-rigid nature of the connections, including their loading/unloading behavior under combined gravity and wind loads. Top and seat angle connections, modeled using the three-parameter power model, are used to demonstrate the proposed design procedure. To simply the design, two linearized connection stiffness values calculated on the basis of expected connection loads are used. The analysis is carried out using the American Institute of Steel Construction (AISC) direct analysis method in which notional horizontal loads, expressed as a fraction of the gravity load, are applied to the PR frames in conjunction with the use of reduced member axial and bending stiffness. Examples are given to demonstrate the validity of the proposed method of PR frame design.
Keywords: Partially restrained frames, Top and seat angle connections, Direct analysis method, Steel structures, Design and analysis

1. INTRODUCTION

Connections are important structural elements in a frame structure. The behavior of the frame is very much affected by the types of connections used. If the connection possesses sufficient strength and stiffness, full continuity between the connected elements can be assumed for analysis and design. However, if either the connection strength or stiffness falls short of what is assumed, allowances must be made in the analysis and design processes to ensure that the frame will behave as expected. In a conventional analysis and design of steel frames, a simplifying assumption that the beam-to-column connections are either fully rigid or ideally pinned is often used. The rigid joint assumption implies that full slope continuity exists between the adjoining members, which means the angle between the beam and column remains more or less unchanged as the frame deforms; and the full or a substantial amount of moments is transferred between the beam and the column. On the other extreme, the assumption of an ideally pinned connection implies that no or very little moment will be transmitted between the beam and the column and as far as rotation is concerned the beam and column will behave independently.

Although the use of these idealized joint bebavior drastically simplifies the analysis and design procedures, the validity of these assumptions becomes questionable for cases in which the rigidity of connections, which can be considered as the slope of the relation between the connection moment M and the connection relative rotation θ, is intermediate between the fully rigid and ideally pinned cases. These connections, referred to as semi-rigid or partially restrained (PR) connections, have been the subject of research for many years, and various researchers have proposed analysis and design methods for frames that utilize these PR connections (Ang and Morris [1], Lui and Chen [2,3,4], Chen [5], Cunningham [6], Wu and Chen [7], Barakat and Chen [8,9], Hsieh and Deierlein[10], Lui [11], Xu [12], Surovek et al. [13]). Detailed summaries of research on PR connections and frames can be found in a number of books and monographs such as those by Narayanan [14], Lorenz et al. [15], Chen et al. [16], Bjorhovde et al. [17], Chan and Chui [18], Chen [19], Faella et al. [20], Chen et al. [21], etc., and will not be repeated here.

According to the American Institute of Steel Construction (AISC [22]) specification, a connection is considered to be a PR connection if its secant stiffness under service load R_{ks} falls in the range $2EI/L < R_{ks} < 20EI/L$, where EI and L are the flexural rigidity and the length of the adjoining beam, respectively. Despite acknowledging the existence of PR connections in frame structures and suggesting that the relevant response characteristics of PR connections must be included in the analysis of the structure for member and connection forces, displacements and frame stability, no recommendations are currently given in the AISC specification on how these PR frames should be designed. In addition, for the first time AISC is espousing the direct analysis method as the main design method for stability, while the commonly-used effective length method, first-order analysis method, and approximate second-order analysis using moment magnification (B_1, B_2) factors have been relegated to the appendix. It is therefore the objective of this paper to propose a design method for PR frames using the direct analysis approach.

2. CONNECTION TYPES, CLASSIFICATIONS AND BEHAVIOR

There are various means by which connections can be classified. For instance, they can be classified by the connecting medium used, e.g., bolted versus welded connections. They can also be classified by their functionality, e.g., beam-to-column connections, hanger connections, bracing connections, truss connections, etc.; or by the type of internal forces/moment that will be transmitted, e.g., shear versus moment connections; or by the types and geometries of connection elements used, e.g., single plate connections, double web angle connections, top and seat angle connections, flange-angle connections, end plate connections, flange-plated connections, etc. Regardless of how connections are classified, the behavior of connections is often described by their moment-rotation (M-θ) response as shown in Figure 1. Although connections do experience axial, shear and torsional deformations, they are usually small compared to the rotational deformation. Consequently, researchers often consider only the connection's rotational deformation in assessing frame response. Aside from a few exceptions (Cerfontaine and Jaspart [23], Urbonas and Daniunas [24,25]), almost all experiments on connections conducted in the past few decades have focused primarily on their flexural response, and over the years several connection database and various connection models have been developed for general use (Frye and Morris [26], Goverdhan [27], Ang and Morris [1], Nethercot [28], Kishi and Chen [29], Chen and Kishi [30], Chen et al. [21]). From these database, it can be observed that (1) almost all types of connections exhibit a M-θ behavior that falls between the extreme cases of ideally pinned and fully rigid conditions, (2) except for small values of moment the M-θ relationships are typically nonlinear over a large range of loading, and (3) the maximum moment a connection can transmit often decreases with the more flexible connection (i.e., there is a correlation between strength and stiffness).

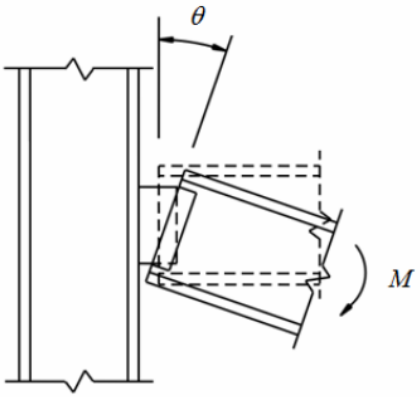

Figure 1. Flexural (or Rotational) Deformation of a PR Connection under a Moment

Because of the above observations, connections can also be classified according to their stiffness or strength (see for example Bjorhovde et al. [31], Eurocode 3 [32], Nethercot et al. [33], AISC [22]). Since the AISC direct analysis procedure will be used, the AISC connection classification scheme will be adopted for the present study. For a connection to be classified as a PR connection, its secant stiffness R_{ks} under service load (i.e., the slope of a straight line drawn from the origin to the moment Ms under service load condition as shown in Figure 2) falls in the range $2EI/L < R_{ks} < 20EI/L$, where EI and L are the flexural rigidity and the length of the beam, respectively. In terms of strength, a PR connection should be able to transmit at least 20% of the full plastic moment of the beam when it is experiencing a rotation $\theta = 0.02$ radian. Furthermore, it should possess sufficient rotational capacity so that θ_u, defined as the connection rotation where its strength has dropped to 80% of its peak value as shown in Figure 2 or a rotational deformation equal to 0.03 radian if the connection experiences little or no loss in strength, will exceed what is required for design at the strength limit state.

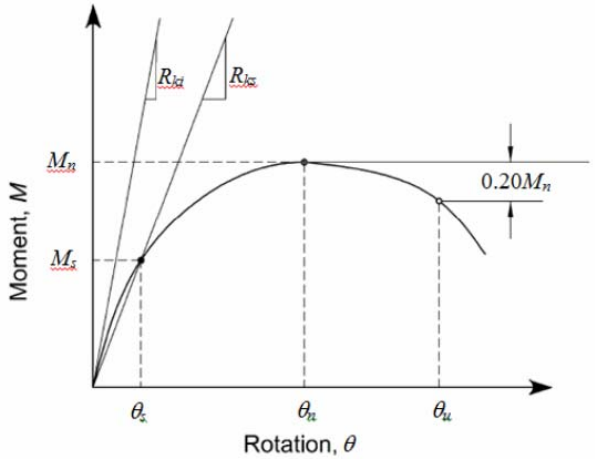

Figure 2. Moment-rotation Response of a PR Connection

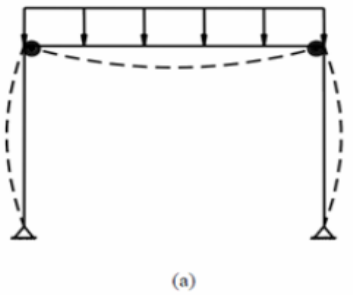

(a)

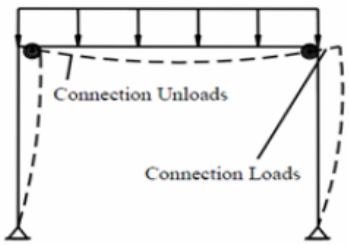

(b)

Figure 3. Loading/Unloading Behavior of PR Connections –
(a) Both Connections Load under Gravity Load,
(b) Windward Connection Unloads while Leeward Connection Loads under Wind Load

Another aspect of PR connections that needs to be addressed is their loading/unloading response to load sequencing. With reference to Figure 3 in which a simple portal frame is shown with PR connections present at both beam-column joints. When the gravity load is applied, both connections undergo loading. However, when a lateral load such as wind is applied, the windward connection will experience unloading while the leeward connection will continue to undergo loading. Depending on the difference between the loading and unloading stiffness, the forces and moments developed in the frame can be quite different. The design procedure for PR frame to be discussed in a later section will account for this connection loading/unloading response.

3. CONNECTION MODEL

Almost all M-θ data for PR connections are obtained from laboratory tests. These test data are then curve-fitted to provide empirical equations for use in analysis and design. Many such equations in the form of linear, bilinear, trilinear, polynomial, spline, exponential, and power functions have been proposed (Frye and Morris [26], Goverdhan [27], Ang and Morris [1], Nethercot [28], Kishi and Chen [29], Chen and Lui [34]), and computer programs (PRCONN [35], Chen and Toma [36], Chen et al. [21]) are available from which information on a number of PR connection types can be retrieved. In the present study, the three-parameter power model (Kishi et al. [37,38], Kishi and Chen [39]) for connections made from angle sections will be used. In this model the initial connection stiffness R_{ki} and ultimate moment capacity M_{ult} of the connections were determined using mechanistic models. Using these two quantities plus a curve-fitting shape factor n, the experimental data were represented by an equation in the form (Richard and Abbott [40])

$$M = \frac{R_{ki}\theta}{\left[1+\left(\frac{\theta}{\theta_o}\right)^n\right]^{1/n}} \tag{1}$$

where

R_{ki} = initial connection stiffness
n = shape factor
θ_o = reference plastic rotation, calculated as $\theta_o = M_{ult}/R_{ki}$
M_{ult} = ultimate moment capacity of the connection

As shown in Figure 4, the shape factor n defines the shape of the M-θ curve for a given set of R_{ki} and M_{ult} values.

Equations for R_{ki}, M_{ult} and n for connections made from angle sections have been derived (Kishi et al. [41]). With reference to a typical connection angle shown in Figure 5, if we define

g_c = distance between heel of angle to center of first line of fasteners
k = gauge distance from heel of angle to top of fillet
t = angle thickness
W = nut width

and denote

d =beam depth
l = angle length
$I_o = t^3/12$ = geometrical moment of inertia
$M_o = \sigma_y t^2/4$ = moment per unit length of angle
σ_y = yield stress of angle

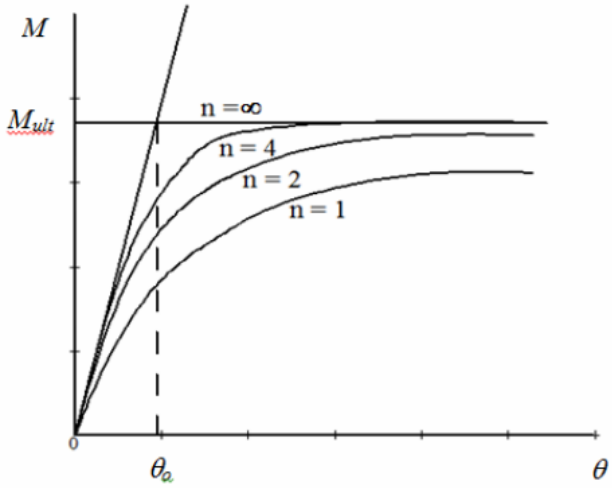

Figure 4. Three-parameter Power Connection Model

as well as with the use of the following non-dimensional parameters

$$\beta = g_c/l, \qquad \gamma=l/t, \qquad \delta=d/t, \qquad \kappa=k/t, \qquad \omega=W/t, \qquad \rho=t_w/t_t \tag{2a-f}$$

where subscripts t and w denote the top angle and the web angle, respectively, the equations for the three parameters R_{ki}, M_{ult} and n are given as follows.

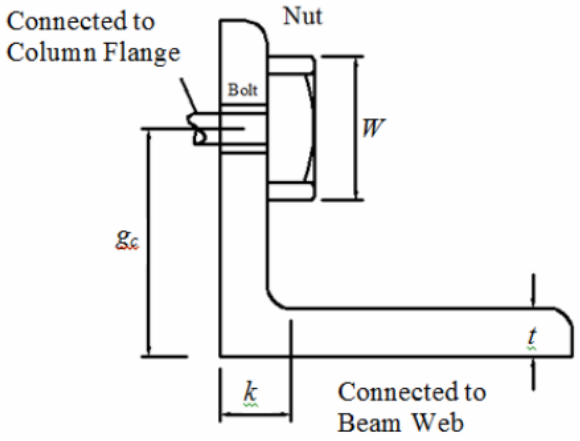

Figure 5. Symbols used for an Angle Connection

3.1 Initial Connection Stiffness R_{ki}

The equation for the initial connection stiffness is

$$\frac{R_{ki}}{EI_{ot}} = \frac{R_{kits}}{EI_{ot}} + \frac{R_{kiw}}{EI_{ot}} \tag{3}$$

where R_{kits}/EI_{ot} and R_{kiw}/EI_{ot} are the non-dimensional top and seat angle and web angle stiffness contributions to the initial connection stiffness, respectively. They are given by

$$\frac{R_{kits}}{EI_{ot}} = \frac{3(1+\delta_t)^2}{\beta_t'[\gamma_t^2(\beta_t')^2 + 0.78]} \tag{4}$$

$$\frac{R_{kiw}}{EI_{ot}} = \frac{3\rho(1+\delta_t)^2}{2\beta_w^{'}[\gamma_w^2(\beta_w^{'})^2 + 0.78]} \tag{5}$$

in which

$$EI_{ot} = 29000 \cdot \frac{t_t^3}{12} \tag{6}$$

$$\beta_t^{'} = \beta_t - \frac{1}{2\gamma_t}\ 1 + ?\omega_t \tag{7}$$

$$\beta_w^{'} = \beta_w - \frac{1}{2\gamma_w}\ 1 + ?\omega_w \tag{8}$$

3.2 Ultimate Connection Moment Capacity M_{ult}

The equation for the ultimate connection moment capacity is

$$\frac{M_{ult}}{M_{ot}t_t} = \frac{M_{uts}}{M_{ot}t_t} + \frac{M_{uw}}{M_{ot}t_t} \tag{9}$$

where $M_{uts}/M_{ot}t_t$ and $M_{uw}/M_{ot}t_t$ are the top and seat angle and web angle moment contributions to the ultimate connection moment capacity, respectively. They are given by

$$\frac{M_{uts}}{M_{ot}t_t} = \gamma_t \left\{1 + \xi_t \left[1 + \beta_t^* + 2(\kappa_t + \delta_t)\right]\right\} \tag{10}$$

$$\frac{M_{uw}}{M_{ot}t_t} = \gamma_w(1+\xi_w)\rho^3 \left[\frac{\gamma_w(\xi_w - 1)}{3(\xi_w + 1)} + \delta_w + \frac{1}{\rho}\right] \tag{11}$$

where

$$M_{ot} = \frac{\sigma_y t_t^2}{4} \tag{12}$$

and ξ_t and ξ_w are to be evaluated from the following fourth-order equations

$$\xi_t^4 + \beta_t^* \xi_t - 1 = 0 \tag{13}$$

$$\xi_w^4 + \beta_w^* \xi_w - 1 = 0 \tag{14}$$

where

$$\beta_t^* = \beta_t^{'}\gamma_t - \kappa_t \tag{15}$$

$$\beta_w^* = \beta_w \gamma_w - \kappa_w \tag{16}$$

with $\beta_t^{'}$ computed from Eq. 7.

It should be noted that even though Eqs. 3 and 9 were derived for top and seat angle connections with double web angles, they can be simplified for top and seat angles without the web angles by setting the second term equal zero, or for double web angle connections by setting the first term equal zero, or for single web angle connections by setting the first term equal zero and dividing the second term by 2.

3.3 Shape Parameter *n*

The equations for the shape parameter are given as follows.

For top and seat angle connections with the web angles:

$$n = 1.398 \log_{10} \theta_o + 4.631 \geq 0.827 \quad (17a)$$

For top and seat angle connections without the web angles:

$$n = 2.003 \log_{10} \theta_o + 6.070 \geq 0.302 \quad (17b)$$

For double web angle connections:

$$n = 1.322 \log_{10} \theta_o + 3.952 \geq 0.573 \quad (17c)$$

For single web angle connections:

$$n = 0.520 \log_{10} \theta_o + 2.291 \geq 0.695 \quad (17d)$$

Because of some uncertainties in test setups and data collections, the loss of accuracy during the curve-fitting process, and the unavoidable variability of one connection to another, a resistance factor of 0.9 as recommended by Christopher and Bjorhovde [42] will be used in the proposed method of PR frame design.

4. AISC DIRECT ANALYSIS METHOD

The direct analysis method is a method recommended by AISC for use in the stability analysis and design of frame structures. It has the following features:

1. A second-order elastic analysis that explicitly accounts for the P-δ and P-Δ effects is to be used to determine the required strengths. However, it is permissible to neglect the P-δ effect in the analysis (but not in design) if (a) the gravity loads are supported primarily by nominally vertical columns, walls or frames, (b) the ratio of maximum second-order drift to first-order drift both calculated using adjusted stiffness (see Items 3 and 4 below) for all stories is ≤ 1.7, and (c) no more than one-third of the total gravity loads on the structure is supported by columns that are part of the moment-resisting frame in the direction of translation being considered. In lieu of a second-order analysis, the use of a first-order analysis in conjunction with the use of moment magnification (i.e., B_1 and B_2) factors is permitted.
2. The effect of initial imperfections in the form of column out-of-plumbness is to be considered in the analysis by including them directly in the structural model. The magnitude of the initial displacements shall be the maximum amount considered in the design, and the pattern of initial displacements shall be such that it provides the greatest destabilizing effect. Alternatively, for structures that support gravity loads primarily through nominally vertical columns, walls or frames, the effect of initial imperfections can be represented using notional loads. In this approach, notional lateral loads of magnitude $0.002\sum P_i$ (where $\sum P_i$ is the factored gravity loads acting on story i) distributed over the story

in the same proportion as the gravity loads are to be applied to the story for all gravity-only load combinations. However, for frames where the ratio of second-order to first-order drift (both computed using the adjusted stiffness discussed in Items 3 and 4 below) exceeds 1.7, these notional lateral loads have to be applied to *all* load combinations in the analysis.

3. A reduced stiffness equal to $0.8E$ is to be used for members whose flexural or axial stiffness is considered to contribute to the lateral stability of the frame. Conservatively, the use of $0.8E$ for *all* members is permitted. This stiffness reduction is used to account for the effects of member imperfections and inelasticity, as well as uncertainty in determining the member strength and stiffness.
4. If $P_u/P_y>0.5$ (where P_u is the required axial compressive strength and $P_y = F_yA$ is the yield load), a second stiffness reduction factor, $\tau = 4(P_u/P_y)[1-(P_u/P_y)]$ is to be applied to the moment of inertia I of all flexural members that contribute to the lateral stiffness of the frame. In lieu of using τ, an increase of the notional from $0.002\sum P_i$ to $0.003\sum P_i$ can be used in all load combinations.
5. Regardless of the end conditions of the member, an effective length factor of $K=1$ is to be used to compute the design compressive strength P_n of the member.

5. PROPOSED PR FRAME DESIGN APPROACH

The steps proposed for the design or PR frames are as follows:

1. For each semi-rigid connection, assume a value of $\overline{R}_k = R_{kb}L/EI$, where R_{kb} is the effective linearized connection stiffness under factored gravity loads. It is obtained as the slope of a line drawn from the origin to the intersection point of the PR connection M-θ curve and a beam line (see Figure 6). The beam line is defined by the equation

$$M = \frac{w_u L^2}{12} - \frac{2EI}{L}\theta \tag{18}$$

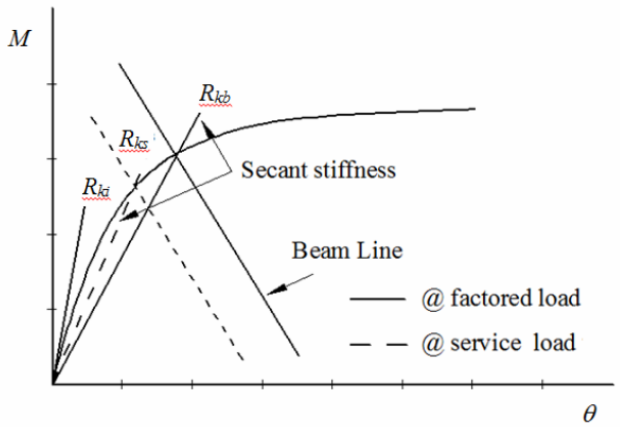

Figure 6. Determination of R_{kb}

where w_u is the uniform factored gravity load on the beam. The above equation relates the end moment M and rotation θ of a prismatic beam subject to a uniformly distributed load applied over its entire length. Note that if the connection is fully-rigid, $\theta=0$ and so $M=w_uL^2/12$, which is the fixed-end moment of the beam. On the other hand, if the connection is ideally-pinned, $M=0$ and so $\theta=w_uL^3/24EI$, which is the end rotation of a simply-supported beam.

2. Calculate the beam moments M_{neg} and M_{pos} for the assumed value of $\overline{R}_k$ using the following equations (Chen and Lui [34]).

$$M_{neg} = \frac{2\overline{R}_{kb}}{3(\overline{R}_{kb}+2)} M_{ss} \tag{19}$$

$$M_{pos} = \frac{\overline{R}_{kb}+6}{3(\overline{R}_{kb}+2)} M_{ss} \tag{20}$$

where $M_{ss} = w_u L^2/8$ is the uniformly loaded simply-supported beam moment.

3. Select trial beam section based on the calculated M_{pos} and M_{neg} values.
4. Select the type of connection (e.g., a top and seat angle connection with double web angles) and choose a family of connections (3 to 4 etc.) as trials.
5. Determine the M-θ curve parameters (M_{ult}, R_{ki}, and n) for each connection using the procedure outlined in Section 3.
6. Construct a family of M-θ curves using Eq. 1, and superimpose on them a beam-line computed using Eq. (18)
7. Select an appropriate connection by determining the R_{kb} values for the family of connections and choose the one that has a $\overline{R}_k$ (= $R_{kb}L/EI$) value closest to the one assumed in Step 1.
8. Determine R_{ks} as shown in Figure 6 and calculate $R_{ks}L/EI$ for the selected connection at service load to check that it falls in the PR connection range of $2 < R_{ks}L/EI < 20$.
9. Select the trial column section based on the factored axial load and moment.
10. For unbraced frames, calculate the loading stiffness R_{kL} using the equation

$$R_{kL} = \frac{M_n - M_g}{\theta_n - \theta_g} \tag{21}$$

where, in reference to Figure 7, M_n is the nominal moment strength of the connection that corresponds to θ_n = 0.02 radian (AISC [22]) denoted as point b in the figure, and M_g and θ_g are the moment and rotation of the connection under factored gravity loads denoted as point a.

11. Analyze the PR frame using the appropriate connection stiffness R_{kb}, R_{kL} or R_{ki} in conjunction with the Direct Analysis Method for the two cases described below.

<u>Case 1, the non-sway frame condition for gravity load combinations only:</u>

Element Stiffness - Column: $EI_e = 0.8\tau EI$
- Beams: $EI_e = 0.8EI$
- Connections: $R_k = 0.9R_{kb}$

Applied Loads - gravity load combinations, plus a notional load of $0.002P_i$ applied to each column at each floor level.

- Perform a *second-order elastic analysis* to determine the internal forces.
- Check the beam-column, beam, and connection strength.
- If the above conditions are satisfied, proceed further. Otherwise, revise the sections and/or connections until the conditions are satisfied.

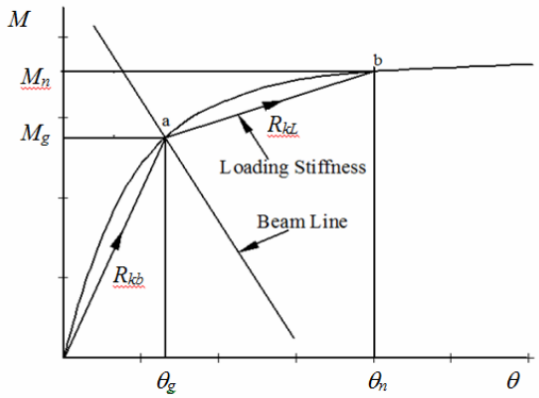

Figure 7. Determination of R_{kL}

Case 2, the sway frame condition for gravity + lateral load combinations:
Step 1 - Gravity load step:

Element Stiffness - Column: $EI_e=0.8\tau EI$
- Beams: $EI_e=0.8EI$
- Connections: $R_k = 0.9R_{kb}$

Applied Loads - Factored gravity loads only without any notional loads

- Perform a *second-order elastic analysis* to determine the internal forces due to the applied loads.

Step 2 - Lateral load step:

Element Stiffness - Column: $EI_e=0.8\tau EI$
- Beams: $EI_e=0.8EI$
- Connections: $R_k = 0.9R_{ki}$(Windward Side)
$R_k = 0.9R_{kL}$ (Leeward Side)

Applied Loads - Concentrated vertical loads applied at beam-column joints producing the column axial forces associated with *Step 1*
- Lateral load combinations plus a notional load of $0.002P_i$applied to each column at each floor level

- Perform a *second-order elastic analysis* to determine the internal forces due to above applied loads
- Superimpose the moments from the gravity (step 1) and lateral (step 2) load steps. Check the beam-column, beam and connection strengths. If not satisfied, revise the sections and/or connections of the structure.

6. DESIGN EXAMPLES

In this section, design examples will be given to show how the proposed PR frame design procedure presented in the preceding section can be applied. The second-order analysis is performed using the software MASTAN2 (McGuire et al. [43]).

The first example (a portal frame) is used to demonstrate the basic loading/unloading behavior of PR connections in an unbraced frame when one end of a beam/girder is connected to a single column. It also serves to show the effect of PR connections on the columns. The second example (a 2-story unbraced frame) is used to demonstrate how the moments can be distributed to the columns above and below the beam to which the columns are attached. In both examples, only top and seat angle with double web angle connections will be considered. This is because the normalized stiffness $\overline{R}_k$ for this type of connections often falls in the semi-rigid range of $2 < \overline{R}_k < 20$, and so they are commonly used in PR frames. In addition, the following assumptions have been used:

- All beam sections are compact (i.e., the sections are capable of developing the full plastic moment)
- All column sections are non-slender elements (i.e., local buckling is not of concern)
- All sections are oriented with their webs in the plane of the applied loads
- The frames are braced against out-of-plane deflection at the beam-column joints only
- The beams are non-composite (i.e., they are not connected to a concrete slab)
- Wind loads are applied as concentrated loads at windward beam-column joints.
- All beam-column connections satisfy the AISC connection design requirements
- All beam and column sections are W-shapes made from A992 steel with F_y = 50 ksi (345 MPa) and E = 29000 ksi (200 GPa).

Example 1 – Design of a PR Portal Frame

The PR frame shown in Figure 8 is to be designed. The frame is subjected to the loads shown. Beam deflection under service live load is limited to $L/360$, where L is the beam length; and frame drift should not exceed $H/200$, where H is the story height. To start the design, assume $\overline{R}_k = 6$ for the connections.

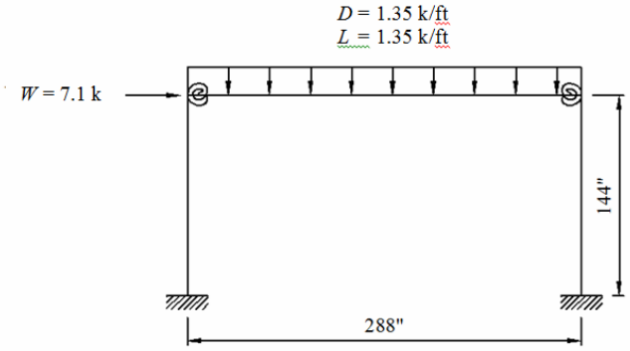

Figure 8. An Unbraced Portal PR Frame (1 k = 4.45 kN, 1 ft = 12” = 0.305 m)

Solution:

Load Combinations: The load combinations (AISC [22], ASCE [44]) that most likely will control the design are given in Table 1.

Table 1. Applied loads (1 k/in. = 175 kN/m, 1 kip = 4.45 kN)

Load Case	Load Combinations	w_u (k/in.) (Gravity)	p_u (kips) (Lateral)
1	$1.2D + 1.6L$	0.315	-
2	$1.2D + 0.5L + 1.0W$	0.191	7.1

Beam Section Selection: For load case 1, the frame does not undergo any sidesway movement. Use Eqs. (19) and (20) with the assumed $\overline{R}_k = 6$ to estimate M_{neg} and M_{pos} for the preliminary sizing of the beam.

$$M_{neg} = \frac{2\overline{R}_{kb}}{3(\overline{R}_{kb}+2)} M_{ss} = 1633 \text{ k-in.}$$

$$M_{pos} = \frac{\overline{R}_{kb}+6}{3(\overline{R}_{kb}+2)} M_{ss} = 1633 \text{ k-in.}$$

Using these moments as a guide, a W14×53 is selected as the trial section. The flexural capacity $\phi_b M_n$ of this section is 2462 k-in. (278 kN-m), which exceeds the required flexural strength M_u (= M_{neg} or M_{pos}) = 1633 k-in. (185 kN-m).

Connection Selection: If top and seat angle with double web angle connections are to be used for the PR frame, a possible set of candidate connections are summarized in Table 2. In the table, the thickness of the top and seat angle is denoted as C (5/8), C (3/4), etc.

Table 2. Details of PR Connections (1 in. = 25.4 mm)

Connection	**Bolt diameter** d (in.)	**Nut Width** W (in.)	**Top and Seat Angles** 2L6 × 4 × t_t				**Web Angles** 2L4 × 3.5 × ½		
			t_t (in.)	l_t (in.)	g_{ct} (in.)	k_t (in.)	l_w (in.)	g_{cw} (in.)	k_w (in.)
C (5/8)	7/8	1-7/16	5/8	7	3	1-1/8	8	3	11/16
C (3/4)	7/8	1-7/16	¾	7	3	1-1/4	8	3	11/16
C (7/8)	7/8	1-7/16	7/8	7	3	1-3/8	8	3	11/16

Calculations for R_{ki}, M_{ult}, and n: Using the above angle data and Eqs. (3), (9) and (17a), the three connection parameters are calculated and summarized in Table 3.

Table 3. Connection Parameters (1 k-in. = 0.113 kN-m)

Connection	R_{ki} **(×10³)** (k-in./rad)	M_{ult} (k-in.)	n
C (5/8)	411	1907	1.37
C (3/4)	690	2435	1.20
C (7/8)	1112	2973	1.03

Beam-Line Diagrams with M-θ Curves: The intersection of the M-θ curve and the beam line represents the expected connection moment and deformation under gravity loads. Using Eq. (1) for the M-θ curves and Eq. (18) for the beam lines, one can generate Figure 9 for the three connections and the two load cases given in Table 1. The beam lines for the two load cases are labeled (BL-LC(I) and BL-LC(II), respectively, in the figure. From this figure, R_{kb} for each connection can be determined as the slope of a line drawn from the origin to the intersection point of the connection's M-θ curve and the respective beam line. The calculated secant stiffness for each connection under Load Case 1 R_{kb1} is given in Table 4.

Table 4. Connection Stiffness (1 k-in. = 0.113 kN-m)

Connection	**Connection Stiffness, R_{kb1} ($\times 10^3$)** (k-in./rad)	$\bar{R}_k = R_{kb1}L/EI$
C (5/8)	435	8
C (3/4)	314	5.8
C (7/8)	202	3.7

Connection C (3/4) is selected because its $\bar{R}_k$ value is closest to the initially assumed value of 6. Once the connection has been selected, its $R_{ks}$and R_{kL} values can now be determined. By subjecting the frame to the service gravity load (D+L), $R_{ks}L/EI$ is computed to be 7.51, which falls in the PR connection range. From Figure 9, the design strength ($\phi_b M_{n\,(0.02\ \text{rad})}$) of the connection is determined to be 1987 k-in. (225 kN-m). Using the data presented in Figure 9 and the schematics shown in Figure 7, R_{kb} and R_{kL} for the two load cases are computed and given in Table 5.

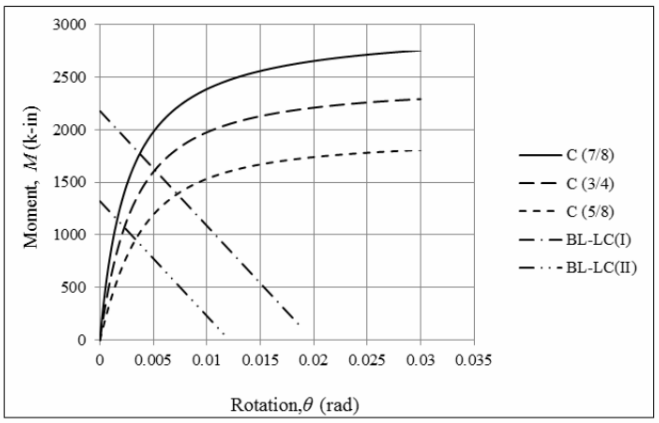

Figure 9.M-θ curves and beam lines (1 k-in. = 0.113 kN-m)

Table 5. Linearized Connection Stiffness (1 k-in./rad = 0.113 kN-m/rad)

Beam Line for Load Case (BL-LC)	**Linearized Connection Stiffness**	
	R_{kb} ($\times 10^3$) (k-in./rad)	**R_{kL} ($\times 10^3$)** (k-in./rad)
1	314	-
2	467	64

Column Section Selection: A W10×33 section is selected based on the axial load (P_u) and moment (M_{neg}) acting on the beam-column joint due to load case 1. A 12-ft long W10x33 section has an axial capacity ($\phi_c P_n$) of 292 kips (1300 kN) and bending moment capacity ($\phi_b M_n$) of 1530 k-in. (173 kN-m).

Applying the Direct Analysis Approach: The analysis is carried out for the non-sway and sway frame conditions as outlined in Section 5.

Case 1 – the non-sway frame condition for gravity loads only

The parameters used for this analysis are summarized in Table 6.

Table 6. Case 1 Analysis Parameters (1 k = 4.45 kN, 1 in. = 25.4 mm)

Element Stiffness			**Applied Loads**	
Columns $EI_e=0.8\tau EI$ (k-in.^{2})	**Beams** $EI_e=0.8EI$ (k-in.^{2})	**Connections** $0.9R_{kb1}$ (k-in./rad)	**Load** $1.2D+1.6L$ (k/in.)	**Notional Load** $0.002P_i$ (kips)
3.97×10^6	12.6×10^6	282×10^3	0.315	0.091

(τ is taken as 1 since the axial load P_u in each column for this load case is less than $0.5P_y$.)

Using the above parameters, a second-order elastic analysis is performed to determine the internal forces in each member. The results are shown in Table 7. Also shown in the table are the results obtained from a 2nd-order inelastic analysis (i.e., instead of using the direct analysis approach outlined in Section 4, the frame is analyzed using 2nd-order inelastic analysis technique) as well as the results of the unity check obtained using the appropriate beam-column interaction (H1-1a or H1-1b) or beam equation given in AISC [22]. The unity check is satisfied if the value computed is <1. As can be seen, the results obtained using the direct analysis approach is slightly conservative when compared to those obtained from a 2nd-order inelastic analysis.

Table 7. Analysis Results for Case 1 with Unity Check (1 kip = 4.45 kN, 1 k-in. = 0.113 kN-m)

Case 1						
Element	**Axial Force** (kips)		**Moment** (k-in.)		**Unity Check**	
	Proposed Method	2nd-order Inelastic Analysis	Proposed Method	2nd-order Inelastic Analysis	Proposed Method	2nd-order Inelastic Analysis
Left Column	45.3	45.3	1029	992	0.75	0.73
Right Column	45.4	45.4	1040	1004	0.76	0.73
Beam	-	-	2246	2280	0.91	0.93

Case 2 – the sway frame condition for gravity + wind loads

The analysis parameters for this load case are given below.

(i) Gravity load step: $1.2D+0.5L$ (see Table 8)

Table 8. Case 2 Gravity Load Analysis Parameters (1 k = 4.45 kN, 1 in. = 25.4 mm)

Element Stiffness			**Applied Loads**	
Columns $EI_e=0.8\tau EI$ (k-in.^{2})	**Beams** $EI_e=0.8EI$ (k-in.^{2})	**Connections** $0.9R_{kb2}$ (k-in./rad)	**Loads** $1.2D+0.5L$ (k/in.)	**Notional Load** $0.002P_i$ (kips)
3.97×10^6	12.6×10^6	420×10^3	0.191	n.a

(ii) Lateral load step: $1.0W$ (see Table 9)

Table 9. Case 2 Lateral Load Analysis Parameters (1 k = 4.45 kN, 1 in = 25.4 mm)

Element Stiffness				**Applied Loads**		
Column $EI_e=0.8\tau EI$ (k-in.^{2})	**Beam** $EI_e=0.8EI$ (k-in.^{2})	**Connections**		**Loads**		**Notional Load** $0.002P_i$ (kips)
		$0.9R_{ki}$ (k-in./rad)	$0.9R_{kL}$ (k-in./rad)	Column Load (kips)	Wind $1.0W$ (kips)	
3.97×10^6	12.6×10^6	621×10^3	58×10^3	27.5	7.1	0.055

Using the analysis parameters given in Tables 8 and 9, a second-order elastic analysis is performed individually for each load step to determine the internal forces in the structure. The results from these two analyses are then superimposed and presented in Table 10. Note that while the final moments are determined by superimposing the moment results from both the gravity and gravity+wind load steps, the final axial loads are determined only from the gravity+wind load step because the axial load effect from the gravity load step is already accounted for by subjecting the columns to the concentrated joint loads. Note also that the notional loads (representing non-verticality) are only applied in the gravity+wind load step to ensure that the second-order effects associated with the non-verticality are accounted for only once. Also shown in the table are results from a 2nd-order inelastic analysis and results of the unity check.

Table 10. Analysis Results for Case 2 with Unity Check (1 kip = 4.45 kN, 1 k-in. = 0.113 kN-m)

Case 2						
Element	**Axial Force** (kips)		**Moment** (k-in.)		**Unity Check**	
	Proposed Method	2nd-order Inelastic Analysis	Proposed Method	2nd-order Inelastic Analysis	Proposed Method	2nd-order Inelastic Analysis
Left Column	26	26	404	392	0.33	0.3
Right Column	29	29	809	778	0.57	0.56
Beam	-	-	1382	1406	0.56	0.57

Finally, the service live load deflection of the beam and the wind drift of the frame are calculated to be 0.41 in. (10.4 mm) and 0.32 in. (8.1 mm), respectively. Since they are less than the allowable values of $L/360$ = 0.8 in. (20.3 mm) and $H/200$ = 0.72 in. (18.3 mm), the design is considered satisfactory.

Example 2 - Design of a Two-Story Unbraced PR Frame

The PR frame subjected to the applied loads shown in Figure 10 is to be designed. The live load beam deflection and the wind induced interstory frame drift are to be limited to $L/360$ and $H/200$, respectively. To start the design, assume $\overline{R}_k$ = 8 and 10 for the 1st and 2nd story connections, respectively.

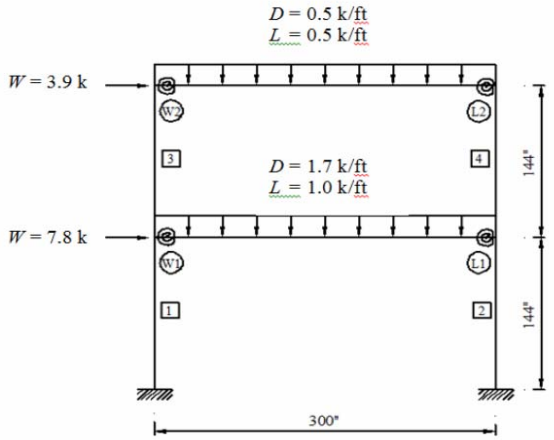

Figure 10. A Two-story Unbraced PR Frame (1 k = 4.45 kN, 1 ft = 12" = 0.305 m)

Solution:

The load combinations used for the design are given in Table 11. By using Load Case 1, Eqs. 19 and 20, and the assumed $\overline{R}_k$ values, M_{neg} and M_{pos} are calculated and shown in Table 12. From these moment values, a W12×50 section ($\phi_b M_n$=1903 k-in. or 215 kN-m) and a W10×33 section ($\phi_b M_n$=912 k-in. or 103 kN-m) are selected for the beams of the first and second stories, respectively.

Table 11. Applied Loads (1 k/in. = 175 kN/m, 1 kip = 4.45 kN)

Load Case	**Load Combinations**	w_{u1} (k/in.) **(Gravity)**	w_{u2} (k/in.) **(Gravity)**	p_{u1} (kips) **(Lateral)**	p_{u2} (kips) **(Lateral)**
1	$1.2D + 1.6L$	0.303	0.117	-	-
2	$1.2D + 0.5L + 1.0W$	0.212	0.071	7.8	3.9

Table 12. Non-sway Beam Moments for Beam Section Selection (1 k-in. = 0.113 kN-m)

Story	M_{neg} (k-in.)	M_{pos} (k-in.)
1st	1818	1590
2nd	731	585

A set of possible top and seat angle with double web angle connections that can be used for the PR frame is given in Table 13. Using the values shown in this table, the connection parameters for the three-parameter model are calculated using Eqs. (3), (9), (17a) and are summarized in Table 14. The M-θ curves of these connections are plotted in Figures 11 and 12 together with the beam lines computed from Eq. (18) for the two load cases. From these figures, the secant stiffness for load case 1 R_{kb1} can be determined and are presented in Table 15. Connections C (3/4) and C (1/2) are selected because their $\overline{R}_k$ values are closest to their respective assumed values. Using the methodology depicted schematically in Figure 7, the linearized connection stiffness are determined for the two load cases and shown in Table 16.

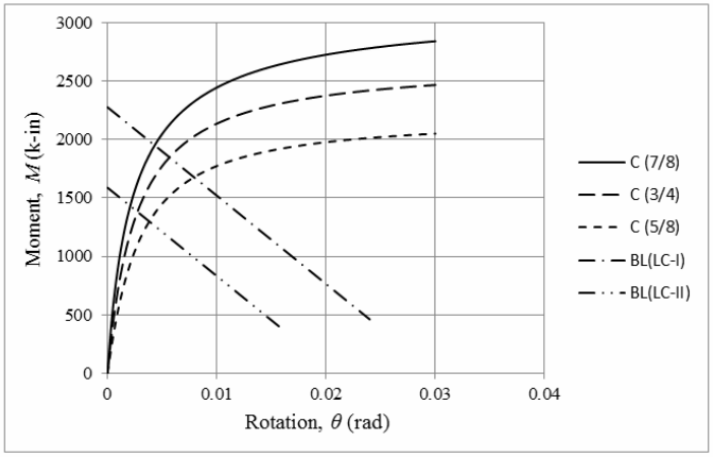

Figure 11. First Story M-θ Curves and Beam Lines (1 k-in. = 0.113 kN-m)

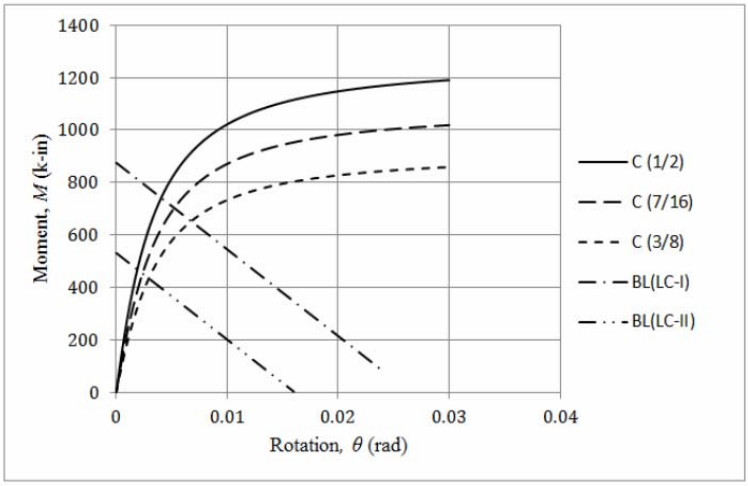

Figure 12. Second Story M-θ Curves and Beam Lines (1 k-in. = 0.113 kN-m)

Table 13. PR Connection Details (1 in. = 25.4 mm)

1st Story									
Connection	**Bolt Diameter** d (in.)	**Nut Width** W (in.)	**Top and Seat Angles** 2L6 × 4 × t_t				**Web Angles** 2L4 × 4 × 5/8		
			t_t (in.)	l_t (in.)	g_{ct} (in.)	k_t (in.)	l_w (in.)	g_{cw} (in.)	k_w (in.)
C (5/8)	7/8	1-7/16	5/8	7	2.75	1-1/8	8	2.5	1
C (3/4)	7/8	1-7/16	3/4	7	2.75	1-1/4	8	2.5	1
C (7/8)	7/8	1-7/16	7/8	7	2.75	1-3/8	8	2.5	1
2nd Story									
Connection	**Bolt Diameter** d (in.)	**Nut Width** W (in.)	**Top and Seat Angles** 2L6 × 4 × t_t				**Web Angles** 2L4 × 3.5 × ½		
			t_t (in.)	l_t (in.)	g_{ct} (in.)	k_t (in.)	l_w (in.)	g_{cw} (in.)	k_w (in.)
C (3/8)	7/8	1-7/16	3/8	7	2.5	7/8	8	2.25	7/8
C (7/16)	7/8	1-7/16	7/16	7	2.5	15/16	8	2.25	7/8
C (1/2)	7/8	1-7/16	1/2	7	2.5	1	8	2.25	7/8

Table 14. Connection Parameters (1 k-in. = 0.113 kN-m)

Connection	R_{ki} **(×10³)** (kips-in./rad)	M_{ult} (kips-in.)	n
1st Story			
C (5/8)	686	2187	1.41
C (3/4)	1010	2663	1.03
C (7/8)	1497	3140	0.89
2nd Story			
C (3/8)	212	908	1.32
C (7/16)	258	1077	1.31
C (1/2)	322	1261	1.27

Table 15. Connection Stiffness (1 k-in. = 0.113 kN-m)

Connection	**Connection Stiffness,** R_{kb1} **(×10³)** (k-in./rad)	$\bar{R}_k = R_{kb1}L/EI$
1st story		
C (5/8)	209	5.52
C (3/4)	325	8.6
C (7/8)	453	12
2nd story		
C (3/8)	92	5.6
C (7/16)	142	8.6
C (1/2)	183	11

Table 16. Linearized Connection Stiffness(1 k-in./rad = 0.113 kN-m/rad)

Beam Line for Load Case (BL-LC)	**Linearized Connection Stiffness**			
	R_{kb} **(×10³)** (k-in./rad)		R_{kL} **(×10³)** (k-in./rad)	
	1st Story	2nd story	1st Story	2nd story
1	325	183	-	-
2	572	246	66	38

Based on P_u and M_{neg} calculated for the gravity load case, a W10×33 ($\phi_c P_n$=292 kips or 1300 kN, $\phi_b M_n$=1530 k-in. or 173 kN-m) is selected as a trial section for the columns. Because each end of the 1st story beam is connected to two columns, a distribution factor based on the flexural stiffness of the columns above and below the beam as given by Eqs. (22a and 22b) can be used to apportion M_{neg} to the columns.

$$M_{above} = \frac{\left(\frac{I}{L}\right)_{above}}{\left(\frac{I}{L}\right)_{above} + \left(\frac{I}{L}\right)_{below}} M_{neg} \tag{22a}$$

$$M_{below} = \frac{\left(\frac{I}{L}\right)_{below}}{\left(\frac{I}{L}\right)_{above} + \left(\frac{I}{L}\right)_{below}} M_{neg} \quad (22b)$$

Using the analysis parameters computed and given in Tables 17 and 18, a direct analysis as outlined in Section 4 is carried out for the two load cases. The results together with the 2nd-order inelastic analysis and unity check results are given in Table 19. As can be seen, good correlation is observed between the direct analysis results and those obtained using 2nd-order inelastic analysis. The unity check is also satisfied for all members.

Table 17. Case 1 Analysis Parameters (1 k = 4.45 kN, 1 in. = 25.4 mm)

Story	**Element Stiffness**			**Applied Loads**	
	Columns EI_e=0.8 τEI (k-in.^{2})	**Beam** EI_e=0.8EI (k-in.^{2})	**Connections** 0.9R_{kb1} (k-in./rad)	**Gravity Load** 1.2D+1.6L (k/in.)	**Notional Load** 0.002P_i (kips)
1st	3.97×10^6	9.07×10^6	292×10^3	0.303	0.091
2nd	3.97×10^6	3.97×10^6	165×10^3	0.117	0.035

Table 18. Case 2 Analysis Parameters(1 k = 4.45 kN, 1 in. = 25.4 mm)

Story	**Element Stiffness**		**Applied Loads**		
	Gravity load step				
	Columns EI_e=0.8 τEI (k-in.^{2})	**Beam** EI_e=0.8EI (k-in.^{2})	**Connections** 0.9R_{kb2} (k-in./rad)	**Load** 1.2D+0.5L (k/in.)	**N.L** 0.002P_i (kips)
1st	3.97×10^6	9.07×10^6	515×10^3	0.212	-
2nd	3.97×10^6	3.97×10^6	222×10^3	0.071	-
	Lateral load step				
	Columns EI_e=0.8 τEI (k-in.^{2})	**Beam** EI_e=0.8EI (k-in.^{2})	**Connections**	**Load**	**Notional Load** 0.002 P_i (kips)
			0.9R_{ki} (k-in./rad)	0.9R_{kL} (k-in./rad)	Column Load (kips)	Wind 1.0W (kips)	
1st	3.97×10^6	9.07×10^6	909×10^3	59×10^3	31.8	7.8	0.064
2nd	3.97×10^6	3.97×10^6	290×10^3	34×10^3	10.6	3.9	0.021

The service live load deflections of the 1st and 2nd story beams are computed to be 0.37 in. (9.4 mm) and 0.44 in. (11.1 mm), respectively, and the wind induced interstory drifts of the frame are calculated to be 0.62 in (15.7 mm) for the 1st story and 0.68 in. (17.2 mm) for the 2nd story. They are within the allowable values of L/360=0.833 in. (21.2 mm) for beam deflection and H/200=0.72 in. (18.2 mm) for interstory drift, and so the design is considered satisfactory.

Table 19. Analysis results for Cases 1 and 2 with Unity Check
(1 kip = 4.45 kN, 1 k-in. = 0.113 kN/m)

Load Case	Element	Axial Force (kips)		Moment (k-in.)		Unity Check	
		Proposed method	2nd-order Inelastic Analysis	Proposed method	2nd-order Inelastic Analysis	Proposed method	2nd-order Inelastic Analysis
1	Col 1	63	63	685	662	0.61	0.60
	Col 2	63	63	699	676	0.62	0.61
	Col 3	17.5	17.5	866	836	0.60	0.58
	Col 4	17.6	17.6	870	840	0.60	0.58
	1st story Beam	-	-	1843	1897	0.97	0.99
	2nd story Beam	-	-	637	656	0.69	0.72
2	Col 1	38	39	349	347	0.33	0.3
	Col 2	46	46	826	809	0.64	0.61
	Col 3	9.5	9.5	440	423	0.30	0.3
	Col 4	12	12	687	665	0.47	0.45
	1st story Beam	-	-	1350	1388	0.71	0.73
	2nd story Beam	-	-	412	423	0.45	0.46

7. SUMMARY AND CONCLUSIONS

A procedure for the design of partially-restrained (PR) frames is proposed. In a PR frame, the connections used to connect the beams and columns are semi-rigid in nature. According to AISC [22], a connection is considered semi-rigid if the ratio of its secant stiffness under service load R_{ks} to the beam stiffness EI/L falls in the range $2 < R_{ks}L/EI < 20$. The proposed procedure makes use of the three-parameter connection model to describe the nonlinear connection moment-rotation (M-θ) behavior and the direct analysis approach to perform the frame analysis. To proceed with the design, a connection stiffness R_{kb} defined as the slope of a line drawn from the origin to the intersection point of the nonlinear M-θ curve and the beam line constructed for the factored gravity load case under consideration is used. Loading and unloading behavior of the PR connections are accounted for by the use of two different stiffness R_{kL} and R_{ki}; the former is obtained from linearization of the M-θ curve and the latter is obtained from the three-parameter connection model.

Trial beam sections are selected based on the beam moments M_{pos} and M_{neg} calculated using a target value of $\overline{R}_k = R_{kb}L/EI$ for the connections under factored gravity loads. The connections are then selected based on the proximity of their $\overline{R}_k$ values to those of the target values. Once the connections are selected, trial column (beam-column to be exact) sections can be selected based on the approximate P_u and M_u values computed from the applied gravity loads and M_{neg} of the adjoining connections, respectively.

Examples of PR frames designed using top and seat with web angle connections were given to demonstrate the steps involved in applying the proposed method in PR frame design. It was shown that despite its simplicity, the proposed approach yields good results when compared to a 2nd-order inelastic analysis.

REFERENCES

[1] Ang, K.M. and Morris, G.A., "Analysis of Three-Dimensional Frames with Flexible Beam-Column Connections", Canadian Journal of Civil Engineers, 1984, Vol. 11, pp. 245-254.

[2] Lui, E.M. and Chen, W.F., "Analysis and Behavior of Flexibly Jointed Frames," Engineering Structures, 1986, Vol. 8, No. 2, pp. 107-118.

[3] Lui, E.M. and Chen, W.F., "Steel Frame Analysis with Flexible Joints", Journal of Construction Steel Research, 1987, Vol. 8, pp. 161-202.

[4] Lui, E.M. and Chen, W.F., "Behavior of Braced and Unbraced Semi-Rigid Frames", International Journal of Solids and Structures, 1988, Vol. 24, No. 9, pp. 893-913.

[5] Chen, W.F., "Joint Flexibility in Steel Frames," Journal of Constructional Steel Research, 8, Special Issue, 1987.

[6] Cunningham, R., "Some Aspects of Semi-Rigid Connections in Structural Steelwork", the Structural Engineer, 1990, Vol. 68, No. 5, pp. 85-92.

[7] Wu, F. S., and W. F. Chen (1990), "A Design Model for Semi-Rigid Connections," Engineering Structures, 1990, Vol. 12, No. 2, pp. 88-97.

[8] Barakat, M., and Chen W. F., "Practical Analysis of Semi-Rigid Frames," Engineering Journal, AISC, 1990, Vol. 27, No. 2, pp. 54-68.

[9] Barakat, M., and Chen W. F., "Design Analysis of Semi Rigid Frames: Evaluation and Implementation," Engineering Journal, AISC, 1991, Vol. 28, No. 2, pp. 55-64.

[10] Hsieh, S. H., and Deierlein, G. C., "Nonlinear Analysis of Three-Dimensional Steel Frames with Semi-Rigid Connections," Computer and Structures, 1991, Vol. 41, No. 5, pp. 995-1009.

[11] Lui, E.M., "Stability Design of Partially Restrained Frames", Fifth International Colloquium on Stability of Metal Structures, Chicago, IL, 1996, pp. 259-268.

[12] Xu, L., "Semirigid Frame Structures", Chapter 23, in Handbook of Structural Engineering, 2nd edition, W.F. Chen and E.M. Lui (editors), CRC Press, Boca Raton, FL., 2005.

[13] Surovek, A.E., White D.W., and Leon, R.T., "Direct Analysis for Design Evaluation of Partially-Restrained Steel Framing Systems," Journal of Structural Engineering, ASCE, 2005, Vol. 131, No. 9, pp. 1376-1389.

[14] Narayanan, R., Structural Connections: Stability and Strength, EF Spon/Routledge, New York, N.Y., 1990.

[15] Lorenz, R.F., Kato, B., and Chen W.F., "Semi-rigid Connections in Steel Frames", Council on Tall Buildings and Urban Habitat, Committee 43, McGraw-Hill, New York, NY., 1993.

[16] Chen, W.F., Goto, Y., and Liew, J.Y.R., Stability Design of Semi-Rigid Frames, John Wiley and Sons, New York, N.Y., 1996.

[17] Bjorhovde, R., Colson, A., and Zandonini, R., Connections in Steel Structures III, Pergamon Press, Oxford, U.K., 1996.

[18] Chan, S.L. and Chui, P.P.T., Non-linear Static and Cyclic Analysis of Steel Frames with Semi-Rigid Connections, Elsevier Science, Oxford, UK., 2000.

[19] Chen, W.F., Practical Analysis for Semi-Rigid Frame Design, World Scientific, Singapore, 2000.

[20] Faella, C., Piluso, V., and Rizzano, G., Structural Steel Semirigid Connections, CRC Press, Boca Raton, FL., 2000.

[21] Chen, W.F., Kishi, N., Komuro, M., Semi-rigid Connections Handbook, J. Ross Publishing, Fort Lauderdale, FL., 2011.

[22] AISC Specification for Structural Steel Buildings, American Institute of Steel Construction, Inc., Chicago, IL., 2010.

[23] Cerfontaine, F. and Jaspart, J.P., "Analytical Study of the Interaction between Bending and Axial Force in Bolted Jointed", In: Eurosteel, Coimbra, 2002, pp. 997-1006.

[24] Urbonas, K. and Daniunas, A., "Component Method Extension to Steel Beam-to-Beam and Beam-to-Column Knee Joints Under Bending and Axial Forces", Journal of Civil Engineering and Management, XI (3), 2005, pp. 217-224.

[25] Urbonas, K. and Daniunas, A., "Behaviour of Semi-Rigid Steel Beam-to-Beam Joints Under Bending and Axial Forces", Journal of Constructional Steel Research, 2006, Vol. 62, pp. 1244-1249,

[26] Frye, M.J. and Morris, G.A., "Analysis of Flexibly Connected Steel Frames", Canadian Journal of Civil Engineers, 1975, Vol. 2, No. 3, pp. 280-291.

[27] Goverdhan, A.V., A Collection of Experimental Moment-Rotation Curves and the Evaluation of Predicting Equations for Semi-Rigid Connections, M.S. Thesis, Vanderbilt University, Nashville, TN., 1983.

[28] Nethercot, D.A., "Steel Beam-to-Column Connections - A Review of Test Data and its Applicability to the Evaluation of Joint Behavior in the Performance of steel Frames", CIRIA Project Study, 1985.

[29] Kishi, N. and Chen, W.F., "Data Base of Steel Beam-to-Column Connections", Structural Engineering Report, CE-STR-86-26, School of Civil Engineering, Purdue University, West Lafayette, IN., 1986.

[30] Chen, W.F. and Kishi, N., "Semi-Rigid Steel Beam-to-Column Connections: Data Base and Modeling," Journal of Structural Engineering, ASCE, 1989, Vol. 115, No. 1, pp. 105-119.

[31] Bjorhovde, R., Colson, A., and Brozzetti, J., "Classification System for Beam-to-Column." Journal of Structural Engineering, ASCE, 1990, Vol. 116, No. 11, pp. 3059-3076.

[32] Eurocode 3, "Design of Steel Structures – Part 1-1: General Rules and Rules for Buildings", EN 1993, European Committee for Standardisation (CEN), 1993.

[33] Nethercot, D.A., Ahmed, T.Q., and Li, B., "Unified Classification System for Beam-to-column Connections", J. of Constructional Steel Research, 1998, Vol. 45, No. 1, pp. 39-65.

[34] Chen, W.F. and Lui, E.M., Stability Design of Steel Frames, CRC Press, Boca Raton, FL., 1991.

[35] PRCONN, Moment-Rotation Curves for Partially Restrained Connections, RMR Design Group, Inc., Tucson, AZ., 1993.

[36] Chen, W.F. and Toma, S., Advanced Analysis of Steel Frames - Theory, Software and Applications, CRC Press, Boca Raton, FL., 1994.

[37] Kishi, N., Chen, W.F., Matsuoka, K.G., and Nomachi, S.G., "Moment-Rotation Relation of Top-and Seat-Angle with Double Web-Angle Connections," Proceedings of the State-of-the-Art Workshop on Connections and the Behavior, Strength and Design of Steel Structures, R. Bjorhovde, J. Brozzetti, and A. Colson, eds., Ecole Normale Superieure de Cachan, France, May 25-27, 1987, London: Elsevier, pp. 121-134.

[38] Kishi, N., Chen, W.F., Matsuoka, K.G., and Nomachi, S.G., "Moment-Rotation Relation of Single/ Double Web-Angle Connections," Proceedings of the State-of-the-Art Workshop on Connections and the Behavior, Strength and Design of Steel Structures, R. Bjorhovde, J. Brozzetti, and A. Colson, eds., Ecole Normale Superieure de Cachan, France, May 25-27, 1987, London: Elsevier, pp. 135-149.

[39] Kishi, N. and Chen, W.F., "Moment-Rotation Relations of Semi-Rigid Connections with Angles, Journal of Structural Engineering", ASCE, 1990, Vol. 116, No. 7, pp. 1813-1834.

[40] Richard, R. M., and B. J. Abbott (1975), "Versatile Elastic-Plastic Stress-Strain Formula," Journal of Engineering Mechanics Division, ASCE,1975, Vol. 101, No. 4, pp. 511-515.

[41] Kishi, N., Chen, W.F., Goto, Y., and Matsuoka, K.G., "Design Aid of Semi-Rigid Connections for Frame Analysis", Engineering Journal, AISC, 1993, Vol. 30, No. 3, pp. 90-107.

[42] Christopher, J. E., and Bjorhovde, R., "Semi-Rigid Frame design for Practicing Engineers" Engineering Journal, AISC, 1999, Vol. 36, No. 1, pp. 12-28.

[43] McGuire, W., Gallagher, R. H., and Ziemian, R. D., Matrix Structural Analysis, 2nd Edition, Wiley, New York, 2000.
[44] ASCE Minimum Design Loads for Buildings and Other Structures, ASCE/SEI 7-10, American Society of Civil Engineers, Reston, VA., 2010.

AXIAL STRENGTH OF CFST COLUMNS CONSIDERING CONCRETE AGE

Hai-Yang Wang and Xiao-Xiong Zha*

Shenzhen Graduate School, Harbin Institute of Technology, Shenzhen 518055, PR China
**(Corresponding author: E-mail: zhahero@126.com and wangsea0510@126.com)*

Received: 8 September 2012; Revised: 21 November 2012; Accepted: 13 March 2013

ABSTRACT: Concrete filled steel tube (CFST) columns are used increasingly in high-rise buildings in China. During the rapid construction of high-rise buildings, concrete age is an important factor which will affect the composite axial strength. In this paper, based on the theory of elasticity, a formula is proposed to predict the composite axial strength of CFST considering the concrete age. For the most common use the parameters in the formula are simplified and calibrated by existing test results. Finally the experiments of the ultimate bearing capacity of CFST columns considering concrete age changes are carried out and the FE method is also adopted to validate the formula results. The results show that the formula can be used satisfactorily in predicting the strength of CFST columns considering concrete age.

Keywords: CFST, composite strength, concrete age, axial strength

1. INTRODUCTION

The concrete filled steel tube (CFST) structure is widely used now around the world because of its superior property on mechanics, fire resistance, anti seismic capacity as well as its cost effective construction. Extensive experimental and theoretical investigations on the CFST have been carried out [1-8]. In recent years, more and more high-rise buildings are constructed using CFST columns mentioned by Fu [9], Fan [10] and Duan [11]. The advantage is to adopt rapid construction which the inside concrete is not fully hardened during the construction and the building is be set up by the outside steel tube frame. This kind of construction method can greatly reduce the time but also bring a problem that the composite strength of CFST column may be different being of the earlier age of concrete.

On the influence of concrete age, Tan and Qi [12] worked systematically by testing the effect of creep on columns under axially compressive loads. Nakai et al. [13] and Terry et al. [14] tested the creep of CFST columns and plain concrete to investigate the influence of the reinforcement on the concrete creep. Ichinose et al. [15], Kwon et al. [16] and Acar [17] also reported a series of tests to obtain creep coefficients of CFST columns. But nearly all of the works are about the aging effect of hardened concrete and there is little attention paid to the research on the aging effect of hardening CFST column.

In this paper, the aging effect of un-fully hardened concrete will be studied on the composite strength of CFST columns and a formula will be proposed based on the theory of elasticity by using the superimposition method and test results. Independent experiments and FE method are also adopted to validate the formula.

2. THEORY ANALYSIS

2.1 Superimposition method

In order to determine the formula of composite strength of CFST columns under axial compression, the elastic analysis is adopted. The CFST column can be equivalently divided into two parts. i.e., the steel tube and the concrete part, and the axial compression process can be divided into two steps. i.e., uniaxial compression of each part and plane strain problem according to Yu [18]. In the uniaxial compression step, two parts are deformed individually as the uniform longitudinal strain. In the second step, there will be the interaction load between the two parts but the longitudinal strain of each part keeps constant which is the plane strain problem, shown in Figure 1.

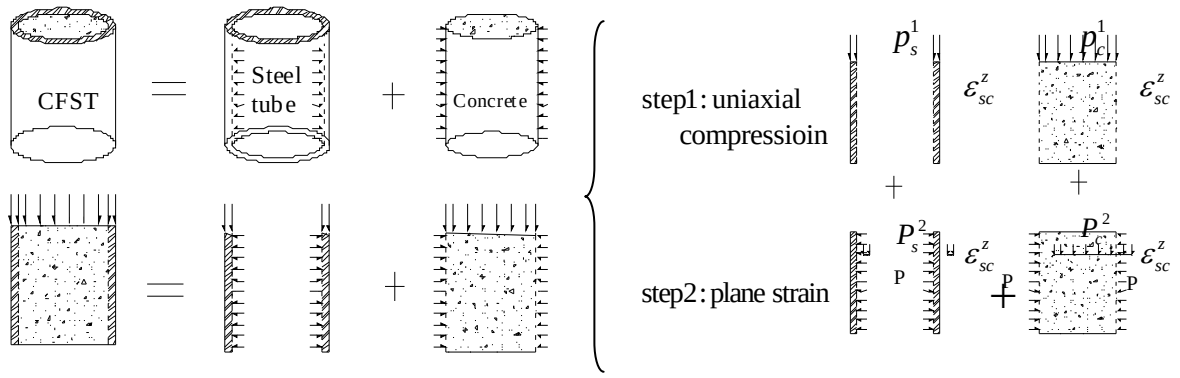

Figure 1. Superimposition Method of CFST under Axial Compression

2.2 Elastic Analysis

Assume that the longitudinal strain of the CFST is $\varepsilon_{sc}^{z}(t)$ under the compression load, as a whole. The longitudinal strains in the steel tube $\varepsilon_{s}^{z}(t)$ and the concrete $\varepsilon_{c}^{z}(t)$ should be the same, then

$$\varepsilon_{s}^{z}(t)=\varepsilon_{c}^{z}(t)=\varepsilon_{sc}^{z}(t) \tag{1}$$

Step 1: The uniaxial compression stage

In this stage, because of the no interactions between steel and concrete, steel tube and concrete cylinder are unrestrained axisymmetric deformation. According to the generalized Hooke's law the radial strains are:

$$\varepsilon_{c}^{r}(t)=-\nu_{c}(t)\varepsilon_{sc}^{z}(t) \tag{2}$$

$$\varepsilon_{s}^{r}(t)=-\nu_{s}\varepsilon_{sc}^{z}(t) \tag{3}$$

In which, $\nu_{c}(t)$ is the Poisson's ratio of concrete at age t, and ν_{s} is the Poisson's ratio of steel. According to Budynas [19], when the radius at the interface surface is r, the radial displacements $u_{c}^{1}(t)$ at the outside surface of the concrete cylinder and u_{s}^{1} at the inside surface of the steel tube, are respectively,

$$u_c^1(t) = r\varepsilon_c^r(t) = -\nu_c(t) r\varepsilon_{sc}^z(t) \tag{4}$$

$$u_s^1(t) = r\varepsilon_s^r(t) = -\nu_s r\varepsilon_{sc}^z(t) \tag{5}$$

So the respective longitudinal stresses of the concrete $\sigma_c^1(t)$ and the steel $\sigma_s^1(t)$ are,

$$\sigma_c^1(t) = E_c(t)\varepsilon_c^z(t) = E_c(t)\varepsilon_{sc}^z(t) \tag{6}$$

$$\sigma_s^1(t) = E_s\varepsilon_s^z(t) = E_s\varepsilon_{sc}^z(t) \tag{7}$$

In which, $E_c(t)$ is the elastic modulus of concrete at age t, and E_s is the elastic modulus of steel.

Step 2: The plane strain stage

In this stage the longitudinal strain is constant and there is the interactive stress P acting between the inside surface of the steel tube and the outside surface of the concrete. According to the theory of elasticity [20], the radial displacements of the concrete cylinder at the outside surface $u_c^2(t)$, and the radial displacements of the steel tube at the inside surface u_s^2 can be calculated respectively,

$$u_c^2(t) = -\frac{r^2 P}{\frac{E_c(t)}{1-\nu_c^2(t)} r^2}\left(1-\frac{\nu_c(t)}{1-\nu_c(t)}\right)r = -\frac{(1+\nu_c(t))(1-2\nu_c(t))}{E_c(t)} rP \tag{8}$$

$$u_s^2 = \frac{(1+\nu_s) r^2 P}{E_s(R^2-r^2)}\left[\frac{R^2}{r} + (1-2\nu_s) r\right] \tag{9}$$

In which, R is the radius at the outside surface of the steel tube.

Step 3: Superimposition results

Assume that the interfaces are ideal and continuous at the interfaces of the steel tube and concrete part. So the radial displacements of steel part and the concrete part should be same at the interfaces,

$$u_c^1(t) + u_c^2(t) = u_s^1 + u_s^2 \tag{10}$$

Introducing Eqs. 4, 5, 8 and 9 into Eq. 10 yields the interactive stress P at the interface,

$$P = \frac{-(\nu_c(t)-\nu_s)\varepsilon_{sc}^z(t)}{\frac{(1+\nu_c(t))(1-2\nu_c(t))}{E_c(t)} + \frac{(1+\nu_s)}{E_s(R^2-r^2)}\left[R^2 + r^2(1-2\nu_s)\right]} \tag{11}$$

From the elastic solution from Sadd [20], the longitudinal stresses caused by P in the concrete part $\sigma_c^2(t)$, and the steel tube $\sigma_s^2(t)$, are,

$$\sigma_c^2(t) = -2\nu_c(t) P \tag{12}$$

$$\sigma_s^2(t) = \frac{2\nu_s r^2}{R^2-r^2} P \tag{13}$$

Hence, the total longitudinal stresses in the concrete and the steel tube are, respectively,

$$\sigma_c(t) = \sigma_c^1(t) + \sigma_c^2(t) = E_c(t)\varepsilon_{sc}^z(t) - 2\nu_c(t)P \tag{14}$$

$$\sigma_s(t) = \sigma_s^1 + \sigma_s^2 = E_s\varepsilon_{sc}^z(t) + \frac{2\nu_s r^2}{R^2 - r^2}P \tag{15}$$

Introducing Eq. 11 into Eq. 14 and Eq. 15, the equivalent uniform stress distribution $\sigma_{sc}(t)$ over the cross section of the CFST is ,

$$\sigma_{sc}(t) = \frac{A_s\sigma_s(t) + A_c\sigma_c(t)}{A_{sc}} \tag{16}$$

Thus,

$$\sigma_{sc}(t) = \left[1 + \frac{2(\nu_c - \nu_s)^2\alpha\,\sigma_s^1/\sigma_c^1(t)}{\left[(1-2\nu_c)(1+\nu_c)\alpha\,\sigma_s^1/\sigma_c^1(t) + 2(1-\nu_s^2) + (1+\nu_s)\alpha\right]\left(1+\alpha\,\sigma_s^1/\sigma_c^1(t)\right)}\right]\left[(1-\beta)\sigma_c^1(t) + \beta\sigma_s^1\right] \tag{17}$$

Replacing all terms containing Poisson's ratios of steel and concrete by A, B and C, Eq. 17 can be written as below,

$$\sigma_{sc}(t) = \left[1 + \frac{\alpha\sigma_s^1/\sigma_c^1(t)}{\left[A + B\alpha\sigma_s^1/\sigma_c^1(t) + C\alpha\right]\left(1+\alpha\sigma_s^1/\sigma_c^1(t)\right)}\right]\left[(1-\beta)\sigma_c^1(t) + \beta\sigma_s^1\right] \tag{18}$$

where, $A = \frac{(1-\nu_s^2)}{(\nu_c - \nu_s)^2}$, $B = \frac{(1-2\nu_c)(1+\nu_c)}{2(\nu_c - \nu_s)^2}$, $C = \frac{(1+\nu_s)}{2(\nu_c - \nu_s)^2}$, $\beta = \alpha/(1+\alpha)$.

2.3 Composite Strength of the CFST and Further Modification

In order to obtain the composite strength of CFST column in inelastic state, it is assumed that the strength of the steel and the concrete are reached simultaneously and introducing the strength of steel and concrete f_y , $f_{ck}(t)$ and parameter $\xi_{sc}(t) = \alpha f_y / f_{ck}(t)$. So,

$$f_{sc}(t) = \left[1 + \frac{\xi_{sc}(t)}{\left[A + B\xi_{sc}(t) + C\alpha\right]\left(1+\xi_{sc}(t)\right)}\right]\left[(1-\beta) f_{ck}(t) + \beta f_y\right] \tag{19}$$

The influence of concrete age on concrete Poisson's ratio is very little according to Oluokun et al. [21] and Carmichael [22], so the concrete Poisson's ratio can be determined by test results of hardened CFST column which is at the age of 28 days. To statistically obtain estimated values of A, B, and C, standard regression analysis is carried out on the basis of a rich collection of test results from O'Shea et al. [3] and Kenji et al. [23]. Finally the values of the three constants are $A = 2.0$, $B = 0.01$, $C = 0.2$ as showing Table 1 and the results agree well.

Table 1. Comparison of the Analytical and the Test Results

Ref.	No.	Numbering	Geometric parameters		material parameters		Ultimate force		ratio
			External diameter D /mm	Steel thickness T /mm	f_y /Mpa	f_{ck} /Mpa	Test N_T /kN	Calc N_c /kN	N_T/N_c
[3]	1	S30CS50B	165	2.8	363.3	48.3	1662	1744	1.05
	2	S20CS50A	190	1.9	256.4	41	1678	1556	0.93
	3	S16CS50B	190	1.5	306.1	48.3	1695	1739	1.03
	4	S12CS50A	190	1.1	185.7	41	1377	1322	0.96
	5	S10CS50A	190	0.9	210.7	41	1350	1303	0.97
	6	S30CS80A	165	2.8	363.3	80.2	2295	2381	1.04
	7	S20CS80B	190	1.9	256.4	74.7	2592	2473	0.95
	8	S16CS80A	190	1.5	306.1	80.2	2602	2615	1.00
	9	S12CS80A	190	1.1	185.7	80.2	2295	2407	1.05
	10	S10CS80B	190	0.9	210.7	74.7	2451	2241	0.91
[3]	11	S30CS10A	165	2.8	363.3	108	2673	2935	1.10
	12	S20CS10A	190	1.9	256.4	108	3360	3379	1.01
	13	S16CS10A	190	1.5	306.1	108	3260	3378	1.04
	14	S12CS10A	190	1.1	185.7	108	3058	3176	1.04
	15	S10CS10A	190	0.9	210.7	108	3070	3168	1.03
[23]	16	CC4-A-2	149	3	308	21.5	941	971	1.03
	17	CC4-A-4-1	149	3	308	33.1	1064	1159	1.09
	18	CC4-A-4-2	149	3	308	33.1	1080	1159	1.07
	19	CC4-A-8	149	3	308	61.2	1781	1610	0.90
	20	CC4-C-2	301	3	279	21.5	2382	2629	1.10
	21	CC4-C-4-1	300	3	279	33.6	3277	3438	1.05
	22	CC4-C-4-2	300	3	279	33.6	3152	3438	1.09
	23	CC4-C-8	301	3	279	63.8	5540	5522	1.00
	24	CC4-D-2	450	3	279	21.5	4415	5069	1.15
	25	CC4-D-4-1	450	3	279	33.6	6870	6944	1.01
	26	CC4-D-4-2	450	3	279	33.6	6985	6944	0.99
	27	CC4-D-8	450	3	279	67.6	11665	12213	1.05
	28	CC6-A-2	122	4.5	576	21.5	1509	1655	1.10
	29	CC6-A-4-1	122	4.5	576	33.1	1657	1771	1.07
	30	CC6-A-4-2	122	4.5	576	33.1	1663	1771	1.06
	31	CC6-A-8	122	4.5	576	61.2	2100	2052	0.98
	32	CC6-C-2	239	4.5	507	21.5	3035	3429	1.13
	33	CC6-C-4-1	238	4.5	507	33.1	3583	3890	1.09
	34	CC6-C-4-2	238	4.5	507	33.1	3647	3890	1.07
	35	CC6-C-8	238	4.5	507	61.2	5578	5044	0.90
	36	CC6-D-2	361	4.5	525	21.5	5633	6088	1.08

	37	CC6-D-4-1	361	4.5	525	33.6	7260	7266	1.00
	38	CC6-D-4-2	360	4.5	525	33.6	7045	7237	1.03
	39	CC6-D-8	360	4.5	525	67.6	11505	10526	0.91
	40	CC8-A-2	108	6.5	853	21.5	2275	2768	1.22
	41	CC8-A-4-1	109	6.5	853	33.1	2446	2882	1.18
	42	CC8-A-4-2	108	6.5	853	33.1	2402	2851	1.19
	43	CC8-A-8	108	6.5	853	61.2	2713	3050	1.12
	44	CC8-C-2	222	6.5	843	21.5	4964	6254	1.26
	45	CC8-C-4-1	222	6.5	843	33.1	5638	6654	1.18
	46	CC8-C-4-2	222	6.5	843	33.1	5714	6654	1.16
	47	CC8-C-8	222	6.5	843	61.2	7304	7617	1.04
	48	CC8-D-2	337	6.5	823	21.5	8475	10045	1.19
	49	CC8-D-4-1	337	6.5	823	33.6	9668	11044	1.14
	50	CC8-D-4-2	337	6.5	823	33.6	9835	11044	1.12
	51	CC8-D-8	337	6.5	823	67.6	13776	13849	1.01

Thus, the composite strength of CFST column considering the age is simplified as shown in Eq.(20), in which $M = 0.001\xi_{sc}(t) + 0.2\alpha$.

$$f_{sc}(t) = \left[1 + \frac{\xi_{sc}(t)}{[2+M]\left(1+\xi_{sc}(t)\right)}\right]\left[(1-\beta) f_{ck}(t) + \beta f_y\right] \tag{20}$$

In practice, the range of steel grade is Q235 to Q420, and concrete is C30 to C80, the range of $f_y / f_{ck}(t)$ is 4.7 to 20.9. The range of steel ratio of CFST is from 0.04 to 0.2, Thus, the range of M is from 0.008 to 0.04 and $1/(2+M) \approx 0.5$. Also according to ACI209 [24], there is a relationship between the strength of hardened and hardening concrete,

$$f_{ck}(t) = Q(t) f_{ck} \tag{21}$$

$$Q(t) = \frac{t}{4 + 0.85t} \tag{22}$$

Then, the composite strength of CFST column considering concrete age can be expressed as following,

$$f_{sc}(t) = \left[1 + \frac{0.5\xi_{sc}(t)}{\left(1+\xi_{sc}(t)\right)}\right]\left[(1-\beta) f_{ck}(t) + \beta f_y\right] = \frac{Q(t) + 1.5\xi_{sc}^0}{1+\alpha} f_{ck}$$
$$= \frac{\frac{t}{4+0.85t} + 1.5\xi_{sc}^0}{1+\alpha} f_{ck} \tag{23}$$

In which, $\xi_{sc}^0 = \alpha f_y / f_{ck}$, and f_{ck} is the strength of hardened concrete.

3. Experiments and FE Analysis

In order to validate the formula of composite strength of CFST column considering concrete age of different hardening time, experiments and FEM are used in this section.

3.1 FE Model of CFST Columns

The software Abaqus is adopted to establish the FE Model. In the model, the 8-node quadrilateral in-plane general purpose continuum shell element (SC8R) is used for the steel tube, and the 8-node linear brick element (C3D8R) is used for the concrete. The bilinear material model is adopted for the steel, with the tangent modulus being one percent of the Elastic Modulus of 206GPa. The material model of the concrete is the damaged plasticity (DP) model with dilation angle being 40^o, and the strength of the concrete at different hardening time follows the curves proposed by Yi [25], as Eq. (24). Other material and geometrical parameters of the column are given in Table 2. According to the experimental specimen in Figure 2, the FE meshes of a typical CFST column are shown in Figure 3. It is assumed that the contact between the steel tube and the concrete is perfect. In order to study the convergent of the FEM model, different meshing schemes are tried which are listed in Table 3.

$$f_c(t) = \frac{\beta_m(\varepsilon_c / \varepsilon_c^{'})}{\beta_m - 1 + (\varepsilon_c / \varepsilon_c^{'})^{\beta_m}} f_c^{'} \tag{24}$$

$$\beta_m = \beta_{m,a} = \left[1.02 - 1.17(E_0 / E_c)\right]^{-0.74} \quad , \varepsilon_c < \varepsilon_c^{'} \tag{25}$$

$$\beta_m = \beta_{m,d} = \beta_{m,a} + (a + bt) \quad , \quad \varepsilon_c \geq \varepsilon_c^{'} \tag{26}$$

$$a = \left(12.4 - 1.66 \times 10^{-2} f_{c,28}\right)^{-0.46} \tag{27}$$

$$b = 0.83 \exp(-911 / f_{c,28}) \tag{28}$$

Where,

t —— the age of concrete in day;

$f_c(t), \varepsilon_c$ —— concrete stress and strain to be computed;

$f_c^{'}, \varepsilon_c^{'}$ —— maximum stress and corresponding strain of concrete at $t$days;

E_0 —— the secant modulus at the maximum stress, $E_0 = f_c^{'} / \varepsilon_c^{'}$;

E_c —— elastic modulus of concrete;

$\beta_{m,a}$ —— a parameter of concrete for the ascending branch;

$\beta_{m,d}$ —— a parameter of concrete for the descending branch.

Figure 2. Experimental Specimens of CFST

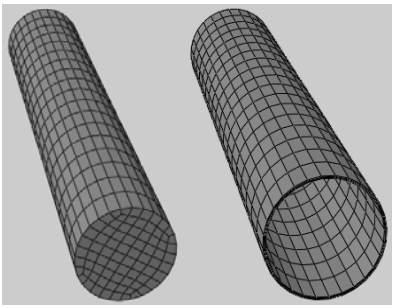

a) concrete b) Steel tube

Figure 3. Finite Element Mesh of CFST Member

Table 2. Geometry and Material Parameters of CFST Column

D (mm)	T (mm)	L (mm)	f_y (MPa)	f_{ck} (MPa)	E_s (MPa)
219	5.5	766	355	51.2	2.06e5
133	4.5	400	345	40.8	2.06e5

Table 3. The Ultimate Load of Different Meshing Scheme

Model	N-Ring	N-Radius	N-Axial	E-Section	E-Tolal	N-3d (kN)	N-28d (kN)
M1	12	2,3	18	56	1120	2240	2868
M2	12	3,4	18	68	1224	2256	2904
M3	16	3,4	18	96	1728	2285	2942
M4	20	3,4	18	104	1872	2358	2965
M5	24	3,4	18	132	2376	2372	2972
M6	28	3,4	18	160	2880	2377	2979

In Table 3, N-Ring, N-Radius, and N-Axial are the respective numbers of elements in the circumferential, radial, and axial directions. E-Section and E-Total are the total numbers of elements on a cross section and of the whole column, respectively. N-3d and N-28d are the ultimate axial loads of the column at the age of 3 and 28 days. It can be seen that when the element mesh is finer than M4, smaller difference between the different meshing schemes are observed. It is decided therefore that the mesh scheme M4 will be used in the following numerical simulations.

Figure 4. Load Bearing Capacity Experiment of the CFST Column

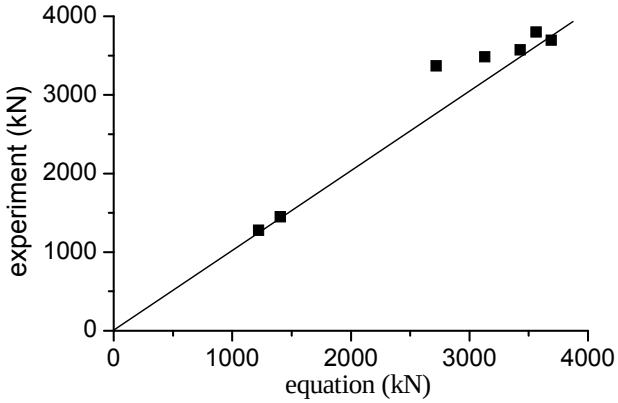

Fig.5 calculated value compared with experiment

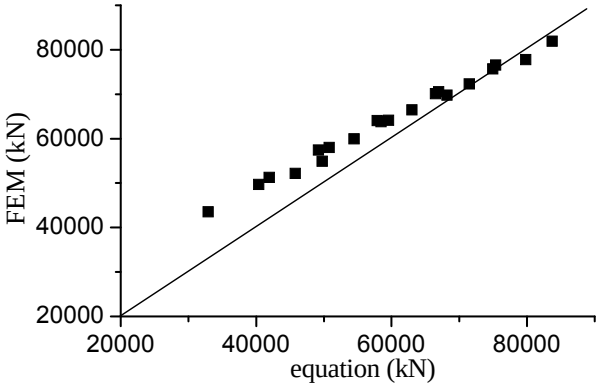

Figure 6. Calculated Value Compared with FEM

3.2 Validation of the Formula

Laboratory experiments had been carried out, as shown in Figures 2 and 4, and the specimen configuration details are specified in Table 2. The load bearing capacity experiments were taken at the concrete curing ages of 3, 7, 14, 21, 35 and 49 days.

The experimental results of the time-dependent elastic modulus of concrete at different ages are shown in Table 4. The comparison between equation results N_c, experimental results N_t and FE results N_f are showed in Table 5, 6 and Figure 5, 6. And the mean value is 0.945 and standard deviation is 0.06 which indicate the formula can predict well the composite strength of CFST columns by considering the variation of concrete curing age.

Table 4. Elastic Modulus of the Concrete at Different Age

age(day)	3	7	14	21	28
E_c (MPa)	30680	32319	34053	35101	35905

Table 5. Further Comparisons of Analytical Results with the Tests Results

No.	D /mm	T /mm	f_y /MPa	f_{ck} /MPa	t /day	f_{sc} /MPa	N_c /kN	N_t /kN	N_c/N_t
1	219	5.5	355	22.626	3	72.21	2719	3368.3	0.807
2	219	5.5	355	34.754	7	83.15	3131	3484	0.899
3	219	5.5	355	43.497	14	91.04	3428	3572.7	0.959
4	219	5.5	355	47.478	21	94.63	3563	3797.7	0.938
5	219	5.5	355	51.230	35	98.02	3690	3694.7	0.999
6	219	5.5	355	53.025	49	99.64	3751	3802.3	0.987
7	133	4.5	345	28.704	7	87.92	1221	1276	0.956
8	133	4.5	345	40.80	53	101.3	1406	1447	0.972

Table 6. Further Comparisons of Analytical Results with FEM Results

No.	D /mm	T /mm	f_y /MPa	f_{ck} /MPa	t /day	f_{sc} /MPa	N_c /kN	N_f /kN	N_c/N_f
1	1000	12	345	18.641	3	41.95	32930	43497	0.757
2	1000	12	345	28.633	7	51.47	40402	49731	0.812
3	1000	12	345	35.836	14	58.33	45789	52161	0.878
4	1000	12	345	40.993	28	63.42	49781	54934	0.906
5	1000	18	345	18.641	3	53.41	41923	51250	0.818
6	1000	18	345	28.633	7	62.69	49213	57432	0.857
7	1000	18	345	35.836	14	69.39	54467	59979	0.908
8	1000	18	345	40.993	28	74.42	58422	63839	0.915
9	1000	24	345	18.641	3	64.70	50789	58000	0.876
10	1000	24	345	28.633	7	73.76	57898	64098	0.903
11	1000	24	345	35.836	14	80.28	63023	66483	0.948
12	1000	24	345	40.993	28	85.29	66955	70591	0.948
13	1000	30	345	18.641	3	75.86	59553	64129	0.929
14	1000	30	345	28.633	7	84.69	66484	70131	0.948
15	1000	30	345	35.836	14	91.06	71480	72343	0.988
16	1000	30	345	40.993	28	96.03	75382	76533	0.985
17	1000	36	345	18.641	3	86.87	68195	69795	0.977
18	1000	36	345	28.633	7	95.48	74950	75706	0.990
19	1000	36	345	35.836	14	101.68	79819	77777	1.026
20	1000	36	345	40.993	28	106.63	83702	81960	1.021

4. CONCLUSION

In the paper, an analytical solution was presented for composite strength of CFST columns considering the influence of concrete age of different hardening time. Bearing capacity experiments of CFST columns with different concrete age were conducted, and FM method was used to calculate the strength of CFST columns with different concrete aging time, steel ratio and concrete strength. Comparisons of composite strength between the formula, the experiment and the FE method results were made, which showed that the formula can predict the composite strength of CFST column well.

For the further work, it is needed to develop the formula of the stability property of CFST column considering the concrete age based on the one presented in this paper.

REFERENCES

[1] Tomii, M., Yoshimura, K. and Morishita, Y., “Experimental Studies on Concrete Filled Steel Tubular Stub Column under Concentric Loading”, Proceedings of the International Colloquium on Stability of Structures under Static and Dynamic Loads, Washington, USA, 1977, pp. 718-741.

[2] Schneider, S.P., “Axially Loaded Concrete-filled Steel Tubes”, J. Struct. Eng., 1998, Vol. 124, No. 10, pp. 1125 -1138.

[3] O'Shea, M.D. and Bridge, R.Q., “Design of Circular Thin-walled Concrete Filled Steel Tubes”, J. Struct. Eng., 2000, Vol. 126, No. 11, pp. 1295-1303.

[4] Giakoumelis, G. and Lam, D., “Axial Capacity of Circular Concrete-filled Tube Columns”, J. Constr. Steel Res., 2004, Vol. 60, No. 7, pp. 1049-1068.

[5] Zhong, S.T., “The Concrete-Filled Steel Tubular Structures”, Tsinghua Univ. Press, 2005. (In Chinese)

[6] Cai, Sh. H., “Modern Concrete Filled Steel Tubular Structure”, China Communications Press, 2007. (In Chinese)

[7] Zha, X.X., “Hollow and Solid Concrete-filled Steel Tube Columns Structure”, Science Press, 2011. (In Chinese)

[8] Han, L.H., “Concrete Filled Steel Tube Structure: Theory and Practice”, Science Press, 2007. (In Chinese)

[9] Fu, X.Y., “The Simulated Calculation of Highrise Building Structure under Vertical Construction Loads”, J. Shenzh. Univ. (Science & Engineering), 2003, Vol. 20, No. 4, pp. 8-13. (In Chinese)

[10] Fan, F., Wang, H.J. and Zhi, X.D., “Analysis of Vertical Deformation During Construction of the Shanghai World Financial Center”, J. Build Struct., 2010, Vol. 31, No.7, pp. 118-124. (In Chinese)

[11] Duan, X. Sh., Zhou, X.Y. and Chang, Y. Ch., “Stress Monitoring and Numerical Analysis in Construction Process for Tianjin Tower”, J. Build Struct., 2011, Vol. 41, No. 6, pp. 114-117. (In Chinese)

[12] Tan, S.J. and Qi, J.L., “Experimental Investigation of the Effect on the Strength of Concrete Filled Steel Tubular Compressive Members under Long-term Load”, J. Harb. Eng. Univ., 1987, No. 2, pp. 10-24. (In Chinese)

[13] Nakai, H., Kurita, A. and Ichinose, L.H., “An Experimental Study on Creep of Concrete Filled Steel Pipes”, Proceeding of the 3rd International Conference on Composite Construction in Steel and Concrete, 1991, pp. 55-60.

[14] Terry, P.J., Bradford, M.A. and Gilbert, R.I., “Creep and Shrinkage in Concrete Filled Steel Tubes”, Proceeding of the 6th International Symposium in Tubular Structures, 1994, pp. 293-298.
[15] Ichinose, L.H., Watanabe, E. and Nakai, H., “An Experimental Study on Creep of Concrete Filled Steel Pipes”, J. Constr. Steel Res., 2001, Vol. 57, No. 4, pp. 453-466.
[16] Kwon, S.H., Kim, Y.Y. and Kim, J. K., “Long-term Behaviour under Axial Service Loads of Circular Columns Made from Concrete Filled Steel Tubes”, Magaz. Concr. Res., 2005, Vol. 57, No. 2, pp. 87-99.
[17] Acar, M.H., “Evaluation of Creep Coefficient on Concrete-filled Steel Tubular Columns”, J. Eng. Mat. Scienc., 2007, Vol. 14, No. 4, pp. 295-302.
[18] Yu, M., Zha, X.X. and Ye, J., “A Unified Formulation for Hollow and Solid Concrete-filled Steel Tube Columns under Axial Compression”, Engin. Struct., 2010, Vol. 32, No. 4, pp. 1046-1053.
[19] Budynas, R.G., “Advanced Strength and Applied Stress Analysis”, Engin. Mechan. Scienc., 1998.
[20] Sadd, M.H., “Elasticity: Theory, Applications, and Numerics”, Acad. Press, 2004.
[21] Oluokun, F.A., Burdette, E.G. and Deatherage, J.H., “Elastic Modulus, Poisson’s Ratio, and Compressive Strength Relationship at Early Ages”, ACI Mater J, 1991, Vol. 88, No. 1, pp. 3-9.
[22] Carmichael, R.P., “Relationship between Young’s Modulus, Compressive Strength, Poisson’ Ratio, and Time for Early Age”, Swarth Colleg. Depart. Engin., 2009.
[23] Kenji, S., Hiroyuki, N., Shosuke, M. and Isao, N., “Behavior of Centrally Loaded Concrete Filled Steel-tube Short Columns”, J. Struct. Eng.-ASCE, 2004, Vol. 130, No. 2, pp. 180-188.
[24] American Concrete Institute (ACI) 209, “Prediction of Creep, Shrinkage, and Temperature Effects in Concrete Structures (ACI209R-92)”, ACI Committee 209R, 1992.
[25] Yi, S.T., Kim, J.K. and Oh, T.K., “Effect of Strength and Age on the Stress-strain Curve of Concrete Specimens”, Cem. Concr. Res., 2003, Vol. 33, No.8, pp. 1235-1244.

COMPUTATIONAL METHOD AND NUMERICAL SIMULATION OF TEMPERATURE FIELD FOR LARGE-SPACE STEEL STRUCTURES IN FIRE

Sheng-gang Fan [1,*], Gan-Ping Shu [1], Guang-Jun She [2], J.Y. Richard Liew [3]

[1] *School of Civil Engineering, Key Laboratory of Concrete and Prestressed Structures of Ministry of Education Southeast University, Nanjing, 210096, China*
[2] *Nanjing Architectural Design and Research Institute Co., Ltd., Nanjing, 210000, China*
[3] *Department of Civil engineering, National University of Singapore, Singapore, 117576, Singapore*
**(Corresponding author: E-mail: 101010393@seu.edu.cn)*

Received: 16 October 2012; Revised: 2 February 2013; Accepted: 16 December 2013

ABSTRACT: For large-space steel structures in fire, an accurate temperature field model is essential to predict the temperature distribution for response analysis of the structure. Based on the field model theories of air thermodynamics and heat transfer, the combustion process and temperature distribution of large-space steel structures in fire were analyzed in this paper. The temperature field model of large-space fire, including fire source, smoke plume and smoke layers models, was established. Closed form formulas were developed to predict the air temperature, within its application limit, near the ceiling of large-space steel structures in fire. The accuracy of the formulas was verified by comparing with results obtained from numerical method based on field models. This research provides an important theoretical basis for further studying the behavior of large-space steel structures in fire.

Keywords: Large-space steel structures, fire, temperature field, computational method, numerical simulation, thermodynamics, heat transfer

1. INTRODUCTION

Structures would be affected by fire, through energy transferred from uncontrolled combustion process. In large space fire, structures are firstly affected by heat from convection and radiation, and then the rise of structural temperature leads to additional thermal stresses due to boundary constraints and sharp decline of structural stiffness and strength. Under the influence of these combined actions and effect of materials in high temperature, structural damage or collapse may occur. One of the most significant preconditions of the whole process of analysis and design of large-space steel structures in fire is to establish an accurate temperature field model in fire to predict the temperature distribution in large structure.

Nowadays, researches on temperature field model are mostly focused on indoor small space fire, while studies on large space fire are not enough. Large space fire have many different attributes and features compared to indoor small space fire such as huge volume, higher space height, full combustion, faster air flow rate, larger heat distribution gradient, obvious local effects, and further distance from structural elements to fire source (Fan et al. [1]; Yu et al. [2]). Therefore, there may be great differences in the temperature field model for large and small space fire. Based on research findings by Li and Du [3], Xue et al. [4], Cooper [5] and Venkatasubbaiah and Jaluria [6], there are four available methods to establish air temperature field model in fire:

(1) The standard ISO834 fire, which is mainly suitable for indoor small space or compartment fire.
(2) Live fire test measuring method, which is mainly applicable to indoor large space fire. However, the testing is very rather costly, and the restricted test parameters often limit their applications.
(3) Analysis method based on zone models, which tend to be more accurate for fire at the initial fire development stage. However as the fire develops into a more mature stage, calculation deviation tends to accumulate leading less accurate prediction of temperature field.

(4)Numerical simulation method based on field models, which can accurately predict, in time and space, air temperature rise in a large space fire. This method may provide reliable analysis of temperature rise in structural members, and is applicable of capturing the entire process of combustion for the purpose of structural analysis at elevated temperature.

On the basis of theories on combustion, fluids and heat transfer, the motion of hot smoke and heat transfer of fire were analyzed in this paper, and the laws in combustion process were revealed. In addition, a mathematical model of air temperature field in large space fire was built. Finally, closed form formulas to predict the air temperature near the ceiling of large-space steel structures in fire was proposed.

2. COMBUSTION CHARACTERISTICS OF LARGE SPACE FIRE

A large space fire mainly undergoes four phases of combustion: initial growth, full development, stable burning and decay, among which the full development phase is the most important one as it has a profound influence on the temperature distribution and response of structure in large space fire. In this phase, as fire continues and flame height constantly increases, the hot air mixed with carbon black produced during combustion continually rises under the action of buoyancy, and forms a cylindrical smoke plume, as displayed in Figure 1. For large space fire which shows tendency towards stabilization, its temperature field model mainly includes models of fire source, smoke plume, and smoke layer.

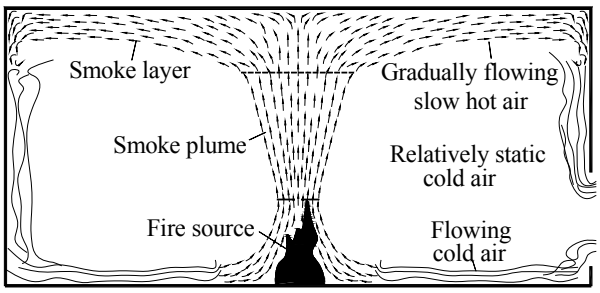

Figure 1. Sketch of Full Development Phase of Large Space Fire

2.1 Combustion Characteristics of Fire Source

Fire source is the only energy source in combustion process, and it exchanges heat with the air primarily by means of convection and radiation. The total heat amount released from fire source is the decisive factor of the temperature field.

The radiation heat generally comes from carbon black produced during combustion. In the initial phase of combustion, there is only 10 percent of the total heat released from fire source, because of relatively low indoor temperature. However, as temperature rises, and a large number of carbon black has been produced, the maximum radiation heat can reach about 15% ~20% of the total heat amount (Floyd et al. [7]; Chow and Yin [8]). In this paper, the radiation heat is taken as 20% of the total heat, and the convective heat is regarded as 80% of the total heat. Assuming the total heat amount released from fire source is Q, the convective heat and radiation heat will be Q_c and Q_e respectively, and then it is obvious that $Q = Q_c + Q_e$, and $Q_c = 0.8Q$.

2.2 Temperature Distribution of the Smoke Plume

As smoke plume rises, its volume expands by entraining surrounding cold air, pushing the boundary layer outwards, as shown in Figure 2. Assuming that the indoor air is isotropic and the

fire source is axisymmetric, the smoke plume will be similar to an inverted axisymmetric cone. The temperature distribution of smoke plume can be described as follows: (1) the highest temperature always locate in the centre whatever the cross section, and it decreases gradually to the lowest (approximately equals to room temperature) in the boundary layer, as displayed in Figure 2 (a), and (2) along the vertical direction, the centreline temperature falls down gradually with the height increasing, as shown in Figure 2 (b).

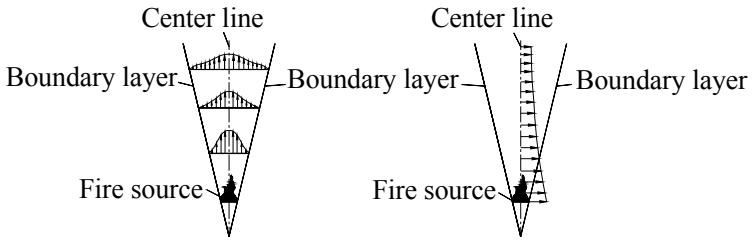

(a) Cross section (b) Centreline

Figure 2. Air Temperature Distribution of Smoke Plume

In the process of combustion, the relevant parameters of smoke plume, such as flow rate, temperature, and the density distribution, can be accurately simulated through fluid theory. The precondition of forming a stable smoke plume in large space fire is that the ceiling has a certain height. For large-space steel structures, if the height of ceiling exceeds 10m an obvious smoke plume will be developed (Li and Du [9]; Huang and Wen [10]).

2.3 Temperature Distribution of Smoke Layer

After the rising smoke plume collides with the ceiling of a large-space steel structure, an impact area is firstly formed, as illustrated in Figure 3. Additionally, the smoke plume moves horizontally to two sides, and the smoke layer is formed. The smoke layer contains most of the convective heat released from the fire source. Therefore, for large-space steel structures, the temperature of structure and components are influenced by temperature distribution of the smoke layer directly. It is important to capture the temperature distribution of this smoke layer for the analysis of structural fire resistance.

The temperature distribution law in smoke layer can be described as follow (Shi et al. [11]; Cooper and Stroup [12-13]):

(1) The temperature declines step by step from the centreline of impact area to surrounding areas. The impact area exhibits great air temperature gradient along horizontal direction, and obvious local effects.
(2) As burning continues, the smoke layer accumulates more heat and increases its thickness gradually.
(3) For thickness direction of the smoke layer, the temperature falls down gradually as the height decreases, until it meets the indoor temperature.
(4) With heat release rate declining, the increment of temperature and thickness gradually drops, and the smoke layer comes to be stable.

Figure 3 illustrates the temperature distribution of the smoke layer at the ceiling of large-space steel structures.

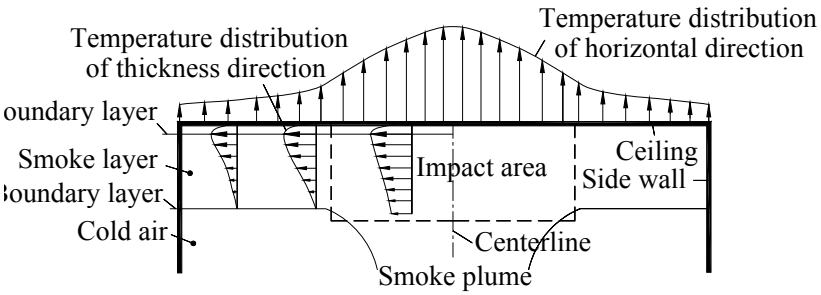

Figure 3. Temperature Distribution of the Smoke Layer

3. TEMPERATURE FIELD MODEL OF LARGE SPACE FIRE

3.1 Model of Fire Source

The fire source model is defined as the relationship between the heat release rate and the burning time. The crucial parameters include the fire load density, the burning rate of the fire source, the maximum heat release rate, the burning area, the flame height, and the burning time. However, the complex combustion process with great randomness in variety, mass, and distribution of the combustibles, makes it difficult to determine the fire source model, and parameters precisely. Nowadays, the method combines mathematical statistics with experimental research is widely adopted by researchers in this field.

3.1.1 Fire load density

Fire load density q_{F} is defined as the heat released by the fire source per unit burning area per unit time, which depends on the variety, mass and distribution of the combustibles. Relevant statistical analysis of fire date by Harmathy [14], Anon [15], and Vrouwenvelder [16) revealed that there is a great difference in the value of fire load density for various building functions, such as residence, office, and school, in different countries.

Sunil and Kameswara [17] prescribed that the fire load density could be taken as $q_{\mathrm{F}} = 500\,\mathrm{kJ/m^2}$ for malls and other public places, as well as warehouses of supermarkets. The large space structures studied in this paper are public buildings for commercial use, so the fire load density is chosen as $q_{\mathrm{F}} = 500\,\mathrm{kJ/m^2}$.

3.1.2 Burning rate of the fire source

The burning rate of the fire source reveals the relationship between heat release rate of the fire source and burning time, which depends on the variety of combustibles and the indoor ventilation conditions. Considering large space fire, the heat release rate of the fire source is basically proportional to the square of burning time (Harmathy and Mehaffey [18]), expressed by

$$Q(t) = \begin{cases} \alpha t^2 & 0 < t \le t_{\mathrm{p}} \\ Q_{\max} & t > t_{\mathrm{p}} \end{cases} \tag{1}$$

where $Q(t)$ is the heat release rate of the fire source at a certain time (MW), $Q_{\max}$ is the maximum heat release rate of the fire source (MW), α is the increasing coefficient of the heat

release rate (kW/s^2), which is determined according to the fire growth rate in Table 1, and t is the burning time (s); $t_p = \sqrt{Q_{max}/\alpha}$ is the time of the heat release rate reaching the maximum value(s).

Table 1. Increasing Coefficient of Heat Release Rate α (kW/s^2)

Burning rate of the fire source	Slow	Medium	Fast	Very fast
Coefficient α	0.002931	0.011270	0.046890	0.187800

3.1.3 Maximum heat release rate

The maximum heat release rate Q_{max} is influenced by the variety of combustibles, the building function, and the fire-fighting facilities. In this paper, based on the research findings from She [19], the values of Q_{max} are taken as 5MW, 10MW, 15MW, 20MW, e and 25MW respectively which corresponding to different building enclosures as illustrated in Table 2.

Table 2. Maximum Heat Release Rate for Different Building Enclosures

Values of Q_{max}	Fire severity	Fire-fighting facility	Building Enclosures
5 MW	Mild	With sprinkler	Waiting room, gymnasium and other public buildings
10 MW	Medium	No sprinkler	Waiting room, gymnasium and other public buildings
15 MW	Relatively severe	With sprinkler	Shopping malls, supermarkets, warehouses, libraries and other large space buildings
20MW	Severe	No sprinkler	Shopping malls, supermarkets, warehouses, libraries and other large space buildings
25 MW	Extremely severe	—	large-space steel structures that contain a large number of flammable and explosive chemicals

3.1.4 Burning area and flame height

The spread of the burning surface is affected by many factors with certain randomness. In order to simplify the calculation, it is assumed that the boundary of the fire source in large space fire advances to all directions at the same rate, and the burning surface has the same heat release rate. Therefore, the shape of the fire source model can be regarded as an axisymmetric cone [20], which is shown in Figure 4. The burning area and the flame height per unit time can be obtained as

$$A = \pi(D/2)^2 = Q(t)t/q_F \quad ; \quad L = 0.235Q(t)^{2/5} - 1.02D \tag{2}$$

where A is the burning area of the fire source per unit time (m^2); D is the diameter at the bottom of the fire source model per unit time (m); L is the flame height per unit time (m); t represents the burning time, which is taken as 1s.

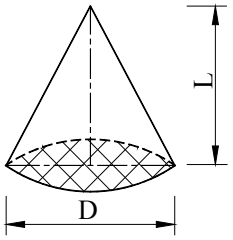

Figure 4. Simplified Model of the Fire Source

When the maximum heat release rate is reached, for example, $Q(t)=Q_{\max}$, A and L for different fire scenarios can be obtained from Eq. 2.

3.1.5 Burning duration

The burning duration t_{m} is defined as the total time taken from the initiation of the fire to its natural extinguishment, as shown in Figure 5 (a).

Based on the principle of energy conservation, the total amount of heat released from the fire source should be equal to the integral of the heat release rate $Q(t)$ throughout the burning duration, which is demonstrated as the shaded area in Figure 5 (a). In order to simplify calculation, the descending curve in the extinguishing phase may be approximated by an equivalent vertical line according to the conservation of the total heat, as shown in Figure 5 (b).

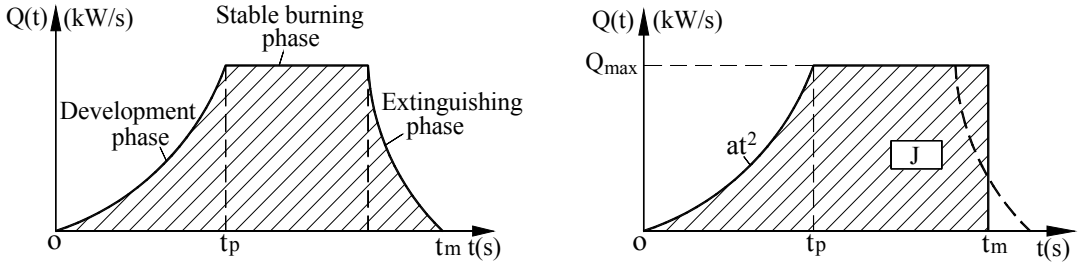

(a) Actual model (b) Simplified model

Figure 5. The Relationship between Heat and Duration of Fire

From Figure 5 (b), the total amount of heat J released from the fire source can be derived by solving the integral of Eq. 3.

$$J=q_F A=\int_0^{t_{\mathrm{m}}} Q(t)\mathrm{d}t=\int_0^{t_{\mathrm{p}}} \alpha t^2\mathrm{d}t+\int_{t_{\mathrm{p}}}^{t_{\mathrm{m}}} Q_{\max}\mathrm{d}t=\alpha t_{\mathrm{p}}^3/3+Q_{\max}\left(t_{\mathrm{m}}-t_{\mathrm{p}}\right) \tag{3}$$

in which

$$t_{\mathrm{m}}=t_{\mathrm{p}}+\left(q_{\mathrm{F}}A-\alpha t_{\mathrm{p}}^3/3\right)/Q_{\max} \tag{4}$$

where $A=\sum_{\mathrm{i}}\left(m_{\mathrm{i}}q_{\mathrm{i}}\right)/q_{\mathrm{F}}$ is the equivalent area after normalizing the heat release rate of all combustibles according to q_{F}; m_{i} and q_{i} are, respectively, the total mass of the i type of combustibles (kg), and the heat release rate per unit mass ($\mathrm{kJ/kg}$).

Based on the test data from Chow et al. [21] and William [22], for large space fire the total mass of combustibles ranges from 200 to 2000 kg and the average heat release rate per unit mass is approximately 25×10^3 kJ/kg. In addition, corresponding to five values of Q_{max} = 5MW, 10MW, 15MW, 20MW, and 25MW, the burning duration t_m for different mass of combustibles and different fire growth rates can be calculated from Eq. 4. The calculation results are shown in Figure 6.

The results in Figure 6 demonstrate that the burning duration t_m would rarely exceed 80 minutes (see curves of FS-10, VS-25 and so on), if the total mass of combustibles is lower than 2000kg. Only when the value of Q_{max} is 5MW, and the mass of combustibles exceeds 1400kg, the burning duration t_m can reach and even more than 120 minutes (see curves of SS-5, MS-5, FS-5, and VS-5). Therefore, it is proposed that the burning duration of large space fire can be taken conservatively as $t_m = 120$ min.

3.2 Model of Smoke Plume

The smoke plume model mainly depends on the distribution in time and space of flow rate, density, temperature, and other state parameters of the smoke, as shown in Figures 7 (a) to (c). According to previous discussion, the shape of the smoke plume is similar to an inverted axisymmetric cone, and thus its motion equation can be derived with the cylindrical coordinates system. The rising direction and the radial direction of smoke plume are assumed as the z and r axis respectively, and the corresponding flow rates to two axes are u and v separately. Based on the principles of mass conservation (the continuity equation), momentum conservation (the motion equation), and energy conservation (the energy equation) of the smoke plume, the differential equations of smoke plume are obtained as follows (Motevalli [23]; Zukoski et al. [24]).

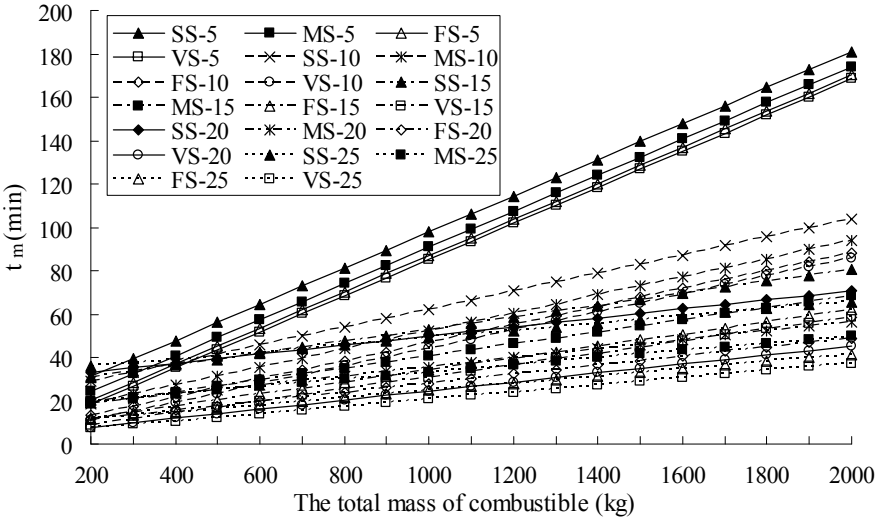

Figure 6. The Burning Duration of Fire t_m
(SS represents slow, MS represents the medium, FS represents fast, VS represents very fast, as shown in Table 1)

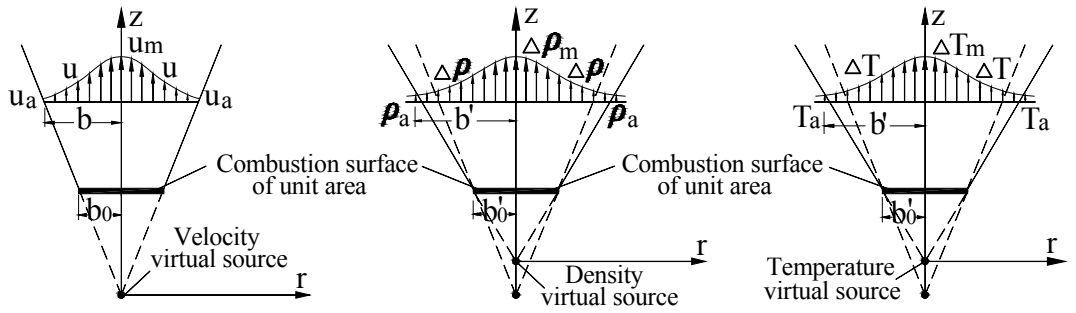

(a) Flow rate distribution (b) Density distribution (c) Temperature distribution

Figure 7. Actual Distribution of State Parameters

Continuity equation: $$\partial u/\partial z+\partial v/\partial r+v/r=0 \tag{5a}$$

Motion equation: $$u\frac{\partial u}{\partial z}+v\frac{\partial v}{\partial r}=-g-\frac{1}{\rho}\frac{\partial p}{\partial z}-\frac{1}{r}\frac{\partial}{\partial r}(r\overline{uv}) \tag{5b}$$

Energy equation: $$u\frac{\partial \Delta T}{\partial z}+v\frac{\partial \Delta T}{\partial r}=-\frac{1}{r}\frac{\partial}{\partial r}(r\overline{u\Delta T}),\ u\frac{\partial \Delta \rho}{\partial z}+v\frac{\partial \Delta \rho}{\partial r}=-\frac{1}{r}\frac{\partial}{\partial r}(r\overline{u\Delta \rho}) \tag{5c}$$

where $\Delta T=T_a-T$, $\Delta\rho=\rho_a-\rho$.

Considering a unit volume of the smoke along the symmetry axis, the differential equations are solved with boundary conditions and assumptions. The air temperature T_m along the centreline of the smoke plume can be expressed as (Gershuni et al. [25]):

$$T_m=T_a+11.21\times V_0^{2/3}\left[\left(\rho_a-\rho_0\right)g/\rho_a\right]^{-1/3}z^{-5/3}\left(T_0-T_a\right) \tag{6}$$

where T_m is the air temperature at the point where the vertical distance along the centreline is z from the fire source (^oC); T_0 is the air temperature of the burning surface (^oC); T_a is the indoor temperature (^oC); ρ_a and ρ_0 are, respectively, the density of the surrounding air, and the initial density of the burning surface (kg/m^3); g is the acceleration of gravity (m/s^2); V_0 is the volume flux across a certain cross section of the smoke plume.

Assuming that the heat release rate on the burning surface is evenly distributed, the rising velocity, density, and temperature of the surrounding air would also approximately follow uniform distribution, as demonstrated in Figures 8(a) to (c). Ignoring the influence of the sudden change of the parameters around the circumference of the burning surface, the following formula can be obtained.

$$Q_c=q\Delta t=c_p m_0\left(T_0-T_a\right) \tag{7}$$

where Q_c is the convective heat release rate of the fire source ; Δt is the time duration of the heating process; c_p is the coefficient of the specific heat at constant pressure for air; m_0 is the mass of the heated air, and q is the heat release rate of the fire source per unit area.

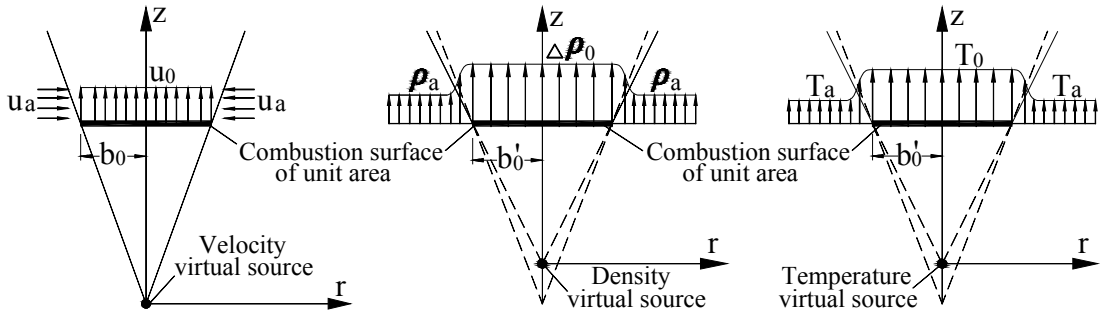

(a) Velocity distribution (b) Density distribution (c) Temperature distribution

Figure 8. Simplified Distribution of State Parameters

It can be obtained from Figure 8(a) that $m_0 = \pi b_0^2 u_0 \Delta t \rho_0$, $V_0 = \pi b_0^2 u_0$. Introducing them into Eq. 7, the following relationship can be obtained:

$$q = c_p \pi b_0^2 u_0 \rho_0 (T_0 - T_a) \quad , \quad V_0 = q / c_p \rho_0 \left(T_0 - T_a\right) \tag{8}$$

Introducing Eq. 8 into Eq. 6, the following formula can be derived.

$$T_m = T_a + 11.21 \times \left[\frac{\rho_a (T_0 - T_a)}{g c_p^2 \rho_0^2 (\rho_a - \rho_0)} \right]^{1/3} q^{2/3} z^{-5/3} \tag{9}$$

Introducing a virtual temperature source, which is demonstrated in Figure 9, the burning area can be extended from a unit area to the whole surface. Therefore, replacing the heat release rate per unit area q with the total heat release rate Q_c in Eq. 9, the air temperature can be expressed as:

$$T_m = T_a + 11.21 \times \left[\frac{\rho_a (T_0 - T_a)}{g c_p^2 \rho_0^2 (\rho_a - \rho_0)} \right]^{1/3} Q_c^{\,2/3} (z + z_0)^{-5/3} \tag{10}$$

where z_0 is the vertical distance between the virtual temperature source and the fire source. Using Eq. 10 and $T_m = T_0$, the position of the virtual temperature source is expressed by

$$z_0 = 4.26 \times \left[\frac{\rho_a Q_c^{\,2}}{g c_p^2 \rho_0^2 (\rho_a - \rho_0)(T_0 - T_a)^2} \right]^{1/5} \tag{11}$$

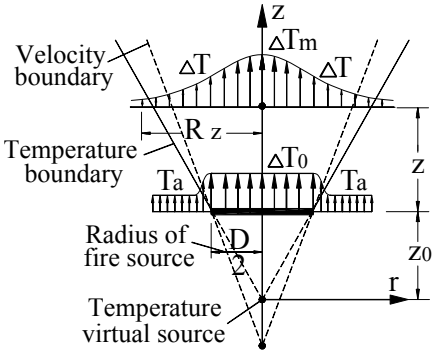

Figure 9. Distribution of Temperature in the Smoke Plume

According to the parameter changes with temperature of thermal physical properties of air at normal pressure, and the burning test results of different combustibles (Guan[26]), the flame temperature of most fibrous combustibles is $1200^{\circ}\mathrm{C}$. Therefore introducing $T_0 = 1200^{\circ}\mathrm{C}$, $\rho_0 = 0.2322\,\mathrm{kg/m^3}$, $\rho_a = 1.1614\,\mathrm{kg/m^3}$, $c_p = 1.230\,\mathrm{kJ/m^3}$, $T_a = 23^{\circ}\mathrm{C}$, $g = 9.8\,\mathrm{m/s^2}$, and $Q_c = 0.8Q$ into Eq. 10 and 11, the following formulas can be obtained.

$$T_m = T_a + 119.15 \times Q^{2/3}(z + z_0)^{-5/3} \tag{12a}$$

$$z_0 = 0.25Q^{2/5} \tag{12b}$$

Based on the similarity principle of the smoke plume model (Fang et al. [27]), the distribution of temperature difference can be described as follow.

$$\Delta T/\Delta T_m = (T_r - T_a)/(T_m - T_a) = \exp[-Pr(r/b)^2] \tag{13}$$

where T_r is the air temperature of the smoke plume (^{o}C); Pr is the Prandtl number of air, which may be taken as 0.72 according to Guan [26]; b is the half width of the temperature field at the position where the vertical distance is z from the fire source, $b = 0.102 \times (z + z_0)$. Introducing Eq. 12a into Eq. 13 yields:

$$T_r = T_a + \exp\left[-67.28 \times r^2/(z + z_0)^2\right]\left[119.15 \times Q_c^{2/3}(z + z_0)^{-5/3}\right] \tag{14}$$

By varying the total heat release rate Q_c as 5MW, 10MW, 15MW, 20MW, and 25MW, and the vertical height z from 0 to 20m, air temperature of the smoke plume T_m along the centreline of the fire source can be obtained from Eq. 12a and Eq. 12b and they are plotted in Figure 10. Figure 11 plots the results of the radical temperature profile of the smoke plume using Eq. 14.

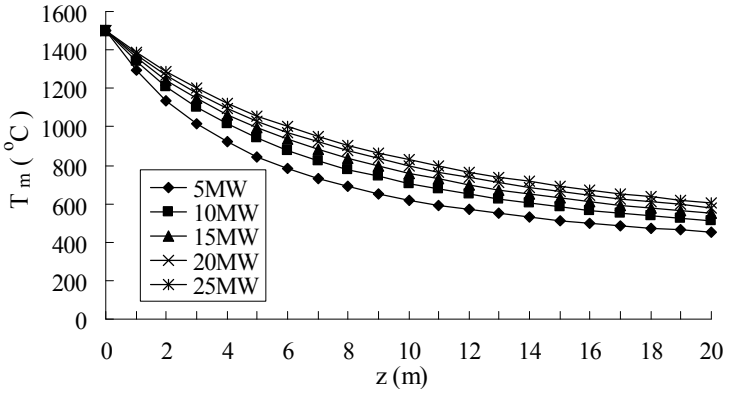

Figure 10. $T_m - z$ Curves of Smoke Plume along the Centreline of Fire Source

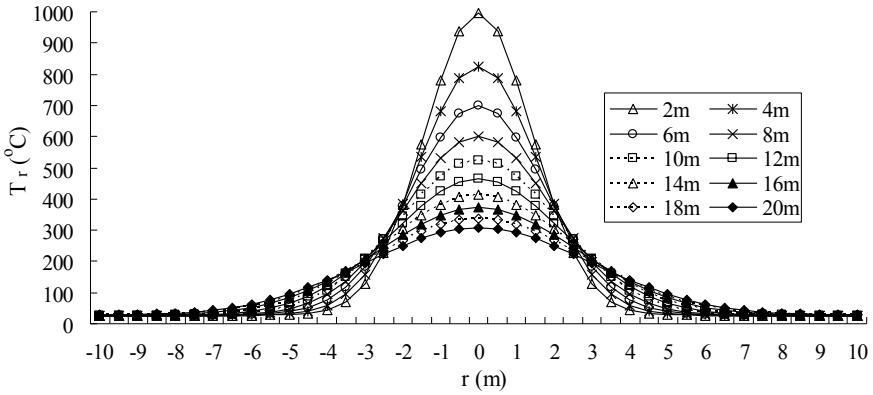

Figure 11. $T_r - r$ Curves of Smoke Plume at Different Heights for $Q_c = 20\text{MW}$

According to Eq. 15a and Eq. 15b, the maximum centreline flow rate of the hot air u_m can be solved.

$$v_n^2 - v_{n-1}^2 = 2a_m \Delta h \tag{15a}$$

$$v_n = v_{n-1} + a_m \Delta t \tag{15b}$$

where v_n and v_{n-1} is the flow rates of air at different heights of the smoke plume; α_m is the rising acceleration of the smoke plume; Δh and Δt are, respectively, the height step, and the time step for iteration.

Considering the value of total heat release rate Q_c as 5MW, 10MW, 15MW, 20MW, and 25MW respectively, and the vertical height z ranges from 0 to 20m, based on Eq. 15a and Eq. 15b, the maximum centreline flow rate u_m of the hot air in the smoke plume can be solved with iteration method, as displayed in Figure 12.

The curves in Figure 12 demonstrate that u_m is basically in linear relationship with the logarithm of height *z*. With data fitting, as displayed in Figure 12, the maximum flow rate u_m can be expressed as follows.

$$u_m = C_1 \ln z + C_2 \tag{16}$$

where C_1 and C_2 are the fitting coefficients, their values are demonstrated in Table 3.

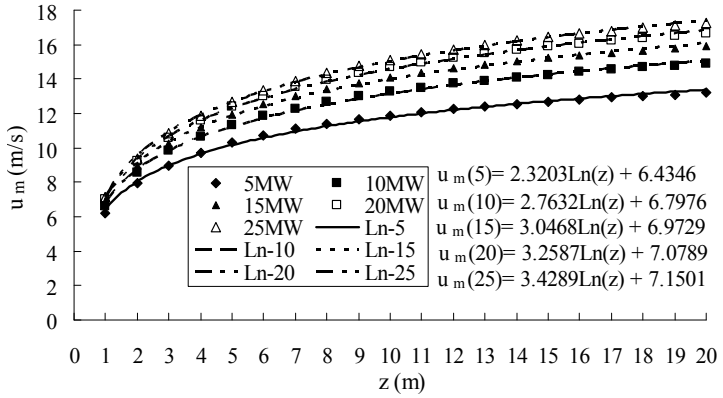

Figure 12. $u_m - z$ Curves (Where Ln is the Fitting Curves)

Table3. The Value of C_1 and C_2

Total heat release rate Q_c	5MW	10MW	15MW	20MW	25MW
Coefficient C_1	2.3203	2.7632	3.0468	3.2587	3.4289
Coefficient C_2	6.4346	6.7976	6.9729	7.0789	7.1501

Based on the similarity principle of the smoke plume model (Harmathy and Mehaffey [18]), the following formula can be obtained.

$$u/u_{\mathrm{m}} = \exp[-(r/b)^2] \tag{17}$$

where u represents the air flow rate of the smoke plume at a certain time.

Introducing Eq. 16 into Eq. 17, solving the integral, the relationship between $\bar{u}$ and u_{m} along the centreline can be expressed as

$$\bar{u} = \frac{1}{\pi b^2}\int_0^{2\pi}\int_0^b u_{\mathrm{m}} \exp(-r^2/b^2) r \mathrm{d}\theta \mathrm{d}r = (1-e^{-1})u_{\mathrm{m}} = (1-e^{-1})\left(C_1 \ln z + C_2\right) \tag{18}$$

3.3 Model of Smoke Layer

In large space fire, the hot air flow is primarily divided into three areas: the smoke plume area, the impact area, and the ceiling jet area, which are demonstrated in Figure 13. In area A, the flow characteristics and the temperature distribution are detailed in section 3.2. In area B, the motion direction of the smoke plume changes significantly, which creates certain pressure gradients. The smoke in the top of this area flows nearly parallel to the ceiling. In area C, the hot smoke continually diffuses to surrounding areas from the centreline of the fire source as the circle centre.

3.3.1 Air temperature distribution of impact area

The temperature, flow rate, density, and pressure of the hot smoke change significantly in the impact area. According to the test results of inverted axisymmetric smoke layer in large space fire from Beltao and Rajaratnam [28], the range of the impact area in large space fire is about $0.86H \le z \le H$, in which H is the distance between the burning surface and the ceiling, as shown in Figure 1.

According to Figure 14, assuming a micro unit of the hot smoke along the centreline, the pressure difference Δp between the upper and lower surfaces in the impact area can be derived as:

$$\Delta p = p_{\mathrm{s}} - p_{\mathrm{a}} = 0.2\left(\rho_{\mathrm{a}} - \rho\right) gH + 0.5\rho u_0^2 \tag{19}$$

where p_{s} is the pressure at the stagnation point in the impact area; p_{a} is the pressure at the bottom of the impact area; ρ_{a} is the indoor air density; ρ_0 is the air density at the bottom of the impact area; u_0 is the maximum centreline flow rate of the hot air at the bottom of the impact area.

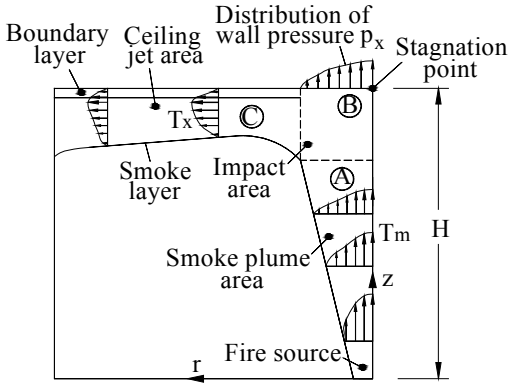

Figure 13. Partition of Smoke Layer

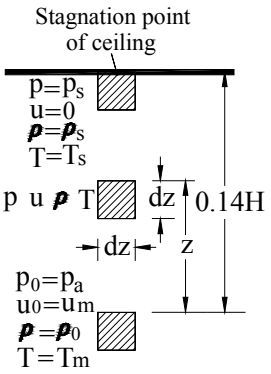

Figure 14. Micro Unit of Hot Smoke

According to the parameter changes with temperature of thermal physical properties of air (Guan [26]), it can be fitted that $\rho \approx 356/T_{0.86\mathrm{H}}$. Using formula (12a), (12b), and (16), $T_{0.86\mathrm{H}}$, z_0, u_0, and ρ can be obtained. Substituting these into Eq. 19, the curves of the pressure difference Δp for different heat release rates Q_c can be obtained, as shown in Figure 15.

In the impact area, because the hot air entrains little cold air, its density barely changes, and the temperature is approximately proportional to the pressure. $\Delta p - z$ Curves in Figure 15 point out that the pressure difference Δp of the hot air at the stagnation point is below $100\,\mathrm{N/m^2}$, and the relative value $\Delta p/p_\mathrm{a} = 100/\left(1.0\times10^5\right) = 0.1\%$ is small. Therefore the influence of the pressure on the temperature is not significant. According to Eq. 12a, the air temperature at the stagnation point near the ceiling can be expressed by relationship.

$$T_H = T_{0.86H} = T_\mathrm{a} + 119.15\times Q_\mathrm{c}^{2/3}\left(0.86H + z_0\right)^{-5/3} \tag{20}$$

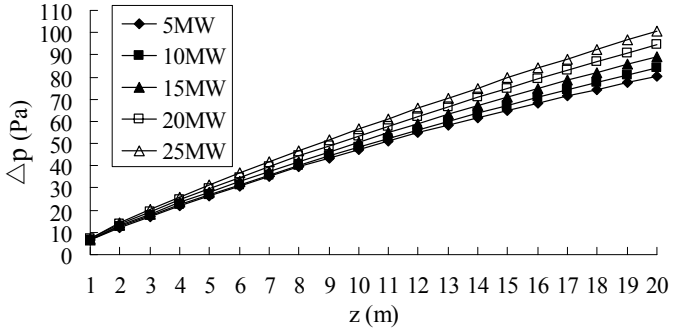

Figure 15. $\Delta p - z$ Curves for Different Values of Q_c

According to the test results from (Beltao and Rajaratnam [28], the air pressure near stagnation point can be approximately described by:

$$\Delta p/\Delta p_\mathrm{s} = \exp\left[-0.693\left(r/b\right)^2\right] \tag{21}$$

Because of the proportional relationship of air temperature with pressure in the impact area, the temperature distribution near the stagnation point can be expressed as:

$$\left(T_\mathrm{r} - T_\mathrm{a}\right)/\left(T_\mathrm{H} - T_\mathrm{a}\right) = \exp\left[-0.693\left(r/b\right)^2\right] \tag{22}$$

Introducing Eq. 20 into Eq. 22, the air temperature in the impact area can be obtained as

$$T_r = T_a + \exp\left[-0.693\left(r/b\right)^2\right] \times 119.15 \times Q_c^{2/3}\left(0.86H + z_0\right)^{-5/3} \tag{23}$$

where r is the horizontal distance from a certain point near the ceiling to the centreline of the fire source; $b = D(z + z_0)/2z_0$ is the half width of the temperature field in the impact area; D is the diameter of the fire source; z_0 is the vertical distance between the virtual temperature source and the fire source; T_a is the indoor temperature.

3.3.2 Air temperature distribution of ceiling jet area

Taking the radius of burning zone ($r = 0.5D$) as the demarcation point of impact area and ceiling jet area, Eq. 22 takes the following form.

$$\left(T_{D/2} - T_a\right)/\left(T_H - T_a\right) = \exp\left[-0.693\left(0.5D/b\right)^2\right] = \exp\left[-0.693\, z_0^2/\left(z + z_0\right)^2\right] \tag{24}$$

Considering the similarity principle of smoke plume model, the temperature difference in ceiling jet area can also be described as:

$$\left(T_r - T_a\right)/\left(T_{D/2} - T_a\right) = \exp\left[-\left(u_m^2/u_{D/2}^2\right)^{1.12Pr}\right] = \exp\left[-\left(r - 0.5D\right)/\left(0.5D\right)\right]^{2.24Pr} \tag{25}$$

Letting Prandtl constant as $Pr \approx 0.72$, Eq. 24 multiplied by Eq. 25 yields

$$\left(T_r - T_a\right)/\left(T_H - T_a\right) = \exp\left[-\left(r - 0.5D\right)^{1.6}/\left(0.5D\right)^{1.6} - 0.693\, z_0^2/\left(z + z_0\right)^2\right] \tag{26}$$

Introducing Eq. 20 into Eq. 26, the air temperature in ceiling jet area can be obtained as

$$T_r - T_a = \exp\left[-\left(r - 0.5D\right)^{1.6}/\left(0.5D\right)^{1.6} - 0.693\, z_0^2/\left(z + z_0\right)^2\right] \times 119.15 \times Q_c^{2/3}\left(0.86H + z_0\right)^{-5/3} \quad r > 0.5D \tag{27}$$

3.3.3 Temperature distribution of smoke layer

Eq. 23 may be used for calculating the air temperature in the impact area, and Eq. 27 is for calculating the air temperature in the ceiling jet area. Combining Eq. 23 with Eq. 27, the air temperature of the smoke layer in large space fire can be obtained.

$$T_r - T_a = \begin{cases} \exp\left[-\left(r - 0.5D\right)^{1.6}/\left(0.5D\right)^{1.6} - 0.693\, z_0^2/\left(z + z_0\right)^2\right] \times 119.15 \times Q_c^{2/3}\left(0.86H + z_0\right)^{-5/3} & r > 0.5D \\ \exp\left[-0.693\, z_0^2/\left(z + z_0\right)^2\right] \times 119.15 \times Q_c^{2/3}\left(0.86H + z_0\right)^{-5/3} & r \le 0.5D \end{cases} \tag{28}$$

Figures 16(a) and 16(b) display the air temperature distribution of the smoke layer when the value of heat release rate Q_c is 5MW and 20MW respectively. For the ceiling height $H = 10\text{m}$, and different Q_c values of 5MW, 10MW, 15MW, 20MW, and 25MW, the radial air temperature profile of the smoke layer is plotted as shown in Figure 17. In addition, for $H = 10\text{m}$ and $Q_c = 20\text{MW}$, the vertical air temperature profile for different distances from centreline is shown in Figure 18.

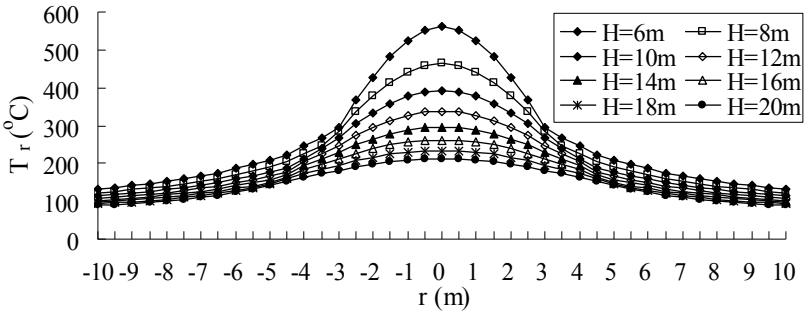

(a) $Q_c = 5\text{MW}$

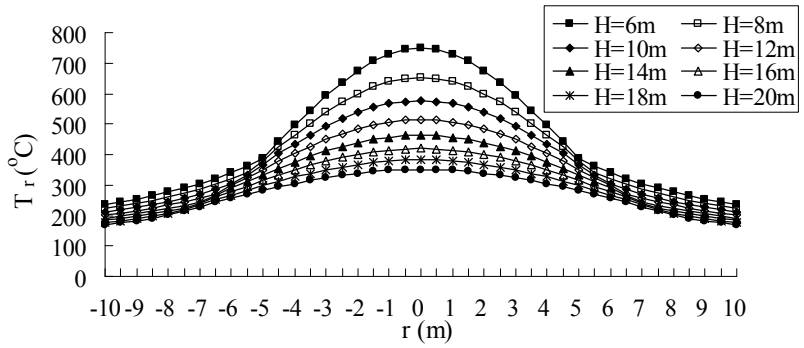

(b) $Q_c = 20\text{MW}$

Figure 16. Radial Air Temperature Profile of Smoke Layer

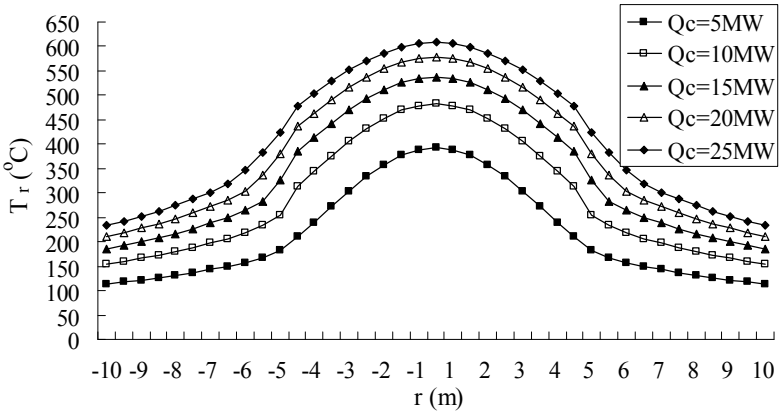

Figure 17. Radial Air Temperature Profile of Smoke Layer for Different Heat Release Rates ($H = 10\text{m}$)

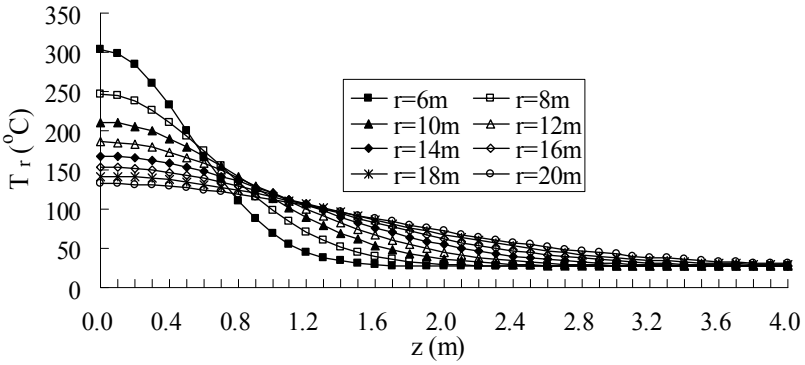

Figure 18. Vertical Air Temperature Profile of Smoke Layer at Distance r from Centreline ($H = 10\text{m}, Q_c = 20\text{MW}$)

Figure 18 shows that with the increasing time of fire, the hot smoke will accumulate in the upper space, and the smoke layer will be thicken ceaselessly.

4. CALCULATION OF AIR TEMPERATURE NEAR THE CEILING OF LARGE SPACE

4.1 Modified Temperature Model in Smoke Layer

Eq. 28 describes the air temperature distribution in the smoke layer near the ceiling of large space based on the assumption that the indoor space of large space structures is infinite. However, since most large space fire occurs in a limited space, the air temperature distribution in the smoke layer will be affected by the following three factors (Bai et al. [29]; Jin et al. [30]). (1) Limited space: since walls and other surfaces in limited space block the flow of the hot smoke, the smoke will continually accumulate near the top of the indoor space, and affect the temperature distribution. (2) Time lag: due to the large volume of the indoor space, time is needed for the rising of hot air from the fire source to the ceiling, leading to obvious time lag phenomenon in temperature field of smoke layer. (3) Temperature uniformity degree: limited by walls and other surfaces, back flow and convection of hot smoke will take place in smoke layer, in this sense, cold air and hot air mix constantly, which averages and uniformizes the air temperature near the ceiling. The influences of the three factors on the air temperature near the ceiling of large-space steel structures will be discussed in the following sections.

4.1.1 Coefficient of limited space

In Reference 3, the simulation software FDS of temperature field was applied to analyze a series of fire scenarios with different indoor areas, and different ceiling heights in large space. Considering the air temperature at the stagnation point near the ceiling, Table 4 shows the relevant experimental results in detail.

Table 4. Experimental Result of Air Temperature at the Stagnation Point of Ceiling

Height of ceiling / Indoor area A (m^2)	$Q_c = 5$MW						$Q_c = 25$MW					
	H (m)						H (m)					
	4	6	9	12	15	20	4	6	9	12	15	20
500	603	573	573	573	553	463	1153	1063	1053	1053	1053	913
1000	503	503	503	483	443	423	1103	973	933	903	883	853
3000	503	453	413	413	403	393	933	903	803	753	723	623
6000	433	413	393	383	373	353	833	813	753	683	653	613

When the indoor area is 6000 m^2, the indoor space is large enough to be supposed as an infinite space. Therefore, for 6000 m^2 in Table 4, dividing the experimental results by those respectively, the ratio (the coefficient of limited space γ_s) of the air temperature at the stagnation point in limited space to infinite space could be obtained in detail in Table 5.

Table 5 demonstrates that the coefficient of limited space γ_s mainly depends on the indoor area, the height of ceiling, and the heat release rate. For small indoor area, $\gamma_s \to \infty$; while for infinite space, $\gamma_s \to 1.0$. Fitting the data in Table 5, as displayed in Figures 19 (a) and (b), the coefficient of limited space γ_s can be approximately expressed as:

$$\gamma_s = 1 + Q_c^{0.2} \exp\left(-0.1A^{0.5} / H^{0.3}\right) \tag{29}$$

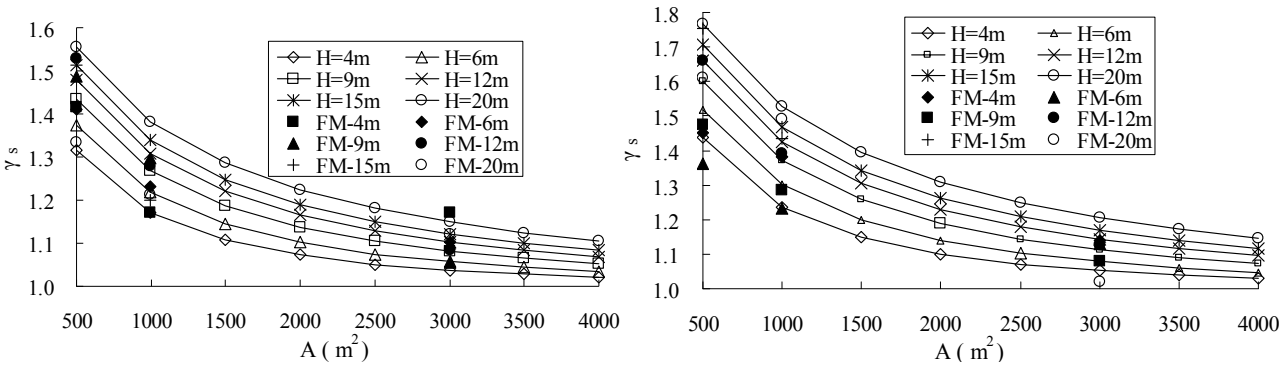

(a) $Q_c = 5$MW (b) $Q_c = 25$MW

Figure 19. Comparison of the Fitting Curves with Experimental Data of the Coefficient γ_s (FM for the Data in Table 5)

Table 5. Ratio of Air Temperature at the Stagnation Point of Ceiling in Limited Space to Infinite Space

Height of ceiling / Indoor Area A (m^2)	$Q_c = 5$MW						$Q_c = 25$MW					
	H (m)						H (m)					
	4	6	9	12	15	20	4	6	9	12	15	20
500	1.42	1.41	1.49	1.52	1.52	1.33	1.45	1.36	1.47	1.66	1.75	1.61
1000	1.17	1.23	1.30	1.28	1.20	1.22	1.38	1.23	1.28	1.39	1.43	1.49
3000	1.17	1.10	1.05	1.08	1.09	1.12	1.14	1.13	1.08	1.13	1.13	1.02
6000	1.00	1.00	1.00	1.00	1.00	1.00	1.00	1.00	1.00	1.00	1.00	1.00

The curves in Figures 19 (a) and (b) shows the relationships between the coefficient γ_s with the indoor area A, ceiling height H, and heat release rate Q_c. For regular structure fire, when heat release rate $Q_c \le 25$MW, and indoor area is about 4000 m^2, the influence of limited space on the increasing of temperature is less than 10%.

4.1.2 Coefficient of time lag

The air temperature basically increases basically with the burning time. For large space fire, the coefficient of time lag γ_t is defined as the degree of the air temperature increase lagging behind the growth of heat release rate, which is expressed by the following formula (Li and Du [3]).

$$\gamma_t = 1 - 0.8\exp\left(-\mu t\right) - 0.2\exp\left(-0.1\mu t\right) \tag{30}$$

where t is the burning duration; μ is the coefficient, which depends on the fire growth rate, the maximum heat release rate, the height of ceiling, and the indoor area. As the large space fire in public structures is rapid growth type, μ takes the values in Table 6.

Table 6. The Value of Coefficient μ

Maximum heat release rate Q_c	5MW	10MW	15MW	20MW	25MW
Coefficient μ	0.0030	0.0024	0.0020	0.0018	0.0016

4.1.3 Coefficient of temperature uniformity degree

The coefficient γ_a represents the temperature uniformity degree, and $f(r)$ describes the temperature distribution of air flow near the ceiling of an infinite space. According to Eq. 28, considering the temperature uniformity degree, the air temperature near the ceiling can be described as follows.

$$T_r - T_a = \left[\gamma_a + (1-\gamma_a) f(r)\right] \times 119.15 \times Q_c^{2/3} (0.86H + z_0)^{-5/3} \tag{31}$$

$$f(r) = \begin{cases} \exp\left[-0.693(r/b)^2\right] & r \le 0.5D \\ \exp\left[-(r-0.5D)^{1.6} / (0.5D)^{1.6} - 0.693 z_0^2 / (z+z_0)^2\right] & r > 0.5D \end{cases} \tag{32}$$

According to Eq. 31, for $t = 0$, $\gamma_a = 0$; for $t \to \infty$, $\gamma_a = 1$.

Li and Du [3] carried out numerical simulation using FDS software for 120 cases of fire scenarios and provides the coefficient of temperature uniformity degree γ_a for different heat release rates, different ceiling heights, and different indoor areas, as detailed in Table 7.

According to Table 7, it can be concluded that, based on the same burning duration, larger indoor area will lead to smaller the coefficient γ_a. Higher the ceiling leads to larger γ_a value; and the larger the heat release rate leads to the smaller coefficient γ_a. In addition, among the three factors, the indoor area A has the most influence on coefficient γ_a, and the height of ceiling H has the second most influence, the heat release rate Q_c has the least influence and hence it is ignored in this paper.

Table 7. The Value of Coefficient γ_a

H (m)	$Q_c = 2$MW				$Q_c = 5$MW				$Q_c = 25$MW			
	A (m^2)				A (m^2)				A (m^2)			
	500	1000	3000	6000	500	1000	3000	6000	500	1000	3000	6000
4	0.60	0.40	0.30	0.15	0.75	0.60	0.30	0.20	0.60	0.40	0.30	0.20
6	0.60	0.50	0.40	0.20	0.60	0.70	0.45	0.30	0.80	0.50	0.35	0.26
9	0.65	0.55	0.45	0.40	0.75	0.60	0.60	0.40	0.55	0.60	0.50	0.30
12	0.70	0.60	0.45	0.30	0.75	0.65	0.60	0.40	0.60	0.60	0.50	0.40
15	0.80	0.70	0.55	0.40	0.70	0.75	0.55	0.45	0.70	0.60	0.55	0.40
20	0.85	0.70	0.60	0.40	0.75	0.70	0.60	0.55	0.70	0.60	0.65	0.45

Fitting the data in Table 7, as displayed in Figure 20, coefficient γ_a can be expressed as follows:

$$\gamma_a = 1 - \exp\left(-0.0012 t \sqrt{H/A}\right) \tag{33}$$

where A is the indoor area of large space (m^2); H is the ceiling height (m).

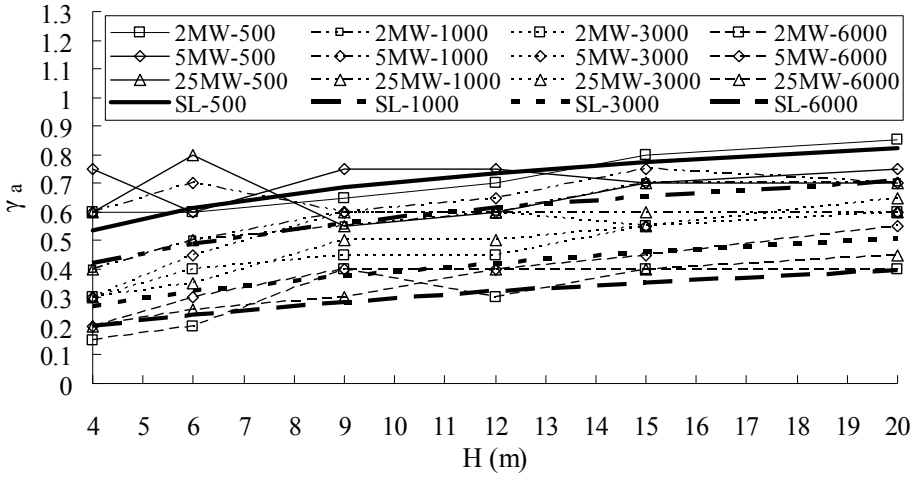

Figure 20. Comparison of the Fitting Curves with Experimental Results of the Coefficient γ_a (SL for the Fitting Curve)

4.2 Prediction of Air Temperature Near the Ceiling of Large Space

Introducing the coefficient of temperature uniformity degree γ_a, and time lag γ_t into Eq. 31, a precise formula for calculating the air temperature near the ceiling of large space can be obtained.

$$T_r - T_a = \gamma_s \gamma_t \left[\gamma_a + (1-\gamma_a) f(r)\right]\left[119.15 \times Q_c^{2/3}\left(0.86H + 0.25Q_c^{2/5}\right)^{-5/3}\right] \tag{34}$$

where the coefficient $\gamma_s, \gamma_t, f(r)$ and γ_a are determined by Eq. 29, 30, 32 and 33 respectively.

4.3 Accuracy of the Formula Proposed and Its Limitations

Li and Du [3] recommended a formula for calculating the air temperature near the ceiling of large space structure in fire as

$$T(x,z,t) - T_g(0) = T_z\left[1 - 0.8\exp(-\beta t) - 0.2\exp(-0.1\beta t)\right]\left[\eta + (1-\eta)\exp\left(-(r-b)/\mu\right)\right] \tag{35}$$

where $T_g(0)$ is the initial indoor temperature; t is burning duration; r is the horizontal distance from the fire source; z is the vertical distance from the fire source; T_z, β, η, b, μ are parameters depending on the fire growth type and the position of the fire source, which can be obtained from She [19].

In order to verify the accuracy of the calculation formula proposed in this paper, according to Eq. (34), and (35), the temperature is calculated respectively for different heat release rates, indoor areas, and ceiling heights. The results of comparative analysis would be discussed in this paper.

4.3.1 Q_c is constant, changing A and H

Changing indoor area A and ceiling height H, while the heat release rate Q_c remains 25MW, according to Eq. 34 and 35, the air temperature distribution can be calculated respectively in Figures 21 (a) ~ (d) (The temperature distribution curves of Figure 22 correspond to different burning durations--5min, 20min, 60min, and 120min).

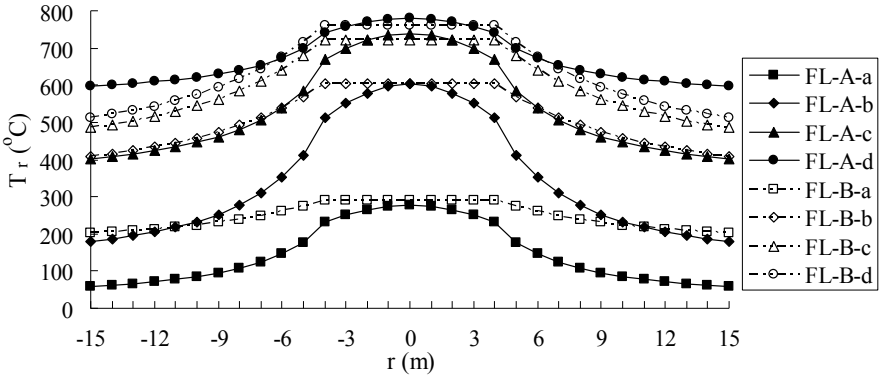

(a) $H = 12\text{m}, A = 500\text{m}^2$

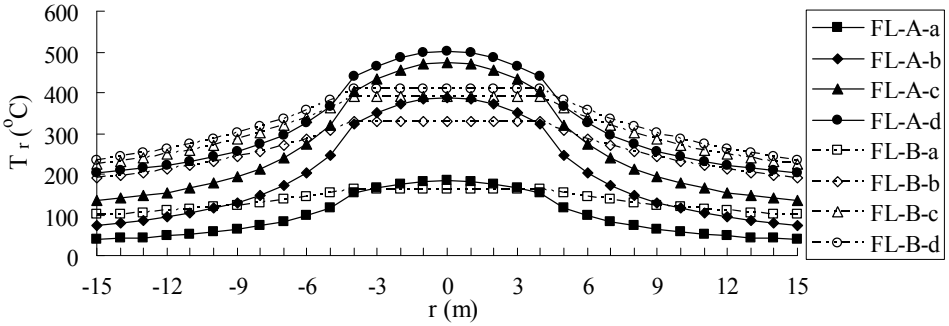

(b) $H = 12\text{m}, A = 6000\text{m}^2$

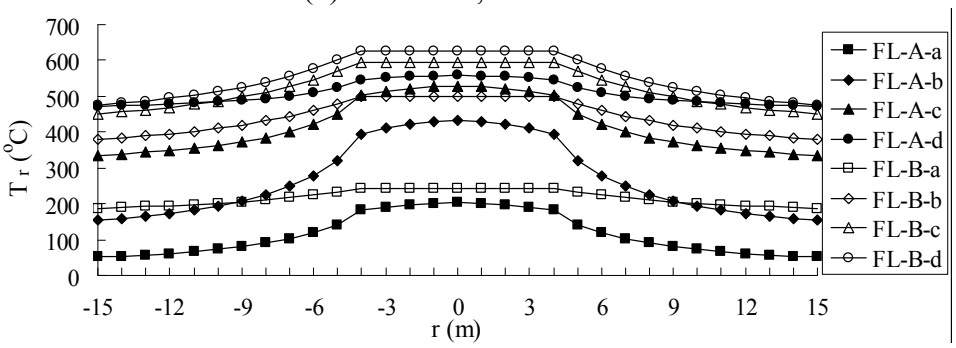

(c) $H = 20\text{m}, A = 500\text{m}^2$

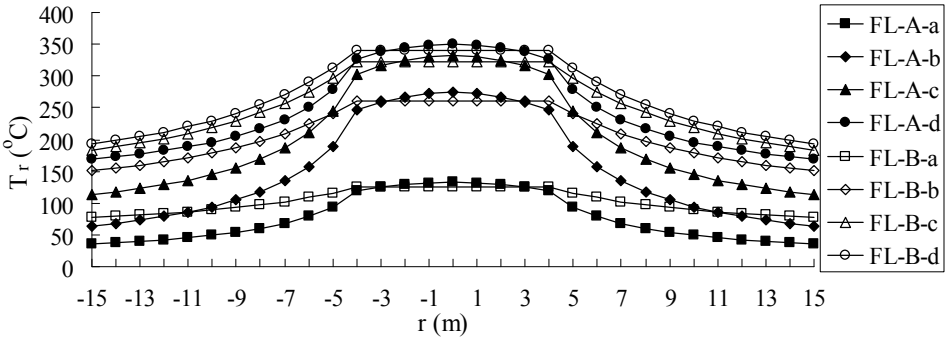

(d) $H = 20\text{m}, A = 6000\text{m}^2$

Figure 21. Air Temperature Distribution near the Ceiling of Large Space ($Q_c = 25\text{MW}$)
(FL-A is from Eq. 34, and FL-B is from Eq. 35, a-5min, b-20min, c-60min, d-120min)

Comparing curves in Figures 21 (a) to (d), the differences between the two temperature distribution curves of Eq. 34 and 35 are as follows.

(1) At the beginning phase, there is a large difference between the two curves (see curves FL-A-a and FL-B-a), however after 120 minutes' burning, the two curves become basically consistent with each other (see curves FL-A-d and FL-B-d).

(2) The air temperature distribution curve above the fire source (in impact area), which can be calculated from Eq. 35, is close to a horizontal line, therefore the temperature is almost the same everywhere (see curves FL-B-a to FL-B-d), and the result disagrees with the actual condition. Furthermore, the larger burning radius is, the greater difference will be. However, the temperature distribution of formula (34) is a curved line, which comparatively obeys the characteristics of the temperature distribution in impact area, and is close to actual condition.
(3) In the temperature distribution curves of formula (35), the horizontal temperature gradient barely changes over time (curves FL-B-a to FL-B-d), which contradicts the phenomenon of time lag in large space fire. However the temperature distribution curves of formula (34) demonstrate a smooth tendency with the increasing of burning time (curves FL-A-a to FL-A-d). Furthermore, as indoor area increases, the effect of time lag becomes even more obvious, as the curve of FL-A-b displays in Figures 21 (a) and (b). Therefore, formula (34) proposed in this paper is more suitable for calculating the air temperature near the ceiling of large space structures in fire, and has a higher accuracy than others.

4.3.2 Q_c *and* H *are constant, changing* A

Changing the indoor area A, while keeping the heat release rate $Q_c = 5\text{MW}$, and the height of ceiling $H = 12\text{m}$ unchanged, the air temperature distribution curves calculated from formula (34) and (35) are displayed in Figures 22 (a) and (b) (The temperature distribution curves of Figure 22 correspond to different burning durations--5min, 20min, 60min, and 120min).

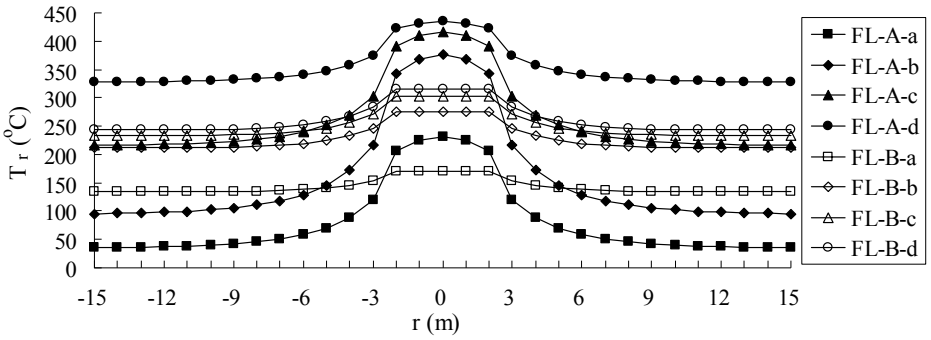

(a) $A = 500\text{m}^2$

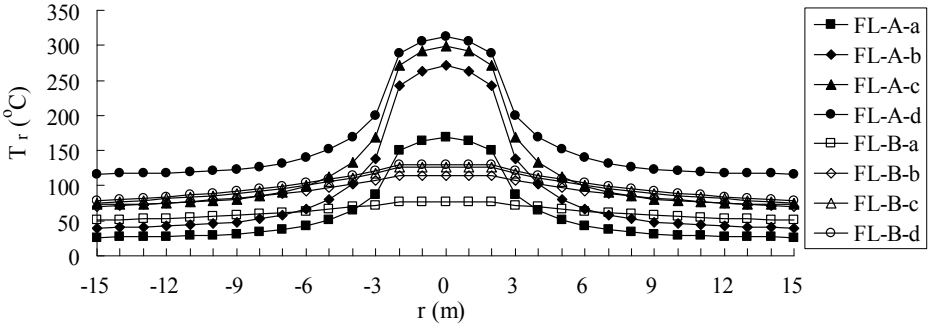

(b) $A = 6000\text{m}^2$

Figure 22. Air Temperature Distribution near the Ceiling of Large Space ($Q_c = 5\text{MW}$, $H = 12\text{m}$)
(FL-A is from Eq. 34, and FL-B from Eq. 35, a-5min, b-20min, c-60min, d-120min)

Comparing the temperature distribution curves in Figures 22 (a) and (b), for small heat release rate ($Q_c = 5\text{MW}$), the air temperature above the fire source of formula (34) is significantly higher than that of formula (35). In this sense, with formula (34) proposed in this paper, the local effect of temperature distribution is more obvious, and the relationship between the indoor area and the effect is positive. The reasons are mainly as follows: (1) the smaller the heat release rate, the

weaker the thrust generated by the smoke plume, which slows down the horizontal diffusion of heat and the mixture of cold and hot air. Therefore the local effect of air temperature is much more obvious; (2) in the derivation process of formula (34), the assumption of energy dissipation is ignored; therefore the result of this formula tends to be conservative.

4.3.3 Relationship between air temperature along the centreline of ceiling and burning time.

According to formula (34) and (35), the relationship between air temperature along the centreline of ceiling and burning time can be obtained for different heat release rates, different indoor areas, and different heights of ceiling, as demonstrated in Figures 23 (a) to (d) (The temperature distribution curves of Figure 23 correspond to different heights of ceiling).

Comparing the curves in Figures 23 (a) to (d), for ceiling height $H < 10\text{m}$, the air temperature along the centreline of ceiling of Eq. 34 is higher than that of Eq. 35. In addition, the smaller the heat release rate, the larger the difference between the two results, as shown in Figures 23 (c) and (d). When the ceiling height H is less than twice the diameter of fire source, it is difficult to form a steady rising smoke plume, and the assumptions in the derivation process of Eq. 34 will be invalid. Therefore, for ceiling height $H < 10\text{m}$, there are significant differences between the results of Eq. (34) and (35). However for ceiling height $H \geq 10\text{m}$, the results of Eq. 34 and 35 are consistent with each other.

In conclusion, in order to calculate air temperature near the ceiling of large space structures in fire with formula (34) accurately, the application scope of the formula should be: height of ceiling $H \geq 10\text{m}$, indoor area $A \geq 500\text{m}^2$, and heat release rate $Q_c \geq 5\text{MW}$.

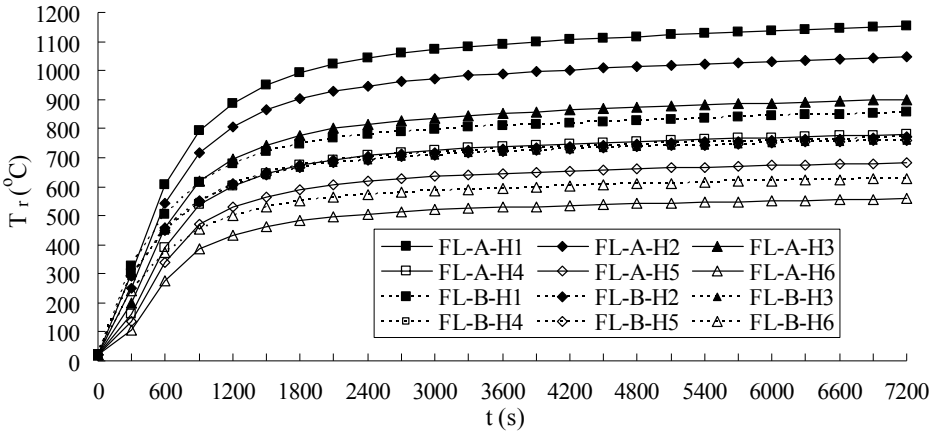

(a) $Q_c = 25\text{MW}, A = 500\text{m}^2$

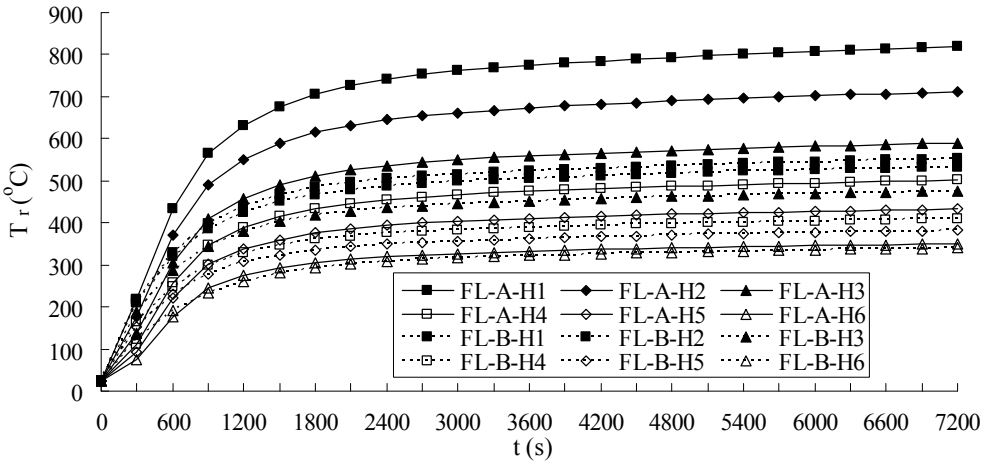

(b) $Q_c = 25\text{MW}, A = 6000\text{m}^2$

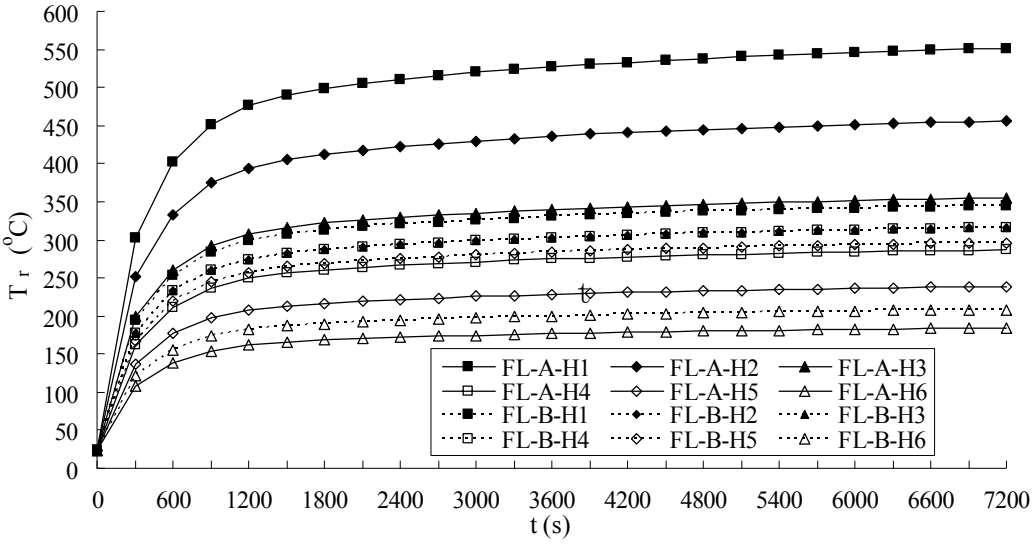

(c) $Q_c = 5\text{MW}, A = 500\text{m}^2$

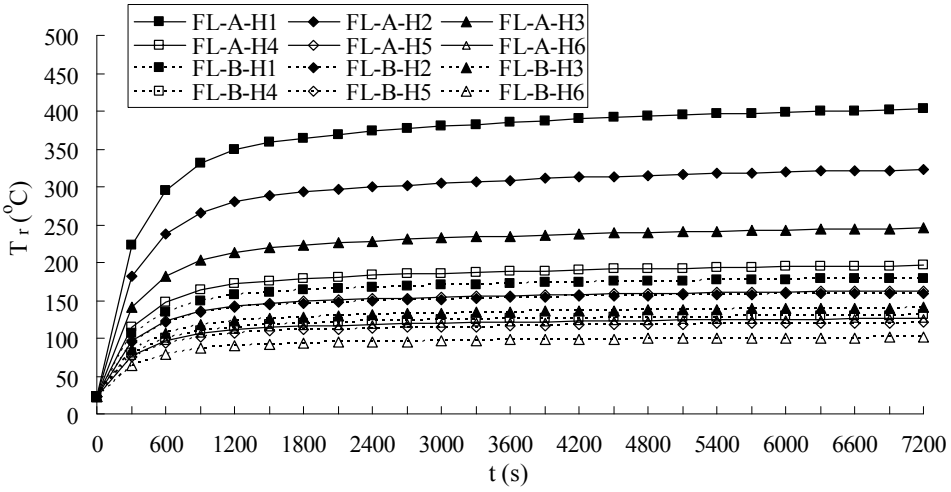

(d) $Q_c = 5\text{MW}, A = 6000\text{m}^2$

Figure 23. Relationship between Air Temperature along Centreline of Ceiling and Burning time

(FL-A from Eq. 34, FL-B from Eq. 35, H1-4m, H2-6m, H3-9m, H4-12m, H5-15m, H6-20m)

5. EXAMPLE

A multi-function hall in a library is an indoor, semi-underground large space structure with a large capacity--28m long, 30m wide, and 10m high with a total floor area of 840 m^2. The plane layout and the function are displayed in Figure 24. Based on performance-based fire protection analysis and design [31], according to structure type, function, and combustible distribution of the multi-function hall, the combustibles can be classified into two major types (for example, curtain and seat), and different fire scenarios also can be defined. The information regarding type, maximum heat release rate, and fire growth rate in different fire scenarios are given in Table 8. The locations of different fire sources are demonstrated in Figure 25.

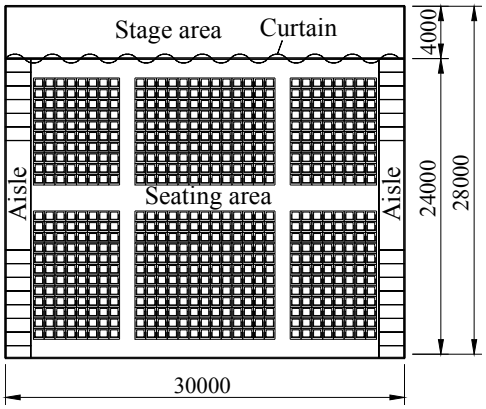

Figure 24. Plane Layout of Multi-function Hall

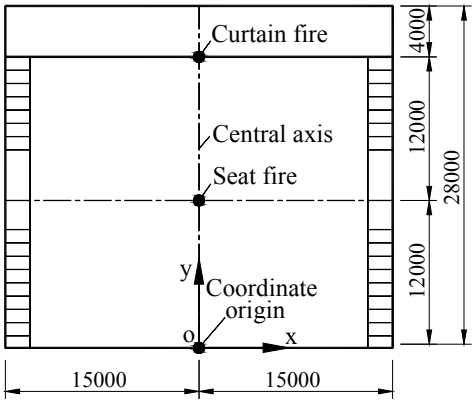

Figure 25. Locations of Fire Sources

With the fire dynamic simulation software CFAST-v4.02 and field simulation software FDS3.0, Ref [31] calculates the ceiling temperature along the centerline (axis y in the Figure 25) at different burning time. Table 9 demonstrates the results for different fire scenarios mentioned.

In the meantime, the air temperatures near the ceiling along the centreline, for fire scenarios FS1~FS4 in Table 8 at different burning time, are calculated with Eq. 34. The results are compared with those in Table 9, as displayed in Figures 26 (a) to (d) (The temperature distribution curves of Figure 26 correspond to different burning time).

Table 8. Information of Different Fire Scenarios

Type	Fire scenarios	Main material	Unit heat release rate	Maximum heat release rate	Fire growth rate
Curtain	FS1	Canvas and fibers. (No fire-retardant treatment)	88~127 kW/m^2	6MW	Fast
	FS2	Canvas and fibers. (fire-retardant treatment)	88~127 kW/m^2	4 MW	Medium
Seat	FS3	Sofa sort	14~18 MJ/kg	16 MW	Fast
	FS4	Wooden chair sort	1.8~7.0 MJ/kg	8 MW	Medium

Table 9. Air Temperature near the Ceiling along the Axis y for Different Fire Scenarios (^{o}C)

Fire scenarios	Burning time	Horizontal distance on y axis (m)														
		0	2	4	6	8	10	12	14	16	18	20	22	24	26	28
FS1	60s	23.6	23.8	24.0	24.4	24.8	25.0	25.6	26.0	26.8	28.2	30.0	32.8	34.8	32.8	30.0
	180s	25.0	25.3	25.6	26.0	26.4	27.0	27.6	30.8	34.4	38.6	49.8	62.0	69.0	62.0	49.8
	300s	45.0	45.2	45.5	45.8	46.2	46.7	48.2	48.9	52.2	66.6	108	160.	195	160	108
	600s	52.0	52.5	53.0	53.8	55.0	56.0	58.0	61.2	68.2	96.2	142	256	345	256	142
FS2	60s	23.6	23.7	23.8	23.9	24.0	24.2	24.4	24.6	24.8	25.0	25.4	26.6	28.4	26.6	25.4
	180s	25.0	26.5	28.2	30.1	32.4	34.2	36.2	38.6	40.2	42.4	45.2	46.9	49.5	46.9	45.2
	300s	29.6	31.2	33.6	35.8	37.7	40.6	44.2	48.2	52.5	62.4	76.3	92.0	116	92.0	76.3
	600s	45.0	46.0	47.2	48.6	50.0	53.2	55.8	59.2	62.8	82.6	123	232	272	232	123
FS3	60s	24.1	24.8	26.5	28.2	30.5	33.2	35.0	33.2	30.5	28.2	26.5	24.8	24.1	23.8	23.5
	180s	38.2	42.7	49.2	56.8	62.5	70.4	78.0	70.4	62.5	56.8	49.2	42.7	38.2	36.9	35.0
	300s	68.2	72.2	89.4	110	132	154	165	154	132	110	89.4	72.6	68.2	57.3	48.0
	600s	92.5	105	136	221	306	436	460	436	306	221	136	105	92.5	76.8	65.1
FS4	60s	23.8	24.6	25.4	26.0	27.2	28.4	29.0	28.4	27.2	26.0	25.4	24.6	23.8	23.1	22.5
	180s	32.4	33.5	36.2	38.6	44.2	50.3	56.0	50.3	44.2	38.6	36.2	33.5	32.4	31.8	31.2
	300s	46.0	48.3	52.8	64.3	78.2	92.8	100	92.8	78.2	64.3	52.8	48.3	46.0	44.8	43.4
	600s	56.0	65.8	72.6	95.1	140	240	265	240	140	95	72.6	65.8	56.0	52.3	47.5

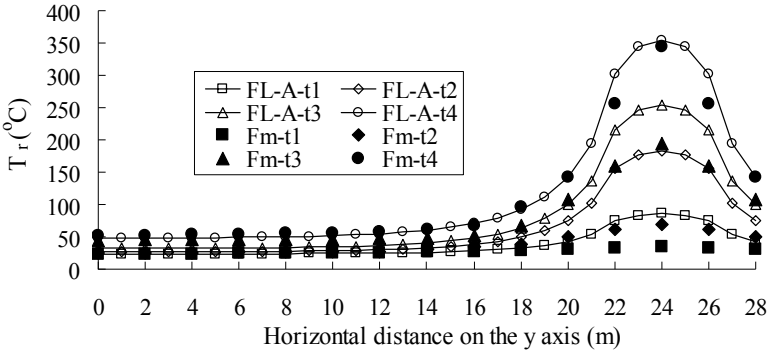

(a) Fire scenario FS1

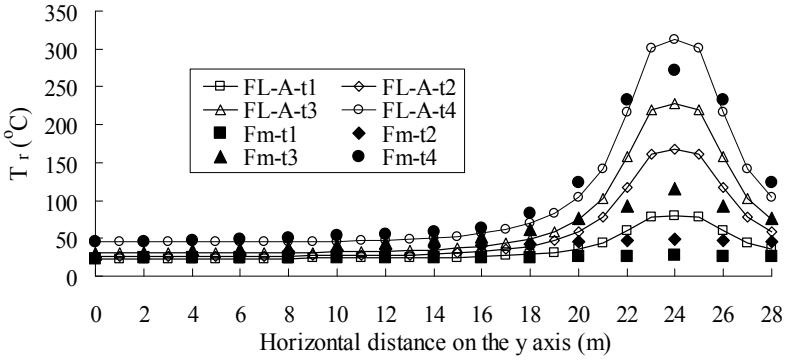

(b) Fire scenario FS2

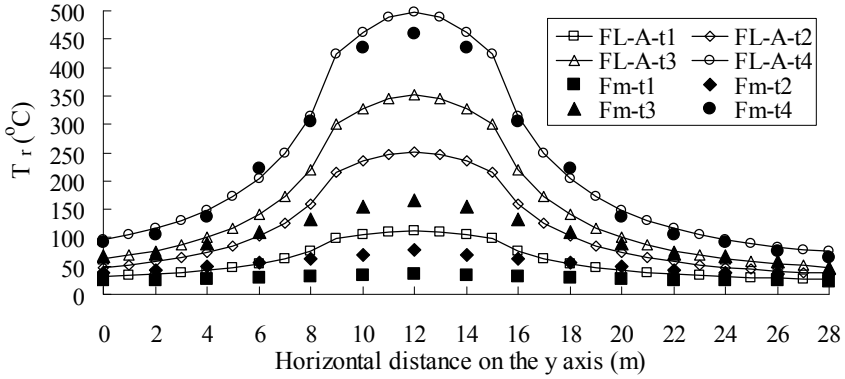

(c) Fire scenario FS3

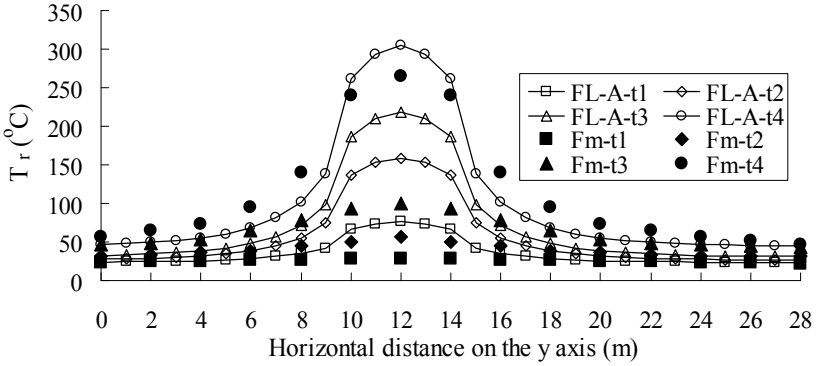

(d)Fire scenario FS4

Figure 26. Comparison of Air Temperature Distributions near the Ceiling along Centreline at Different Fire Scenarios
(FL-A from Eq. 34, Fm is the Values of Table 9, t1-60s, t2-180s, t3-300s, t4-600s)

As shown in Figures 26 (a) to (d), during the early stage of burning (about the first 300s of burning time), the air temperatures calculated with Eq. 34 are generally higher than those in Table 9. In Figure 26 (a), for example, for burning time 180s, 300s, and 600s, the corresponding temperatures calculated with formula (34) are respectively 183^{o}C, 253^{o}C, and 3545^{o}C. Compared with the simulation temperatures in of 69 ^{o}C, 195 ^{o}C, and 345^{o}C as in Table 9, the former are higher by 166%, 30%, and 2.8% respectively. It can be seen that, due to large temperature difference between hot and cold air, the heat dissipation of the smoke plume is significant in the early stage of burning, which is ignored in the derivation of Eq. 34. Therefore there are some differences between the analytical and numerical results. However, if the heat dissipation recedes with burning continuing, the temperatures calculated by Eq. 34 may tend to be close to the simulation ones in Table 9.

6. CONCLUSION

Based on the field model of fire thermodynamics and heat transfer, the temperature field model of large space fire is established, which considers fire source, smoke plume, and smoke layer model. Parametric studies of the large space fire were carried out and the results showed that the duration of burning is less than 80 minutes when the total amount of combustibles is not more than 2000kg. However, if the heat release rate Q_c is less than 5MW, the burning time of fire can be more than 120 minutes. It is thus recommended that the burning duration may be taken as 120 minutes conservatively in the fire analysis of large-space steel structures.

An analytical expression (Equation 34) has been derived which can be used to predict the air temperature of large space fire that meets the criteria of (1) ceiling height greater than 10m, (2) indoor area more than 500 m^2 and (3) heat release rate greater than 5MW. The accuracy of the proposed equation was verified by comparing the results with those obtained by fire dynamic simulation software.

ACKNOWLEDGEMENTS

The research was supported by a project funded by the Priority Academic Program Development of Jiangsu Higher Education Institutions, Jiangsu Provincial Forward-Looking Cooperation Foundation of Industry, Education and Research (No. BY2012200 and No. BY2009151), and National Natural Science Foundation of China (No. 51378105 and No. 51008065). The authors are grateful to the financial support.

REFERENCES

[1] Fan, Z., Wang, Z. and Tang, J., “Analysis on Temperature Field and Determination of Temperature upon Healing of Large-span Steel Structure of the National Stadium”, Jianzhu Jiegou Xuebao, 2007, Vol. 28, No. 2, pp. 32-40.

[2] Yu, F.B., Wang, X.T., Zhou, M. and Wang, W.Z., “Research on Fire Resistance Performance of Pre-stressed Suspended Steel Reticulated Shell”, Advanced Materials Research, 2011, Vol. 163, No. 1, pp. 790-794.

[3] Li, G.Q. and Du, Y., “Utility Temperature Elevation Empirical Formula in Large Space Fire”, Fire Science and Technology, 2005, Vol. 24, No. 5, pp. 283-287.

[4] Xue, H., Ho, J.C., Cheng, Y.M., “Comparison of Different Combustion Models in Enclosure Fire Simulation”, Fire Safety Journal, 2001, Vol. 36, No. 1, pp. 37-54.

[5] Cooper, L.Y., “Smoke Movement in Rooms of Fire Involvement and Adjacent Spaces”, Fire

Safety Journal, 1981, Vol. 3, pp. 201-214.
[6] Venkatasubbaiah, K. and Jaluria, Y., "Numerical Simulation of Enclosure Fires with Horizontal Vents", Numerical Heat Transfer, 2012, Vol. 62, pp.179-196.
[7] Floyd, J.C., McGrattan, K.B., Hostikka, S. and Baum, H.R., "CFD Fire Simulation Using Mixture Fraction Combustion and Finite Volume Radiative Heat Transfer", Journal of Fire Protection Engineering, 2003, Vol. 13, No. 4, pp. 275.
[8] Chow, W.K. and Yin, R., "Discussion on two plume formulae with computational fluid dynamics", Journal of Fire Sciences, 2002, Vol. 20, No. 3, pp. 179-201.
[9] Li, G.Q. and Du, Y., "Analyses the Parameters of Fire Temperature Elevation at the top of Large Space Buildings", Fire Science and Technology, 2005; Vol. 24, No. 1, pp.19-22.
[10] Huang, L.Y. and Wen, J.X., "Field Modelling of Large Scale Compartment Jet Fires by Constrained Equilibrium Method", Fire Safety Science - Proceedings of the 6th International Symposium, 2000, Vol. 1, pp. 361-372.
[11] Shi, C.L., Zhong, M.H., Fu, T.R. and He, L., "An Investigation on Spill Plume Temperature of Large Space Building Fires", Journal of Loss Prevention in the Process Industries, 2009, Vol. 22, No. 4, pp. 76-85.
[12] Cooper, L.Y. and Stroup, D.W., "Thermal Response of Unconfined Ceilings above Growing Fires and the Importance of Convective Heat Transfer", Journal of Heat Transfer, 1987, Vol. 109, No. 1, pp. 172-178.
[13] Cooper, L.Y., "Heat Transfer in Compartment Fires near Regions of Ceiling Jet-wall Impingement", American Society of Mechanical Engineers, Heat Transfer Division, 1987, Vol. 73, pp. 57-62.
[14] Harmathy, T.Z., "Fire Safe Design and Concrete", Longman Scientific & Technical, London, 1993, Vol. 1, pp. 210-211.
[15] Anon., "Design Guide: Structural Fire Safety-workshop (CIB W14)", Fire Safety Journal, 1986, Vol. 10, No. 2, pp. 75-137.
[16] Vrouwenvelder, T., "JCSS Probabilistic Model Code", Structural Safety, 1997, Vol.19, No.3, pp. 245-251.
[17] Sunil, K. and Kameswara, R.C., "Fire Loads in Office Building", Journal of Structural Engineering, 1997, Vol. 123, No. 3, pp. 365-368.
[18] Harmathy, T.Z. and Mehaffey, J.R., "Design of Buildings for Prescribed Levels of Structural Fire Safety", ASTM Special Technical Publication, 1985, Vol. 1, pp. 160-175.
[19] She, G.J., "The Fire Emulation and Resistance of Long-span Spatial Steel Structure Based on Performance", Master dissertation, Southeast University, Nanjing, 2007.
[20] European Committee for Standardization (CEN), "Eurocode 1-Actions on Structures, Part 1-2: General Actions-Actions on Structures Exposed to Fire", CEN, Brussels, 2003.
[21] Chow, W.K., Yi, L. and Shi, C.L., "Experimental Studies on Mechanical Smoke Exhaust System in an Atrium", Journal of Fire Sciences, 2005, Vol. 23, No. 5, pp. 429-444.
[22] William, D. D., "Comparison of Algorithms to Calculate Plume Centerline Temperature and Ceiling Jet Temperature with Experiments", Journal of Fire Protection Engineering, 2002, Vol.12, pp.9-29.
[23] Motevalli, V., "Numerical Prediction of Ceiling Jet Temperature Profiles during Ceiling Heating Using Empirical Velocity Profiles and Turbulent Continuity and Energy Equations", Fire Safety Journal, 1994, Vol. 22, No. 2, pp. 125-144.
[24] Zukoski, E.E., Kubota, T. and Cetegen, B., "Entrainment in Fire Plumes", Fire Safety Journal, 1980, Vol. 3, No.3, pp. 107-121.
[25] Gershuni, G.Y., Zhukhovitskiy, Y.M. and Yurkov, Y.S., "Vibrational Thermal Convection in a Horizontal Layer with Internal Heat Sources", Heat Transfer - Soviet Research, 1991, Vol. 23, No. 4, pp. 959-967.
[26] Guan, D., "Calculation of Unsteady Aerodynamic", Beijing Aeronautics and Astronautics Press, 1991.

[27] Fang, J., Shu, X.M., Yuang, H.Y. and Zhen, X., "Self-preserving Size Distribution of Fire Soot Fractal Coagulation in Flaming Combustion", Journal of Fire Sciences, 2004, Vol. 22, No. 1, pp. 53-68.
[28] Beltaos, S. and Rajaratnam, N., "Impinging Circular Turbulent Jets", ASCE J Hydraulics Div, 1974, Vol. 100, No. 10, pp. 1313-1328.
[29] Bai, Y., Shi, Y.J. and Wang, Y.Q., "Numerical Simulation Analysis on Temperature Field for Large-Space Structures under Fire", China Safety Science Journal, 2006, Vol. 16, No. 1, pp. 34-38.
[30] Jin, X.H., Huo, R. and Li, Y.Z., "Study on Dynamic Display of Smoke Movement in Atrium Fire", China Safety Science Journal, 1999, Vol. 4, No. 9, pp. 26-10.
[31] Research Report, "Fire Safety Evaluation Report of New Library Multi-Function Room of Nanjing", State Key Laboratory of Fire Science of University of Science and Technology of China, 2003.

SIMPLIFIED DESIGN MODEL FOR UNI-AXIALLY LOADED DOUBLE-SKINNED CONCRETE-FILLED-STEEL-TUBULAR COLUMNS WITH EXTERNAL CONFINEMENT

J.C.M. Ho[1] and C.X. Dong[2]

[1] *Senior Lecturer, School of Civil Engineering, The University of Queensland, Brisbane, QLD 4072, Australia
[2]PhD Student, Department of Civil Engineering, The University of Hong Kong, Hong Kong
*(Corresponding author: E-mail: johnny.ho@uq.edu.au)

Received: 5 December 2012; Revised: 4 January 2013; Accepted: 16 December 2013

ABSTRACT: One of the significant contributions of using double-skinned concrete-filled-steel-tubular (CFST) columns is that it can extend the maximum limit of concrete strength that can be practically used in the construction industry, by improving the ductility of columns through providing more uniform and continuous confining pressure to the in-filled concrete. However, because of the imperfect interface bonding occurs at early stage, the elastic strength and stiffness will decrease so that the confinement effect provided by the steel tube is not fully utilized. To improve the situation, the authors have proposed to use external confinement in the form of steel rings on the outer steel tube to restrict the dilation of CFST columns and thus restore an intact interface bonding condition. It has been verified by uni-axial compression test that the elastic strength, stiffness and interface bonding were improved. Based on the test results, the authors have developed a theoretical model for predicting the uni-axial load-carrying capacity of doubled-skinned CFST columns. As a continued study, the authors will investigate the most critical parameters affecting the uni-axial strength, and to develop a simplified formula for practical design of doubled-skinned CFST columns through an extensive parametric study.

Keywords: Columns, Concrete-filled, Double-skin tubular, External confinement, Rings

1. INTRODUCTION

High-strength concrete (HSC) of concrete strength about 100 MPa has been adopted popularly in East Asia for construction of tall buildings. Not only does the HSC improve the strength-to-weight ratio, reduce embodied energy, but also save extra floor space. Recently due to the rapid development of superfine materials such as micro-silica and superfine cement, as well as the matured filler technology [1,2], the concrete compressive strength can now be pushed up to 130 MPa. Using such a very high-strength concrete can also improve the lateral stiffness of tall buildings and limit the overall and inter-storey drift ratio to within the serviceability limit state. Therefore, it is indeed very attractive to the column construction of tall buildings. However, notwithstanding these merits, the adoption of such a high concrete strength is still rare in the construction industry. The use of lower concrete strength for column construction of tall buildings is under-utilising the construction materials and wasting available floor space that can possibly be saved.

One of the major reasons that inhibits the use of HSC is its brittleness [3-7], which needs to have substantial confinement to protect the concrete core from explosive failure. The traditional method of utilizing transverse steel in the form of closed hoops or ties for normal-strength reinforced concrete (RC) columns is not applicable in HSC columns, because the transverse reinforcement required for providing sufficient confinement against explosive failure will be too large to enable good placing quality of concrete. In order to have a breakthrough in the maximum limit that can be practically used in column construction, special type of confinement that can provide larger, more continuous and uniform confining pressure to concrete should be devised. One of the most ineffective reasons for adopting transverse reinforcement in RC columns is the

concrete arching action, which decreases the effectively confined concrete area. In order to eliminate this action, a continuous concrete confinement in the form of steel tube has been advocated. Two composite structural forms of high-strength concrete-filled-steel-tubular (HSCFST) column that contains one (i.e. single-skinned) or two hollow steel tubes (i.e. double-skinned) for concrete confinement were put forward.

From structural point of view, these forms of composite column construction can provide larger axial strength [8-20], bending stiffness, moment capacity [10,21-24], better ductility [25,26,27] and excellent seismic performance [28-34]. The tubes are both longitudinal reinforcement and formwork, which saves the construction cycle time and cost. Due to composite action, the sizes of double-skinned CFST column can be up to 50% smaller than that of HSC columns with the same load-carrying capacity. The larger strength-to-weight ratio decreases the embodied energy level in the building structures. Furthermore, higher strength concrete is more durable than normal-strength concrete (NSC), therefore, it lengthens the design life of the buildings and reduces the construction and demolition waste generated. The double-skinned CFST columns are more structural efficient than another type of single-skinned CFST columns (one tube with in-filled concrete). It improves the strength-to-weight ratio by replacing the bulky central concrete with a lighter inner steel tube. It also provides a dry atmosphere within the inner steel tube, which is particularly useful to house sub-sea oil production facilities for offshore structures [32,35,36].

The steel tubes in the double-skinned CFST columns provide superior confining pressure to the in-filled concrete to enhance its strength and stiffness. However, the confinement performance during the initial elastic stage has not been fully developed due to the imperfect steel-concrete interface bonding [9,37] since steel dilates more than concrete under compression [38-41]. In order to maximize the confining performance of steel tubes in the early elastic stage, the authors have previously proposed to use external confinement in the form of steel rings to restrict the dilation of HSCFST columns for restoring an intact interface bonding [42,43,44]. The proposed method has been verified by a preliminary test programme on uni-axial compression performance of unconfined and ring-confined double-skinned CFST columns. It has been shown from the results that the rings provided effective lateral restraint points, and between the rings, the lateral dilation of columns is smaller than that of unconfined columns. Overall speaking, the Poisson's ratios of columns between ring levels were close to 0.2, except for the locations further away from the rings, which were about 0.3. It verified that the interface bonding have been substantially improved under the extra confinement effect provided by the steel rings. Previously, efforts have been spent on installing internal stiffeners and binding bars for achieving similar purpose [45-48]. However, it is worth noting that the welding of these internal stiffeners and binding bars are more difficult than that of the proposed external confinement, in particular for double-skinned HSCFST columns where the gap between steel skins is very limited.

Based on the test results, the authors have developed a theoretical model based on force equilibrium equations for evaluating the uni-axial load-carrying capacity of both unconfined and ring-confined double-skinned CFST columns. Nevertheless, the evaluation procedure was divided in to several steps and depends on hoop stress that is not readily available at early design stage. Therefore, an iterative process may be required to get the final load-carrying capacity of a design section. In order to simplify the evaluation process and to make the model more user friendly particularly at the design stage, the authors will in the paper investigate the major factors that affect the load-carrying capacity of ring-confined double-skinned HSCFST column through a parametric study. Based on the obtained results, a simplified equation relating the load-carrying capacity and solely geometry and material factors will be proposed. It is believed that the simplified equation can serve as a design aids for practical design of ring-confined double-skinned CFST columns.

2. DETAILS OF SPECIMENS

To verify the effectiveness of the proposed external ring confinement on the improvement of interface bonding, strength and stiffness of double-skinned CFST columns, the authors has previously conducted a series of uni-axial compression test on 20 double-skinned CFST columns. The specimens were divided into four groups based on the provision of confinement, concrete cylinder strength and the hollow ratio χ (defined as $\chi = \frac{D_i}{D_o - 2t_o}$), where D_i and D_o are the diameters of the inner and outer tubes respectively, t_o is the thickness of the outer tube: (1) Four double-skinned CFST columns of hollow ratio 0.56 and external steel rings of various spacing ($5t_o$, $10t_o$, $15t_o$ and $20t_o$); (2) Four double-skinned CFST columns of hollow ratio 0.72 and external steel rings of various spacing ($5t_o$, $10t_o$, $15t_o$ and $20t_o$); (3) One double-skinned CFST column of hollow ratio 0.56 but without external steel rings; (4) One double-skinned CFST column of hollow ratio of 0.72 but without external steel rings. In each of the two sets of specimens (i.e. χ = 0.56 and 0.72), concrete cylinder strength of 50 and 85 MPa were adopted. The grade of both inner and outer steel tubes is S355 produced as per BS EN 10210-2:2006. For all tested specimens, the thickness of both inner and outer steel tubes is 5 mm and the diameter of outer steel tube is 168.3 mm (measured to the outer face). For columns of hollow ratios 0.56 and 0.72, the diameters of inner tubes are 88.9 and 114.3 mm respectively (measured to the outer face). The total height of the specimens is 330 mm (aspect ratio of 2). Figure 1(a) shows the double-skinned normal-strength concrete-filled-steel-tubular (NSCFST) columns with hollow ratio of 0.56 and with external steel rings of various spacing ($5t_o$, $10t_o$, $15t_o$ and $20t_o$). Figure 1(b) shows the double-skinned NSCFST columns with hollow ratio of 0.72 and with external steel rings of various spacing ($5t_o$, $10t_o$, $15t_o$ and $20t_o$). Figure 1(c) shows the double-skinned NSCFST columns with hollow ratio of 0.56 and without external steel rings. Figure 1(d) shows the double-skinned NSCFST columns with hollow ratio of 0.72 and without external steel rings. Figure 1(e) shows the double-skinned HSCFST columns with hollow ratio of 0.56 and with external steel rings of various spacing ($5t_o$, $10t_o$, $15t_o$ and $20t_o$). Figure 1(f) shows the double-skinned HSCFST with hollow ratio of 0.72 and with external steel rings of various spacing ($5t_o$, $10t_o$, $15t_o$ and $20t_o$). Figure 1(g) shows the double-skinned HSCFST columns with hollow ratio of 0.56 and without external steel rings. Figure 1(h) shows the double-skinned HSCFST columns with hollow ratio of 0.72 and without external steel rings. The section and material properties of the specimens are summarised in Table 1.

Figure 1(a) Double-skinned NSCFST columns with external steel rings (s=$5t_o$, $10t_o$, $15t_o$ and $20t_o$) with Hollow Ratio of 0.56

Figure 1(b) Double-skinned NSCFST columns with external steel rings (s=5t_o, 10t_o, 15t_o and 20t_o) with Hollow Ratio of 0.72

Figure 1(c) Double-skinned NSCFST columns without external steel ring with hollow ratio of 0.56

Figure 1(d) Double-skinned NSCFST columns without external steel ring with hollow ratio of 0.72

Figure 1(e) Double-skinned HSCFST columns with external steel rings (s=5t_o, 10t_o, 15t_o and 20t_o) with hollow ratio of 0.56

Figure 1(f) Double-skinned HSCFST columns with external steel rings (s=5t_o, 10t_o, 15t_o and 20t_o) with hollow ratio of 0.72

Figure 1(g) Double-skinned HSCFST columns without external steel ring with hollow ratio of 0.56

Figure 1(h) Double-skinned HSCFST columns without external steel ring with hollow ratio of 0.72

Table 1. Details of specimens and materials' properties

Specimen Label	D_i (mm)	t_i (mm)	$f_{y,i}$ (MPa)	D_o (mm)	t_o (mm)	$f_{y,o}$ (MPa)	f'_c (MPa)	$f_{y,R}$ (MPa)
D-0.56-50-5	88.9	5	450	168.3	5	360	50	300
D-0.56-50-10	88.9	5	450	168.3	5	360	50	300
D-0.56-50-15	88.9	5	450	168.3	5	360	50	300
D-0.56-50-20	88.9	5	450	168.3	5	360	50	300
D-0.56-50-0	88.9	5	450	168.3	5	360	50	N/A
D-0.56-85-5	88.9	5	450	168.3	5	360	85	300
D-0.56-85-10	88.9	5	450	168.3	5	360	85	300
D-0.56-85-15	88.9	5	450	168.3	5	360	85	300
D-0.56-85-20	88.9	5	450	168.3	5	360	85	300
D-0.56-85-0	88.9	5	450	168.3	5	360	85	N/A
D-0.72-50-5	114.3	5	430	168.3	5	360	50	300
D-0.72-50-10	114.3	5	430	168.3	5	360	50	300
D-0.72-50-15	114.3	5	430	168.3	5	360	50	300
D-0.72-50-20	114.3	5	430	168.3	5	360	50	300
D-0.72-50-0	114.3	5	430	168.3	5	360	50	N/A
D-0.72-85-5	114.3	5	430	168.3	5	360	85	300
D-0.72-85-10	114.3	5	430	168.3	5	360	85	300
D-0.72-85-15	114.3	5	430	168.3	5	360	85	300
D-0.72-85-20	114.3	5	430	168.3	5	360	85	300
D-0.72-85-0	114.3	5	430	168.3	5	360	85	N/A

In all specimens, the external steel rings were mild steel round bars of 8 mm diameter and the yield strength is f_R = 300 MPa. The rings were welded to the outer tubes at different spacing and the lap length was ten times the diameter of the steel bar (80 mm). Each ring was welded to the outer tube at eight locations with a central angle of 45° separated from each other. Figures 2 and 3 show the test setup and the details of the specimens.

A naming system consisting of one letter and three numbers has been used to represent the specimens. For instance, 'D-0.72-50-5' represents a double-skinned CFST column (indicated by the first letter "D"), a hollow ratio of 0.72 (indicated by the first number "0.72"), a concrete cylinder strength of about 50 MPa on the testing day (indicated by the second number "50") and lastly five times the thickness of the outer steel tube as the ring spacing (indicated by the last number "5"). Alternatively, 'D-0.56-85-0' represents a double-skinned CFST column (indicated by the first letter "D") with a hollow ratio of 0.56 (indicated by the first number "0.56"), a concrete cylinder strength of about 85 MPa on the testing day (indicated by the second number "85"), and lastly no external steel ring (i.e. zero spacing indicated by the last number "0").

Figure 2 Test setup

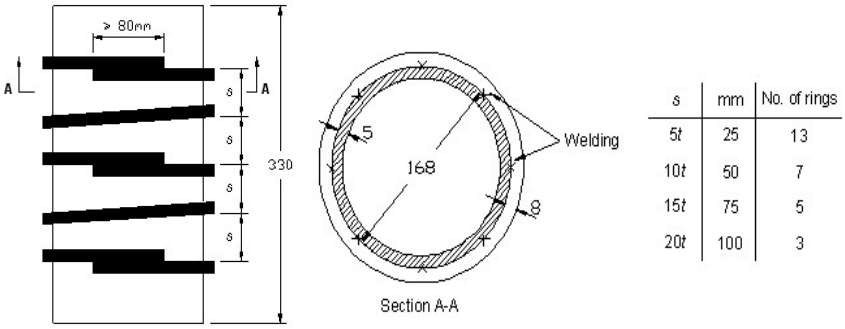

s	mm	No. of rings
5t	25	13
10t	50	7
15t	75	5
20t	100	3

Figure 3 Details of external steel rings of specimens

3. SIMPLIFIED DESIGN MODEL FOR CONFINED DOUBLE-SKINNED CFST COLUMNS

3.1 Theoretical Equations for Confined Double-skinned CFST Columns

There were a lot of researches conducted on the theoretical models of double-skinned HSCFST columns [49-52]. However, all of these models were developed based on unconfined double-skinned CFST columns. Furthermore, the design guidelines specified in Eurocode 4 [53] were also only applicable to unconfined CFST columns. If those models and guidelines are used for design of confined double-skinned CFST columns, the uni-axial load-carrying capacity will be significantly underestimated. To this, the authors have previously developed a theoretical model based on force equilibrium method to predict the uni-axial load carrying capacity of ring-confined double-skinned CFST columns. The validity of the theoretical model has been verified by comparing the theoretical results with the experimental results obtained previously by the authors and other researchers [9,13,22,51,54]. Good agreement was obtained.

The following briefly summarises the theoretical formulas for evaluating the axial capacity of the double-skinned CFST columns:

$$N_p = f_i A_i + f_o A_o + f_{cc} A_{cc} \quad (1)$$

where N_p in Eq. 1 represents the predicted axial load capacity of double-skinned CFST column with/without external confinement. In Eq. 1, f_i and f_o are the axial stresses in the inner and outer tubes respectively under bi-axial stress state; f_{cc} is the axial stress in the core concrete under the confining pressure f_r. These parameters are given by the following equations:

$$f_o^2 - f_o \sigma_{\theta,o} + {\sigma_{\theta,o}}^2 = {f_{y,o}}^2 \quad (2a)$$

$$f_i^2 - f_i \sigma_{\theta,i} + {\sigma_{\theta,i}}^2 = {f_{y,i}}^2 \quad (2b)$$

$$f_{cc} = f_c' + 4.1 f_r \quad (2c)$$

where $f_{y,o}$, $f_{y,i}$ are the uni-axial yield strength of the steel tubes, f_r is the confining pressure and f_{cc} is the confined concrete strength [55]. The hoop stress $\sigma_{\theta,o}$ of the outer tube at ultimate strength is taken as the formulas proposed by Hatzigeorgiou [56] in Eq. 3:

$$\sigma_{\theta,o} = \alpha_\theta f_{y,o} \quad (3a)$$

$$\alpha_\theta = \exp(\ln(\frac{D_0}{t_0}) + \ln(f_{y,o}) - 11) \le 1 \quad (3b)$$

The confining pressure f_r for ring-confined and unconfined specimens is shown in Eq. 4a and 4b respectively.

$$f_r = -\frac{2t_o h \sigma_{\theta,o} - 2nA_R \sigma_R}{(D_o - 2t_o)h} \quad (4a)$$

$$f_r = -\frac{2t_o \sigma_{\theta,o}}{(D_o - 2t_o)} \quad (4b)$$

where $\sigma_{\theta,o}$ is the hoop tensile stress developed in the outer tube; σ_R is the tensile stress acting in the external rings; A_R is the cross-section area of each steel ring; D_o and t_o represent the diameter and thickness of the outer steel tube; h stands for the total height of the column; n is the number of the external steel rings welded on the specimen.

3.2 Simplified Formulas for Confined Double-skinned CFST Columns

One of the difficulties of applying the above equation in design stage is that the whole calculation process is split into different parts and complicated equations such as those for the hoop stress and the Von Mises Criterion have to be gone through each time. For the sake of design purpose, it is better to have an equation depending on solely the geometry and material factors that are readily available in early design stage. Hence, based on the theoretical equations presented above, a parametric study on the effects of various geometry and material factors on the uni-axial load-carrying capacity of double-skinned CFST columns will be conducted herein. The cross-sections adopted are circular double-skinned CFST columns of outer diameter 1 m. In the parametric study, the following parameters have been varied:

(1) The concrete cylinder strength (f_c') was varied from 20 to 80 MPa to cover typical double-skinned CFST columns cast with normal- and high-strength concrete.

(2) The hollow ratio (χ) was varied from 0.3 to 0.7 in this study to cover typical double-skinned CFST column that can be constructed practically.
(3) The diameter-to-thickness ratios of outer (D_o/t_o) and inner (D_i/t_i) steel tubes were varied from 40 to 100.
(4) The yield strength of inner ($f_{y,i}$) and outer steel tube ($f_{y,o}$) was taken as 275, 355 or 460 MPa. The same yield strength was adopted for the outer and inner tubes because it is usually the practice in real design and construction.
(5) The volumetric ratio of external rings to concrete (ρ_R), which is defined as the ratio between the volumes of external rings to the in-filled concrete, was varied from 0 (i.e. unconfined) to 10%.
(6) Mild steel is adopted as the external rings, the yield strength of which is taken as 235 or 275 MPa.

3.2.1 Confining pressure provided by outer tube ($f_{r,tube}$)

From the previously proposed theoretical model, it is evident that the confining pressure (f_r) provided by the steel tube and the external rings to the concrete is the most crucial parameter to predict the uni-axial load-carrying capacity. In this study, it is proposed to investigate the relationship of f_r with other parameters based on the obtained results. The investigation is separated into two parts: (1) Confining pressure provided by the steel tube ($f_{r,tube}$); (2) Confining pressure provided by the rings ($f_{r,ring}$). Firstly, the confining pressure provided by the outer steel tube was plotted against the diameter-to-thickness ratio D_o/t_o for different yield strength of the outer tube as shown in Figure 4. The y-axis represents $f_{r,tube}$ given by Eqs. (3) and (4b). The x-axis represents the diameter-to-thickness ratios of the outer steel tubes. From the figure, it is found that $f_{r,tube}$ is insensitive to the diameter-to-thickness ratio D_o/t_o for a particular yield strength. Therefore, in this study, it is proposed to use a constant value for $f_{r,tube}$, which is taken as the lower bound value obtained in the parametric study for each of the yield strength. For the sake of practical design purpose, the adopted lower bound values of $f_{r,tube}$ have been plotted against the yield strength of the outer steel tube $f_{y,o}$ in Figure 5. From the figure, it is found that these two parameters can be correlated very well using linear equation, which is written in Eq. (5):

$$f_{r,tube} = 0.025 f_{y,o} - 4.5 \tag{5}$$

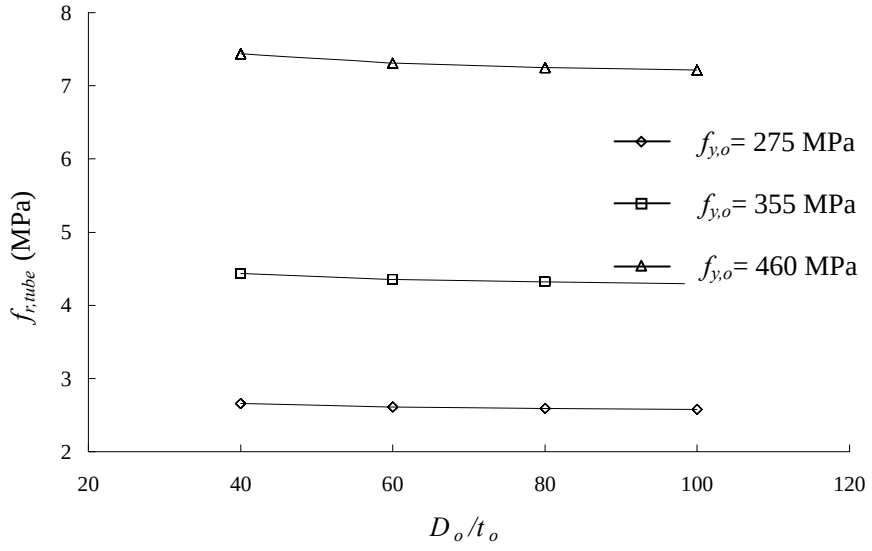

Figure 4 Confining pressure $f_{r,tube}$ against diameter-to-thickness ratio D_o/t_o

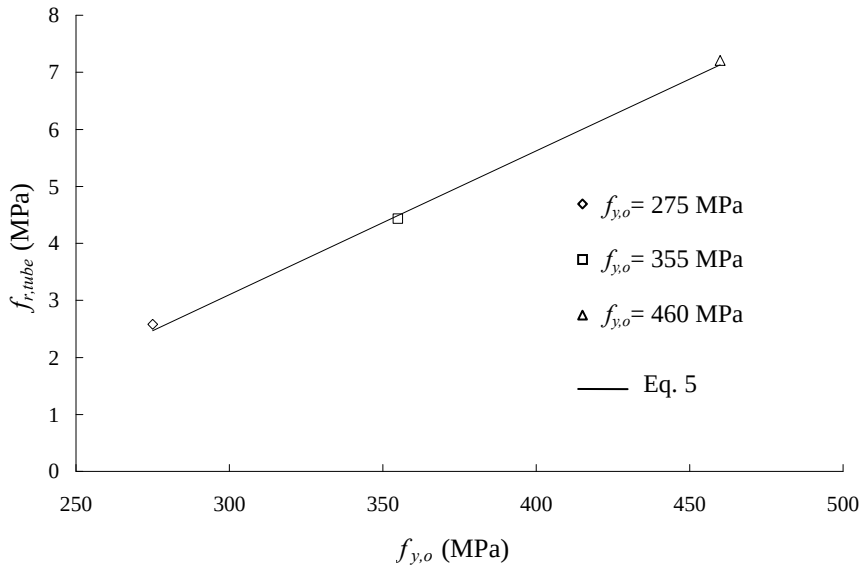

Figure 5 Confining pressure $f_{r,tube}$ against yield strength of outer steel tube $f_{y,o}$

3.2.2 Confining pressure provided by external rings ($f_{r,ring}$)

On the other hand, the relationship of confining pressure provided by external ring ($f_{r,ring}$) with other studied parameter needs to be determined in order to find out the total confining pressure f_r for a given double-skinned CFST column section. A new non-dimensional parameter of volumetric ratio of external confinement ρ_R is hence proposed, which is defined as the volume of steel rings (V_R) to the volume of concrete (V_c) in the double-skinned CFST columns. By this definition, the following mathematical expression for ρ_R can be derived:

$$\rho_R = \frac{V_R}{V_c} = \frac{n\pi(D_o + 2r_R)A_R}{h\pi\left[(\frac{D_o - 2t_o}{2})^2 - (\frac{D_i}{2})^2\right]} = \frac{4}{1-\chi^2}\frac{(D_o + 2r_R)A_R}{s(D_o - 2t_o)^2} \tag{6}$$

The confining pressure provided by the rings can be expressed in Eq. (7a) by considering the force equilibrium:

$$f_{r,ring} = \frac{2nA_R f_{y,R}}{(D_o - 2t_o)h} = \frac{f_{y,R}}{2}\frac{V_R}{V_c}(1-\chi^2)\frac{(D_o/t_o) - 2}{(D_o/t_o) + 2(r_R/t_o)} = \frac{f_{y,R}}{2}\rho_R(1-\chi^2)G \tag{7a}$$

where G is a geometric factor. It should be noted that in Eq. 7a, a uniform confining pressure is assumed to be produced by the rings on the steel tube and the concrete core. This can be justified as the rings spacing are small when compared with the diameter of the column. From Eq. 7a, it is seen that the geometric factor G depends on the diameter-to-thickness of the outer tube (D_o/t_o), as well as the ratio of radius of rings (r_R) to thickness of outer tube (t_o). Since (r_R/t_o) is much smaller than (D_o/t_o), and that r_R is similar to t_o, it can be deduced that G can be correlated reasonably well to just (D_o/t_o). Thus, the variation of G has been plotted against (D_o/t_o) for from 40 – 100 in Figure 6. From Figure 6, it is apparent that the variation of G against (D_o/t_o) varies within a narrow range from 0.90 to 0.96. For the purpose of practical design of CFST columns, a lower bound value of G = 0.90 is adopted. Hence, substituting G = 0.90 into Eq. 7a, the following equation is proposed for the confining pressure provided by the external rings:

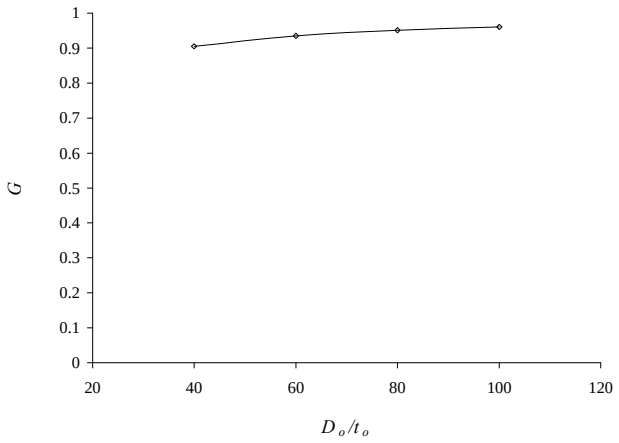

Figure 6 Minimum value of G against diameter-to-thickness D_o/t_o

$$f_{r,ring} = 0.45 f_{y,R} \rho_R (1 - \chi^2) \tag{7b}$$

The total confining pressure (f_r) can be obtained by adding up Eqs. 5 and 7b, which is given by Eq. 7c:

$$f_r = f_{r,tube} + f_{r,ring} = (0.025 f_{y,o} - 4.5) + 0.45 f_{y,R} \rho_R (1 - \chi^2) \tag{7c}$$

To verify the validity of the simplified equation for f_r as shown in Eq. 7c, the values of f_r calculated in the proposed model by Eqs. 3a, 4a and 4b are plotted against those calculated by Eq. 7c in Figure 7. It can be observed from the graph that both values are very close to each other.

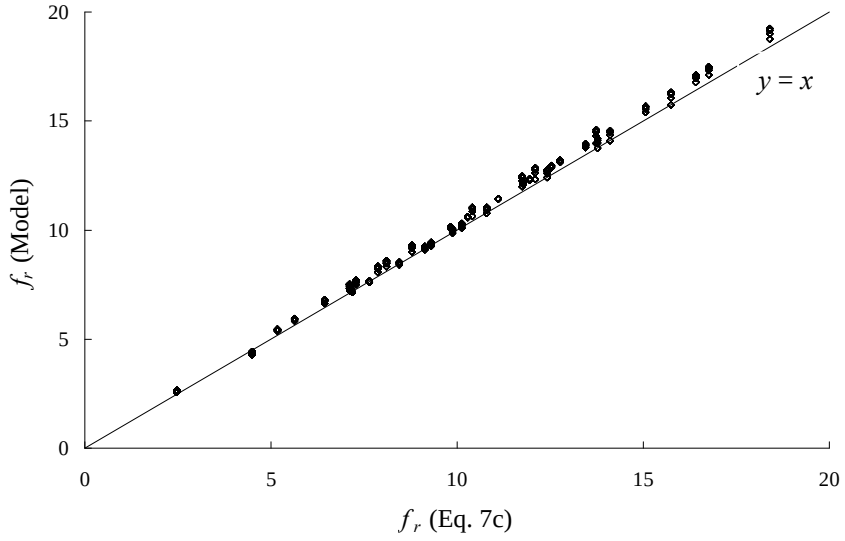

Figure 7 Comparison between the results obtained by model and Eq. 7c

3.2.3 Axial yield strength of the outer (f_o) tube and inner (f_i) tube under bi-axial state

Apart from the confining the pressure (f_r), it is essential to determine the yield stresses of both outer and inner tubes in order to assess the uni-axial load-carrying capacity of double-skinned CFST columns. For the outer tube, it is evident from Eqs. 2a, 3a and 4 that the major factors affecting

the yield stress of the steel tube under bi-axial state (f_o) are the confining pressure on the steel tube ($f_{r,tube}$), diameter-to-thickness ratio (D_o/t_o) and the uni-axial yield strength ($f_{y,o}$). Since $f_{r,tube}$ depends on D_o/t_o, it can be said that the major factors affecting the non-dimensional axial yield strength of the outer tube ($f_o/f_{y,o}$) are only (D_o/t_o) and $f_{y,o}$. From the results obtained in the parametric study, value of ($f_o/f_{y,o}$) have been plotted against the (D_o/t_o) in Figures 8(a) and 8(b). It is found from graphs that the value of ($f_o/f_{y,o}$) decreases as D_o/t_o increases for different yield strength and decreases as $f_{y,o}$ increases. An empirical formula is then set up correlating ($f_o/f_{y,o}$) to (D_o/t_o), $f_{y,o}$ and is written in Eq. 8.

$$\frac{f_o}{f_{y,o}} = 1 - \left[1.6\times10^{-7}\left(\frac{D_o}{t_o}\right)^2 - 1.4\times10^{-6}\left(\frac{D_o}{t_o}\right) \right] f_{y,o} \tag{8}$$

For the axial yield strength of the inner tube (f_i), it is noted from Eqs. 2b, 3b and 4 that the major factors affecting f_i are also the confining pressure ($f_{r,tube}$), diameter-to-thickness ratios of the outer tube (D_o/t_o) and inner tube (D_i/t_i). By the same token, the non-dimensional axial strength to yield strength ratio of the inner ($f_i/f_{y,i}$) is plotted against (D_i/t_i) for various steel yield strength in Figures 9(a) (D_o/t_o =40), 9(b) (D_o/t_o =60), 9(c) (D_o/t_o =80) and 9(d) (D_o/t_o =100). Unlike the outer steel tube, it is evident from Figure 9 that the value of f_i under bi-axial state is less significantly affected than that in outer tube f_o. The values of ($f_i/f_{y,i}$) were varying from 1.08 to 1.15. For the purpose of practical design of CFST columns, a lower bound value of 1.08 is adopted. An empirical formula is then set up for ($f_i/f_{y,i}$) and is shown in Eq. 9.

$$\frac{f_i}{f_{y,i}} = 1.08 \tag{9}$$

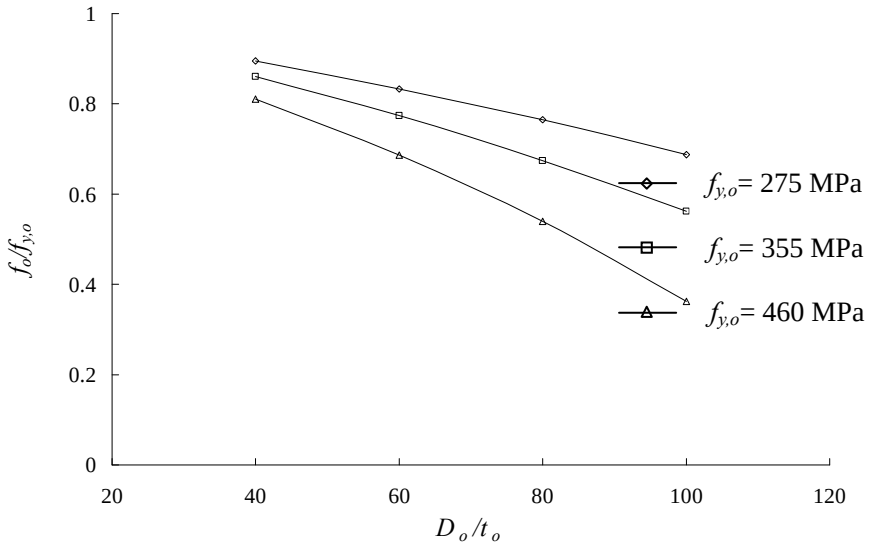

Figure 8(a) Axial-to-yield stress ratio (Outer Tube) against diameter-to-thickness ratio D_o/t_o

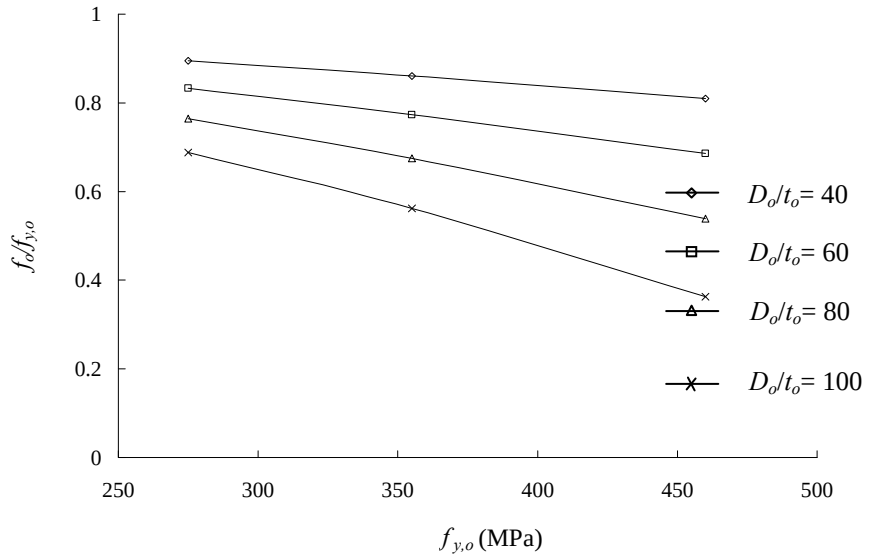

Figure 8(b) Axial-to-yield stress ratio (outer tube) against yield strength of outer tube $f_{y,o}$

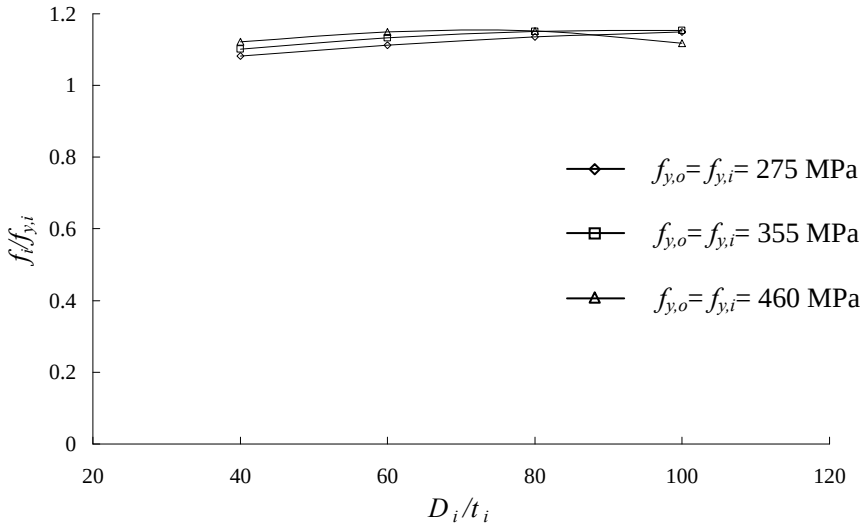

Figure 9(a) Axial-to-yield stress ratio (Inner tube) against diameter-to-thickness ratio of inner tube D_i/t_i for diameter-to-thickness ratio of outer tube D_o/t_o =40

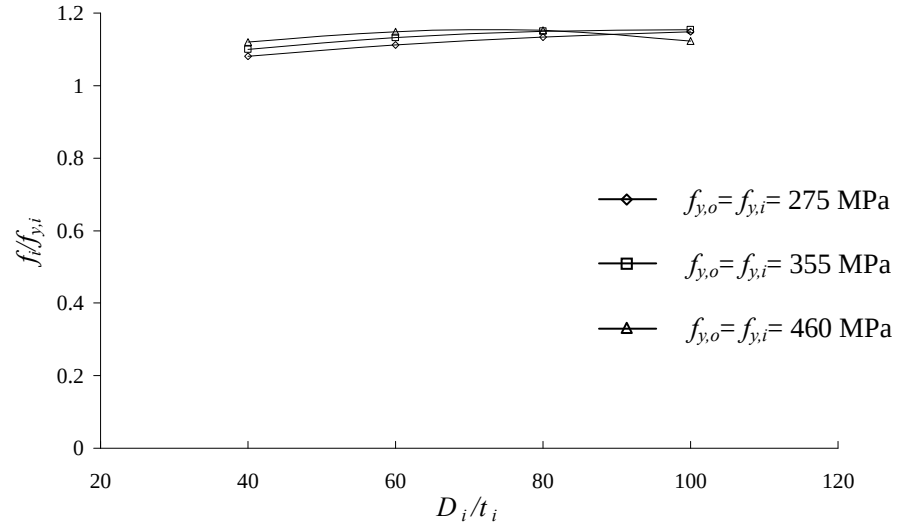

Figure 9(b) Axial-to-yield stress ratio (inner tube) against diameter-to-thickness ratio of inner tube D_i/t_i *for* diameter-to-thickness ratio of outer tube D_o/t_o =60

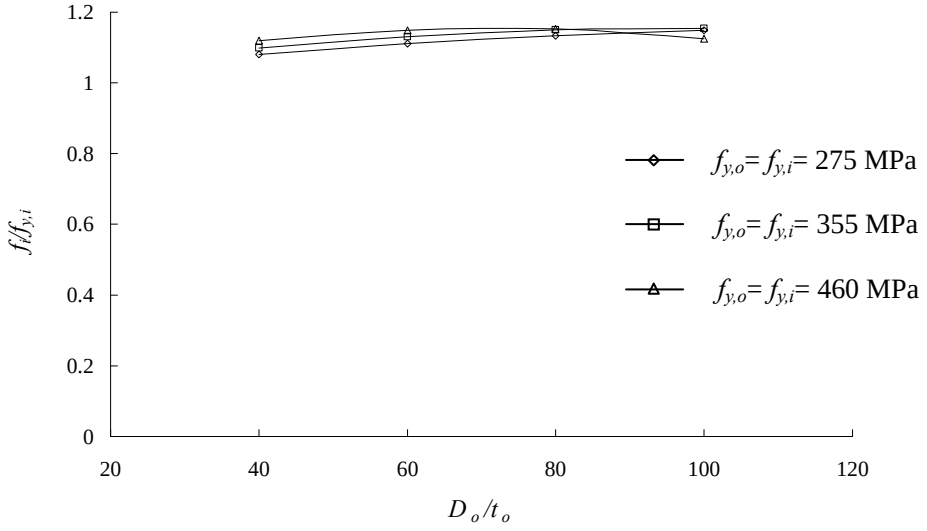

Figure 9(c) Axial-to-yield stress ratio (Inner tube) against diameter-to-thickness ratio of inner tube D_i/t_i *for* diameter-to-thickness ratio of outer tube D_o/t_o =80

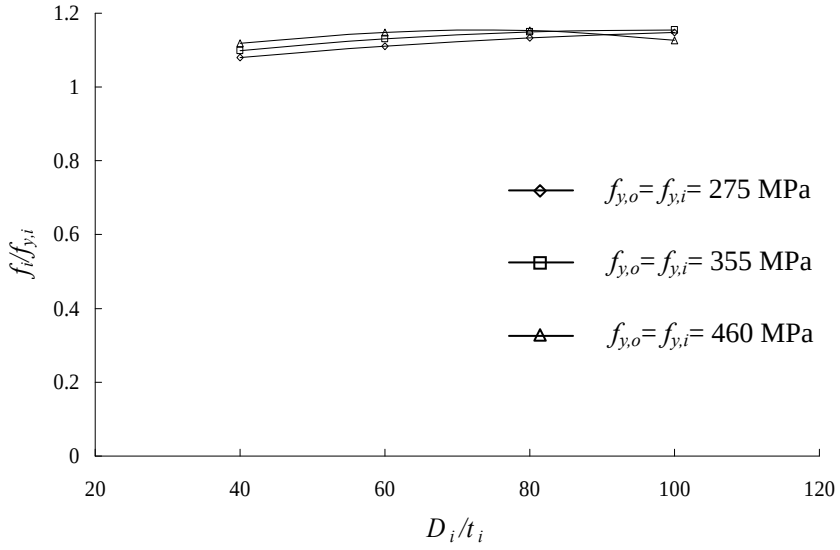

Figure 9(d) Axial-to-yield stress ratio (Inner tube) against diameter-to-thickness ratio of inner tube D_i/t_i *for* diameter-to-thickness ratio of outer tube

3.2.4 Confined concrete strength (f_{cc}) under confinement

As seen from Eq. 2c, the most critical factor affecting the confined concrete strength (f_{cc}) is the confining pressure (f_r). Substituting the empirical equation proposed for the confining pressure f_r as shown in Eq. 7c into Eq. 2c, the value of f_{cc} can be obtained.

3.2.5 Simplified equation for predicting uni-axial strength

From the first principle, the following equation can be adopted to evaluate the uni-axial strength of double-skinned CFST columns:

$$N_p' = f_{cc}A_c + f_oA_{so} + f_iA_{si} \tag{10}$$

where N_P' is the predicted uni-axial strength of double-skinned CFST column by the simplified equation, A_c, A_{so} and A_{si} are the cross-section areas of the concrete, outer steel tube and inner steel tube respectively. Substituting Eqs. 2c, 8 and 9 into Eq. 10, the following equation is obtained:

$$N_p' = Af_c'A_c + Bf_{y,o}A_{so} + Cf_{y,i}A_{si} \tag{11}$$

where $A = \left(1 + 4.1\frac{f_r}{f_c'}\right)$, $B = 1 - \left[1.6\times10^{-7}\left(\frac{D_o}{t_o}\right)^2 - 1.4\times10^{-6}\left(\frac{D_o}{t_o}\right)\right]f_{y,o}$ and $C = 1.08$. It is worth noting that since the strength enhancement in the inner steel tube due to confinement effect is relatively smaller (see Eq. 9), and that the cross-section area of the inner tube is considerably smaller than those of concrete and outer tube, it is believed that the influence of factor C is insignificant to the final result of the uni-axial load-carrying capacity N_p'. Hence, the authors propose to simply take the value of C as unity in all cases and the final form of equation is shown as follows:

$$N_p' = Af_c' A_c + Bf_{y,o} A_{so} + f_{y,i} A_{si} \quad (12)$$

The formula shown in Eq. 12 will be very useful to the structural designers for a prescribed uni-axial load-carrying capacity of doubled-skinned CFST columns. It is because Eq. 12 expresses the uni-axial load-carrying capacity in terms of some basic material and geometry parameters that can be obtained readily at early design stage. The formula will thus provide a straightforward method for designing the cross-section of double-skinned CFST column based on prescribed uni-axial strength.

The accuracy of the simplified formula as shown in Eq. 12 is checked by plotting the uni-axial strength calculated by Eq. 12 against that by the proposed model as shown in Eqs. 1 to 4 for all trial sections' results obtained in the parametric study (total specimen numbers > 3,000). The comparison is shown in Figure 10. The obtained average value and standard deviation of N_p/N_p' is 0.990 and 0.023 respectively, which suggests that the proposed simplified formula given in Eq. 12 is applicable for predicting and designing the uni-axial strength of double-skinned CFST columns with a wide range of geometric and material parameters.

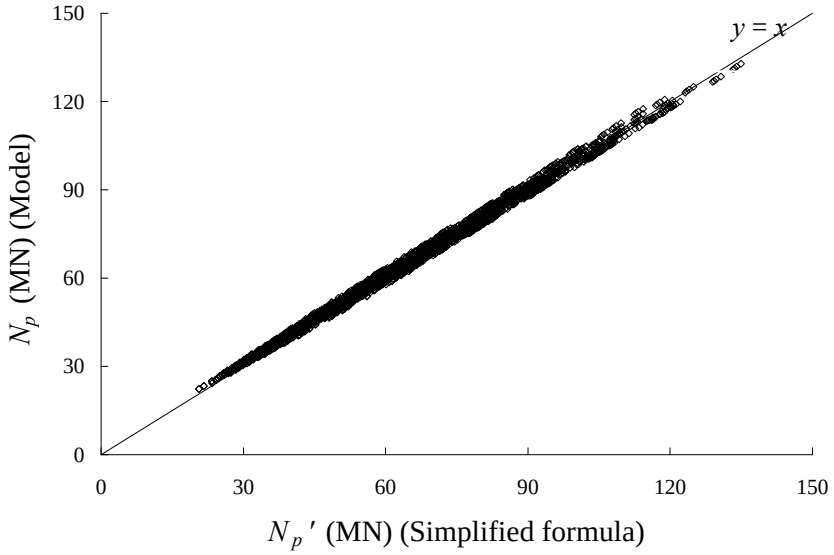

Figure 10. Comparison between the Results Obtained by Model and Simplified Formula

4. CONCLUSIONS

A new method of providing external confinement to restrict the lateral dilation of double-skinned CFST columns has been proposed and verified previously by uni-axial compression tests. A theoretical model has been developed for uni-axial load-carrying capacity for CFST columns that takes into account the confining effects provided by steel rings and steel tube. The validity of the proposed model has been verified by comparing with the experimental results obtained by the authors and other researchers on both confined and unconfined double-skinned CFST columns.

Using the developed model, a parametric study has been carried out to investigate the effects of various geometry and material factors on the uni-axial load-carrying capacity of confined double-skinned CFST columns. It has been identified that the confining pressure f_r is the major factor affecting the uni-axial strength. To facilitate practical design procedure without the need of going through the detailed calculation as per the proposed model, it is decided to establish empirical equation correlating the confining pressure f_r to various geometry and material factors.

By using the proposed empirical equation for f_r, the authors has eventually come up with a very simple formula capable of evaluating the uni-axial strength of confined double-skinned CFST columns based on only readily available design data, such as cross-section areas of concrete and steel tubes, as well as concrete cylinder and steel tube yield strength. The uni-axial strength predicted by the simplified equation has been compared with those obtained from the theoretical model, and excellent agreement was obtained. It is believed that the simplified equation can provide the structural designer a rapid and accurate design formula for estimating the uni-axial strength of double-skinned CFST column at early design stage based only on geometry and material factors.

ACKNOWLEDGEMENT

The work described in this paper has been substantially supported by a grant from the Research Grants Council of the Hong Kong Special Administrative Region, China (Project No. HKU 712310E). Technical supports for the experimental tests provided by the laboratory staff of the Department of Civil Engineering, The University of Hong Kong, are gratefully acknowledged.

LIST OF NOTATIONS

NSC	Normal-strength concrete
HSC	High-strength concrete
RC	Reinforced concrete
NSCFST	Normal-strength concrete-filled-steel-tubular
HSCFST	High-strength concrete-filled-steel-tubular
D_i	Outer diameter of inner tube of double-skinned CFST column
D_o	Outer diameter of outer tube of double-skinned CFST column
t_i	Thickness of inner tube of double-skinned CFST column
t_o	Thickness of outer tube of double-skinned CFST column
r_R	Radius of external steel bars
A_i	Cross-section area of the inner tube
A_o	Cross-section area of the outer tube
A_{cc}	Cross-section area of the core concrete
A_R	Cross-section area of external steel ring
χ	Hollow section ratio
N	Load-carrying capacity of a specimen
N_i	Axial load taken by the inner tube
N_o	Axial load taken by the outer tube
N_{cc}	Axial load taken by the core concrete
N_p	Axial strength of a specimen predicted by the proposed model
N_p'	Axial strength of a specimen predicted by simplified formula
N_t	Experimentally measured axial strength of a specimen
f_i	Axial stress of the inner tube
f_o	Axial stress of the outer tube

f_{cc}	Axial stress of the core concrete
f_c'	Uni-axial concrete compressive strength represented by cylinder strength
f_r	Confining pressure
$f_{r,tube}$	Confining pressure provided by the outer tube
$f_{r,ring}$	Confining pressure provided by external steel rings
$\sigma_{\theta,i}$	Hoop stress in inner tube of double-skinned CFST column
$\sigma_{\theta,o}$	Hoop stress in outer tube of double-skinned CFST column
σ_R	Tensile stress in external steel ring
$f_{y,i}$	Uni-axial yield strength of inner tube of double-skinned CFST column
$f_{y,o}$	Uni-axial yield strength of outer tube of double-skinned CFST column
$f_{y,R}$	Uni-axial yield strength of external steel ring
n	Number of external steel bars
h	Height of the specimen
s	Spacing of external steel rings
α_θ	Hoop stress ratio
G	Geometric factor
ρ_R	Volumetric ratio of external rings to concrete
V_R	Volume of steel rings
V_c	Volume of concrete

REFERENCES

[1] Goldman, A. and Bentur, A., “The Influence of Microfillers on Enhancement of Concrete Strength”, Cement and Concrete Research, 1993, Vol. 23, No. 4, pp. 962-972.

[2] Haque, M. and Kayali, O., “Properties of High-strength Concrete Using a Fine Fly Ash”, Cement and Concrete Research, 1998, Vol. 28, No. 10, pp. 1445-1452.

[3] Gettu, R., Bazant, Z.P. and Karr, M.E., “Fracture Properties and Brittleness of High-strength Concrete”, ACI Materials Journal, 1990, Vol. 87, No. 6, pp. 608-618.

[4] Cusson, D. and Paultre, P., “High-strength Concrete Columns Confined by Rectangular Ties”, Journal of Structural Engineering, 1994, Vol. 120, No. 3, pp. 783-804.

[5] Marzouk, H. and Chen, Z., “Fracture Energy and Tension Properties of High-strength Concrete”, Journal of Materials in Civil Engineering, 1995, Vol. 7, No. 2, pp. 108-116.

[6] Zhou, F., Barr, B. and Lydon, F., “Fracture Properties of High Strength Concrete with Varying Silica Fume Content and Aggregates”, Cement and Concrete Research, 1995, Vol. 25, No. 3, pp. 543-552.

[7] Ho, J.C.M. and Zhou, K.J.H., “Limited Deformability Design of High-strength Concrete Beams in Low to Moderate Seismicity Regions”, Journal of Civil Engineering and Management, 2011, Vol. 17, No. 3, pp. 409-423.

[8] Wright, H., Oduyemi, T. and Evans, H., “The Experimental Behaviour of Double Skin Composite Elements”, Journal of Constructional Steel Research, 1991, Vol. 19, No. 2, pp. 97-110.

[9] Wei, S., Mau, S.T., Vipulanandan, C. and Mantrala, S.K., “Performance of New Sandwich Tube under Axial Loading: Experiment”, Journal of Structural Engineering, 1995, Vol. 121, No. 12, pp. 1806-1814.

[10] Zhao, X.L. and Grzebieta, R., “Strength and Ductility of Concrete Filled Double Skin (SHS Inner and SHS Outer) Tubes”, Thin-walled Structures, 2002, Vol. 40, No. 2, pp. 199-213.

[11] Zhao, X.L., Grzebieta, R. and Elchalakani, M., “Tests of Concrete-filled Double Skin CHS Composite Stub Columns”, Steel and Composite Structures, 2002, Vol. 2, No. 2, pp.129-146.
[12] Giakoumelis, G. and Lam, D., “Axial Capacity of Circular Concrete-filled Tube Columns”, Journal of Constructional Steel Research, 2004, Vol. 60, No. 7, pp. 1049-1068.
[13] Tao, Z., Han, L.H. and Zhao, X.L., “Behaviour of Concrete-filled Double Skin (CHS Inner and CHS Outer) Steel Tubular Stub Columns and Beam-columns”, Journal of Constructional Steel Research, 2004, Vol. 60, No. 8, pp. 1129-1158.
[14] Young, B. and Ellobody, E., “Experimental Investigation of Concrete-filled Cold-formed High Strength Stainless Steel Tube Columns”, Journal of Constructional Steel Research, 2006, Vol. 62, No. 5, pp. 484-492.
[15] Dabaon, M., El-Khoriby, S., El-Boghdadi, M. and Hassanein, M.F., “Confinement Effect of Stiffened and Unstiffened Concrete-filled Stainless Steel Tubular Stub Columns”, Journal of Constructional Steel Research, 2009, Vol. 65, No. 8, pp. 1846-1854.
[16] Kuranovas, A., Goode, D., Kvedaras, A.K. and Zhong, S., “Load-bearing Capacity of Concrete-filled Steel Columns”, Journal of Civil Engineering and Management, 2009, Vol. 15, No. 1, pp. 21-33.
[17] de Oliveira, W.L.A., De Nardin, S., El Debs, A.L.H. and El Debs, M.K., “Evaluation of Passive Confinement in CFT Columns”, Journal of Constructional Steel Research, 2010, Vol. 66, No. 4, pp. 487-495.
[18] Szmigiera, E., Zoltowski, W. and Siennicki, M., “Research on Load Capacity of Concrete Filled Columns with Battened Steel Sections”, Journal of Civil Engineering and Management, 2010, Vol. 16, No. 3, pp. 313-319.
[19] Li, G.C., Lang, Y. and Yang, Z.J., “Behavior of High Strength CFSST Stub Columns with Inner CFRP Tube under Axial Compressive Load”, Advanced Steel Construction, 2011, Vol. 7, No. 3, pp. 239-254.
[20] Yu, F., He, S.H. and Niu, D.T., “Study on Unified Bearing Capacity of Rectangular Concrete-filled Steel Tubular Column Subjected to Axial Compression”, Advanced Steel Construction, 2012, Vol. 8, No. 1, pp. 95-111.
[21] Elchalakani, M., Zhao, X.L. and Grzebieta, R., “Concrete-filled Circular Seel Tubes Subjected to Pure Bending”, Journal of Constructional Steel Research, 2001, Vol. 57, No. 11, pp. 1141-1168.
[22] Lin, M. and Tsai, K.C., “Behavior of Double-skinned Composite Steel Tubular Columns Subjected to Combined Axial and Flexural Loads”, Proceedings of the First International Conference on Steel and Composite Structures, Pusan, Korea, 14-16 June, 2001, pp. 1145-52.
[23] Chitawadagi, M.V. and Narasimhan, M.C., “Strength Deformation Behaviour of Circular Concrete Filled Steel Tubes Subjected to Pure Bending”, Journal of Constructional Steel Research, 2009, Vol. 65, No. 8, pp. 1836-1845.
[24] Lu, H., Han, L.H. and Zhao, X.L., “Analytical Behavior of Circular Concrete-filled Thin-walled Steel Tubes Subjected to Bending”, Thin-walled Structures, 2009, Vol. 47, No. 3, pp. 346-358.
[25] Kitada, T., “Ultimate Strength and Ductility of State-of-the-art Concrete-filled Steel Bridge Piers in Japan", Engineering Structures, 1998, Vol. 20, No. 4, pp. 347-354.
[26] Schneider, S.P., “Axially Loaded Concrete-filled Steel Tubes”, Journal of Structural Engineering, 1998, Vol. 124, No. 10, pp. 1125-1138.
[27] Elremaily, A. and Azizinamini, A., “Behavior and Strength of Circular Concrete-filled Tube Columns”, Journal of Constructional Steel Research, 2002, Vol. 58, No. 12, pp. 1567-1591.
[28] Varma, A.H., Ricles, J.M., Sause, R. and Lu, L.W., “Seismic Behavior and Modeling of High-strength Composite Concrete-filled Steel Tube (CFT) Beam–columns”, Journal of Constructional Steel Research, 2002, Vol. 58, No. 5, pp. 725-758.

[29] Sakino, K., Nakahara, H., Morino, S. and Nishiyama, I., “Behavior of Centrally Loaded Concrete-filled Steel-tube Short Columns”, Journal of Structural Engineering, 2004, Vol. 130, No. 2, pp. 180-188.
[30] Yang, Y. and Han, L.H., “Concrete-filled Double-skin Tubular Columns under Fire”, Magazine of Concrete Research, 2008, Vol. 60, No. 3, pp. 211-222.
[31] Lu, H., Han, L.H. and Zhao, X.L., “Fire Performance of Self-consolidating Concrete Filled Double Skin Steel Tubular Columns: Experiments”, Fire Safety Journal, 2010, Vol. 45, No. 2, pp. 106-115.
[32] Zhao, X.L., Tong, L.W. and Wang, X.Y., “CFDST Stub Columns Subjected to Large Deformation Axial Loading”, Engineering Structures, 2010, Vol. 32, No. 3, pp. 692-703.
[33] Li, G.C., Sun, W. and Leon, R.T., “Hysteretic Performance of Steel Beam to Gangue CFST Column Connections with Ring Stiffeners under Low Reversed Cyclic Loading”, Advanced Steel Construction, 2011, Vol. 7, No. 2, pp. 173-181.
[34] Montejo, L.A., González-Román, L.A. and Kowalsky, M.J., “Seismic Performance Evaluation of Reinforced Concrete-filled Steel Tube Pile/Column Bridge Bents”, Journal of Earthquake Engineering, 2012, Vol. 16, No.3, pp. 401-424.
[35] Shakir-Khalil, H., “Composite Columns of Double-skinned Shells”, Journal of Constructional Steel Research, 1991, Vol. 19, No. 2, pp. 133-152.
[36] Yang, J., Xu, H. and Peng, G., “Behavior of Concrete-filled Double Skin Steel Tubular Columns with Octagon Section under Axial Compression”, Frontiers of Architecture and Civil Engineering in China, 2008, Vol. 2, No. 3, pp. 205-210.
[37] Huang, Y.H., Wang, R.H. and Huang, X.F., “Calculation of the Interfacial Tensile Stress of CFST Members under Axial Pressure”, Advanced Materials Research, 2011, Vol. 250, pp. 1638-1645.
[38] Köster, W. and Franz, H., “Poisson's Ratio for Metals and Alloys”, Metallurgical Reviews, 1961, Vol. 6, No. 1, pp. 1-56.
[39] Persson, B., “Poisson's Ratio of High-performance Concrete”, Cement and Concrete Research, 1999, Vol. 29, No. 10, pp. 1647-1653.
[40] Ferretti, E., “On Poisson's Ratio and Volumetric Strain in Concrete”, International Journal of Fracture, 2004, Vol. 126, No. 3, pp. 49-55.
[41] Lu, X. and Hsu, C.T.T., “Tangent Poisson's Ratio of High-strength Concrete in Triaxial Compression”, Magazine of Concrete Research, 2007, Vol. 59, No. 1, pp. 69-77.
[42] Dong, C.X.; Ho, J.C.M., “Uni-axial Behaviour of Normal-strength CFDST Columns with External Steel Rings”, Steel and Composite Structures,2012, Vol. 13, No. 6, pp. 587-606.
[43] Ho, J.C.M. and Luo, L., “Uni-axial Behaviour of Normal-strength Concrete-filled-steel-tube Columns with External Confinement”, Earthquake and Structures, 2012. (in press)
[44] Lai, M.H. and Ho, J.C.M., “Behaviour of Uni-axially Loaded Concrete-filled-steel-tube Columns Confined by External Rings”, The Structural Design of Tall and Special Buildings, 2012, DOI: 10.1002/tal.1046.
[45] Huang, C., Yeh, Y.K., Liu, G.Y., Hu, H.T., Tsai, K., Weng, Y.T., Wang, S.H. and Wu, M.H., “Axial Load Behavior of Stiffened Concrete-filled Steel Columns”, Journal of Structural Engineering, 2002, Vol. 128, No. 9, pp. 1222-1230.
[46] Tao, Z., Han, L.H. and Wang, Z.B., “Experimental Behaviour of Stiffened Concrete-filled Thin-walled Hollow Steel Structural (HSS) Stub Columns”, Journal of Constructional Steel Research, 2005, Vol. 61, No. 7, pp. 962-983.
[47] Cai, J. and He, Z.Q., “Axial Load Behavior of Square CFT Stub Column with Binding Bars”, Journal of Constructional Steel Research, 2006, Vol. 62, No. 5, pp. 472-483.
[48] Tao, Z., Han, L.H. and Wang, D.Y., “Experimental Behaviour of Concrete-filled Stiffened Thin-walled Steel Tubular Columns”, Thin-walled Structures, 2007, Vol. 45, No. 5, pp. 517-527.

[49] Tao, Z. and Han, L.H., “Behaviour of Concrete-filled Double Skin Rectangular Steel Tubular Beam–columns”, Journal of Constructional Steel Research, 2006, Vol. 62, No. 7, pp. 631-646.
[50] Tan, K.H. and Zhang, Y.F., “Compressive Stiffness and Strength of Concrete Filled Double Skin (CHS Inner & CHS Outer) Tubes”, International Journal of Mechanics and Materials in Design, 2010, Vol. 6, No. 3, pp. 283-291.
[51] Uenaka, K., Kitoh, H. and Sonoda, K., “Concrete Filled Double Skin Circular Stub Columns under Compression”, Thin-walled Structures, 2010, Vol. 48, No.1, pp. 19-24.
[52] Hu, H.T. and Su, F.C., “Nonlinear Analysis of Short Concrete-filled Double Skin Tube Columns Subjected to Axial Compressive Forces”, Marine Structures, 2011, Vol. 24, No. 4, pp. 319-337.
[53] EC4, Eurocode 4, Eurocode 4: Design of Composite Steel and Concrete Structures: Part 1-1: General Rules and Rules for Buildings, UK, 2004.
[54] Han, L.H., Ren, Q.X. and Li, W., “Tests on Stub Stainless Steel-concrete-carbon Steel Double-skin Tubular (DST) Columns”, Journal of Constructional Steel Research, 2011, Vol. 67, No. 3, pp. 437-452.
[55] Mander, J. and Priestley, M.J.N., “Theoretical Stress-strain Model for Confined Concrete”, Journal of Structural Engineering, 1988, Vol. 114, No. 8, pp. 1804-1826.
[56] Hatzigeorgiou, G.D., “Numerical Model for the Behavior and Capacity of Circular CFT Columns, Part I: Theory”, Engineering Structures, 2008, Vol. 30, No. 6, pp. 1573-1578.

THE BEHAVIOR OF INFILLED STEEL FRAMES UNDER REVERSE CYCLIC LOADING

M. Yasar Kaltakci [1] and Ali Koken [2,*]

[1] *Professor, Department of Civil Engineering, Engineering Faculty, Selcuk University, Konya, Turkey*
[2] *Assistant Professor, Department of Civil Engineering, Engineering Faculty, Selcuk University, Konya, Turkey*
**(Corresponding author: E-mail: : akoken@selcuk.edu.tr)*

Received: 8 November 2012; Revised: 14 January 2013; Accepted: 13 March 2013

ABSTRACT: The objective of this study was to make an experimental investigation on the behavior of nine steel frames with various infill characteristics under reverse cyclic loading. The test specimens, which were one-story steel frames, had the frame length/height ratios (l/h) of 1, ½, and 2. The infill characteristics of the specimens were assigned as i) no infill, ii) brick wall infill, iii) brick wall+plaster infill. The specimens were tested under reverse cyclic loading representing the seismic loading in the horizontal direction, and the displacement values obtained during the tests were measured and recorded in a digital manner. At the end of the tests, the infilled frames were evaluated in terms of failure types, strength envelopes, energy consumption characteristics, and stiffness decreases by comparing the test results.

Keywords: Steel frames with infill walls, seismic behavior of infilled steel frames

1. INTRODUCTION

It is a known reality that infill walls considerably change the behavior of frames under horizontal loads and especially affect the strength, rigidity, and energy consumption properties. Studies on the structural behavior and response of masonry infilled frames trace back to as early as the 1950s [4]. The behavior of infilled frames under lateral loads has been investigated by a number of researchers. Findings and theories pertaining to infilled frames since the 1950s to the late 1980s were presented in a state of the art report prepared by Moghaddam et al. [12]. In general, researchers employed two different testing schemes in their investigations. The first was in-plane, diagonal, and compressive loading of a single frame unit, and the second in a plane racking test in which the frame is subjected to a top lateral load [4]. Holmes [5], Stafford [13, 14], Mainstone and Weeks [10], Dawe and Seah [1], Flangan et al. [3], Mander et al. [11], and Dukuze et al [2] have studied the behavior of masonry infilled steel frames under lateral loads [9].

In this study, an experimental investigation was executed to explore the effect of infill walls on steel frame systems in which infill walls are not generally taken into consideration in the structural analysis. Nine single story steel frame systems with various infill wall properties were tested under horizontal a reverse cycling load simulating a seismic load, and the results were examined and concluded [6], [7], [8].

2. OBJECT AND SCOPE

The objective of this study is to investigate the following: the effect of infill walls on strength, horizontal rigidity and energy consumption capacity of steel frames under a horizontal load, the failure types of infilled steel frame systems, and the effects of various infill wall properties and infill wall length/height (l/h) ratios on the seismic behavior of the steel frame system. With this purpose, throughout the study, nine steel frame systems on approximately a 1/3 scale were tested under reverse cycling horizontal loading. The variables considered in deciding the test specimens

were the length/height (l/h) ratio of the infill wall and properties of the infill wall. Considering these variables, the following test specimens were prepared and the experiments were performed.

1. Frame systems of infill wall length/height ratio (l/h) = 1, **a**-frame system with no infill – N110 (l/h = 1), **b**-Steel frame system with brick wall infill – N111 (l/h = 1), **c**- frame system with brick wall + plaster infill – N112 (l/h = 1)

2. Frame systems of infill wall length/height ratio (l/h) = 2, **a**- frame system with no infill – N110 (l/h = 2), **b**-Steel frame system with brick wall infill – N111 (l/h = 2), **c**- frame system with brick wall + plaster infill – N112 (l/h = 2)

3. Frame systems of infill wall length/height ratio (l/h) = 1/2 , **a**-frame system with no infill – N110 (l/h = 1/2), **b**-frame system with brick wall infill – N111 (l/h = 1/2), **c**-frame system with brick wall + plaster infill –N112 (l/h=1/2)

3. PRESENTATION OF TEST MECHANISM AND TEST TECHNIQUE

U-profiles, manufactured by bending cold steel plates for the preparation of steel frames, were used. Welding these U-profiles with arc welding, steel frames were formed with rigid nodal points and infill walls with various properties were placed there inside the steel frames. For brick wall infill, a horizontal hollow block brick of 190×185×85 mm was used. The brick wall+plaster infilled specimens had 17.5 mm plaster formed from lime with added cement mortar on both sides of the brick wall. For the masonry of the brick wall and plaster, the same cement mortar was used. The physical and geometric properties of the prepared test specimens are given in Table 1.

Table 1. Physical and Geometric Characteristics of Test Specimens

Specimens	Infill properties	Frame length (l)	Frame height (h)	Infill length (l_p)	Infill height (h_p)
N110 (l/h=1)	No infill (empty)	843.7	823.7	810	790
N111 (l/h=1)	Brick wall infill	843.7	823.7	810	790
N112 (l/h=1)	Brick wall+ plaster infill	843.7	823.7	810	790
N110 (l/h=2)	No infill (empty)	1643.7	823.7	1610	790
N111 (l/h=2)	Brick wall infill	1643.7	823.7	1610	790
N112 (l/h=2)	Brick wall+ plaster infill	1643.7	823.7	1610	790
N110 (l/h=1/2)	No infill (empty)	843.7	1603.7	810	1570
N111 (l/h=1/2)	Brick wall infill	843.7	1603.7	810	1570
N112 (l/h=1/2)	Brick wall+ plaster infill	843.7	1603.7	810	1570

3.1 Test Technique

The experimental part of this study was performed in the structure laboratory of Selcuk University. The prepared nine steel frame specimens with various properties were tested under a horizontal reverse cycling load, which simulates seismic load by using a rigid loading frame system. During the experiment, the necessary load and displacement readings were made and recorded using a computer-aided data reading system. The experiment mechanism used in the tests is presented in Figure 1.

The rigid loading frame was manufactured from various steel profiles and designed properly to apply the horizontal load. The system had a rigid base plate that enabled test specimens to be rigidly supported. The specimens could be rigidly supported to the rigid base plate using bolts. Thus, any rotation and translation of the specimen at the bottom were prevented. The horizontal load was applied to the steel frame specimen with the assistance of a hydraulic jack and a tension bar that was fixed on the loading plate supported on the vertical columns of the rigid loading frame. The hydraulic jack system could operate bi-directionally, meaning that it could apply both tension and compression force to the specimen. While the hydraulic jack system pushes the specimen fastened with the bolts in the compression stage, it pulls the specimen in the tension stage with the help of the steel tension bar of ϕ 40 mm and extending to the back end of the specimen at the top capital. In this way, it was possible to apply a horizontal reverse cycling load to the specimen. The steel bar also aided in preventing the specimen from tilting. In order to prevent the tilting of the specimens, steel profiles fixed to the horizontal branches of the rigid loading frame were used. While the branches perpendicular to the test frame that were welded to the profiles in the vertical position did not prevent the movement of the specimen through the loading direction with the shear loading mechanism, they only prevented the tilting of the specimen during load application by not taking on any load. A load cell together with the hydraulic jack was placed on the loading plate supported by the vertical branches of the rigid loading frame to perform the load readings. The loading frame was designed as rigid as possible to minimize horizontal and vertical motion, and the rotation of the loading mechanism formed from a pump and a load cell at values closer to zero so not affect the measurements during the test.

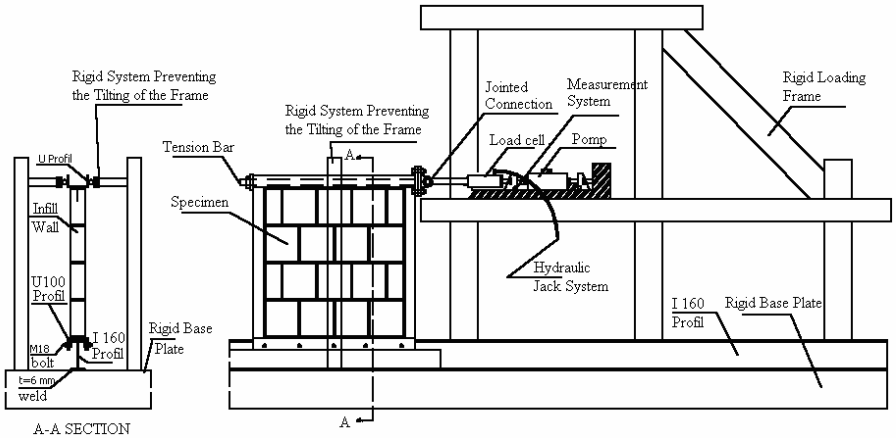

Figure. 1 The Loading System used in the Tests

3.2 The Measurement Mechanism Used in the Tests

A measurement system that was as similar as possible was used for every frame tested in the experiments. The measurement of the displacements occurred at the steel frame and the infill wall during the test that was performed using LVDTs of 0.01 mm accuracy. The required numbers of LVDTs are placed in the necessary locations to determine the horizontal displacements of the bottom and top ends of the steel frame system and rotations at the bottom and top capitals. Load measurements are made by using a load cell working in contact with the hydraulic jack. The measurement mechanism used in the tests is presented in Figure 2.

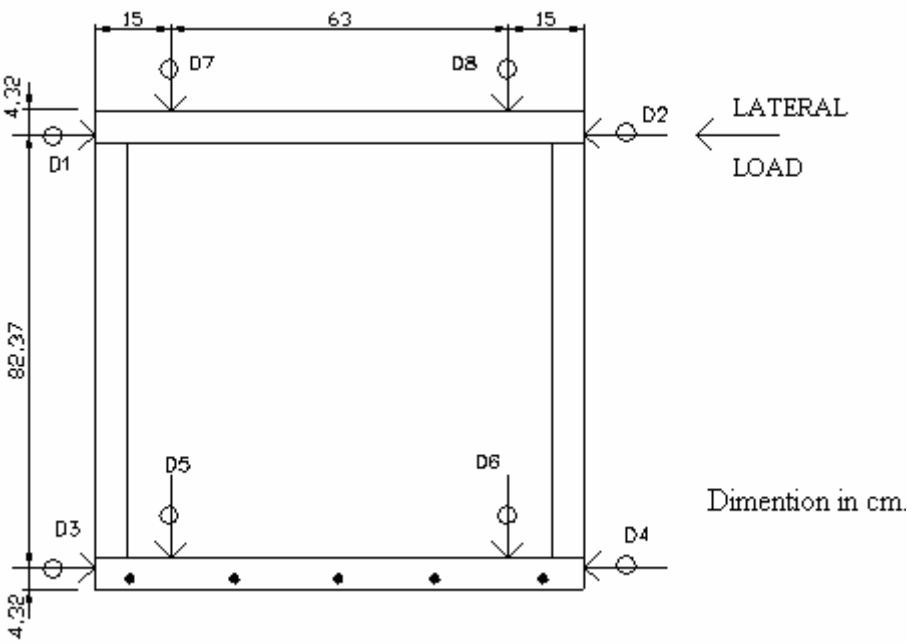

Figure 2. The Measurement Mechanism used for l/h=1 Tests

3.3 Loading Program

All the tests were carried out under displacement control. The loading control was performed by beginning from the stationary position and increasing 10 mm in each cycle as given in Figure 3. The purpose of selecting such a loading program was to determine a systematic method in comparing the results between the specimens, because each of the frame system has different structural characteristics (empty, infilled with brick wall, infilled with brick wall + plaster). Therefore, each frame system would be evaluated according to horizontal displacement and (δ/h) ratio with the desired behavior characteristics and compared with other specimens.

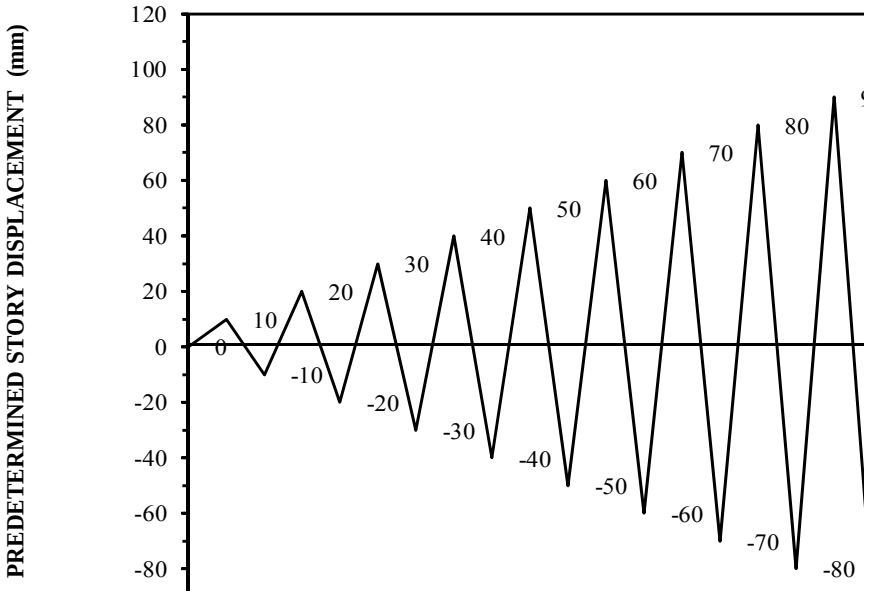

Figure 3. The Loading Program Applied in the Tests

4. RESULTS

After the experiment, for each test specimen, the strength envelope, rigidity decline graphics and energy consumption graphics were obtained and these results were compared with each other.

4.1 The Effect of Infill Wall Length/Infill Wall Height (l/h) to the Behavior of the Frame Systems

4.1.1 Frame systems with Infill Wall Length / Infill Wall Height (l/h = 1)

The experimental test results of the three frame systems with infill wall length/infill wall height (l/h = 1) are examined in this section. The aforementioned test specimens are the empty frame system N110, brick wall infilled frame system N111, and brick wall+plaster infilled frame system N112. The strength envelopes of the specimens are given in Figure 4. The maximum horizontal load values are found as 32.37 kN (N110), 41.42 kN (N111), and 56.92 kN (N112) respectively. When the empty frame system was taken as the reference, the increase in the carried horizontal load was 28% in the brick wall infilled system and 76% in the brick wall+plaster infilled system. The brick wall+plaster infilled system bears 37% more horizontal load compared to the brick wall infilled system. It was observed that after the third cycle, the carried horizontal loads decreased in the brick wall and brick wall+plaster infilled systems.

The rigidity decline graphics obtained from the tests of the aforementioned specimens are given in Figure 5. The first cycle rigidities are 1.17 kN/mm (N110), 2.55 kN/mm (N111), and 3.06 kN/mm (N112). However, the rigidities decreased in subsequent cycles. The rigidity decrease is more rapid in the brick wall and brick wall+plaster infilled systems than the empty frame systems. Generally during the fifth cycle ($\delta/H=0.0607$) the rigidity values in all of the frame systems decrease to approximately 0.5 – 0.7 kN/mm. Observations made during the experiments revealed that in the fifth cycles a lateral buckling generally begins at the bottom ends of the columns. After this cycle, all systems presented empty frame behavior characteristics. In terms of rigidities obtained from the first cycle, when the reference empty frame was considered as a base, the increase in the first cycle rigidities was 118% for the brick wall infilled system and 160% for the brick wall+plaster infilled system.

The cumulative consumed energy graphics determined from the tests are also given in Figure 6. The cumulative consumed energy values after the eighth cycle are 10878 kNmm, 14877 kNmm, and 17978 kNmm, respectively. When the reference empty frame was considered as a base, the increase in the cumulative consumed energy was 37% for the brick wall infilled system and 65% for the brick wall+plaster infilled system.

4.1.2 Frame systems with infill wall length/infill wall height (l/h=2)

The test results belonging to the three frame systems with infill wall length/infill wall height (l/h=2) are examined in this section. The test specimens were the empty frame system N110, the brick wall infilled frame system N111, and the brick wall+plaster infilled frame system N112. The related specimens' strength envelopes are presented in Figure 7.

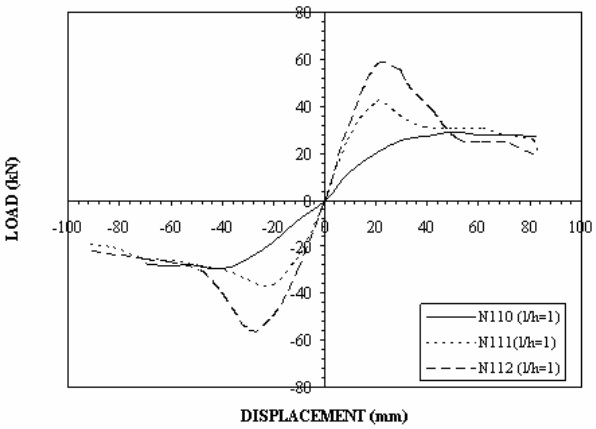

Figure 4. Strength Envelopes of Frame Systems with Infill Wall Length/ Infill Wall Height (l/h=1)

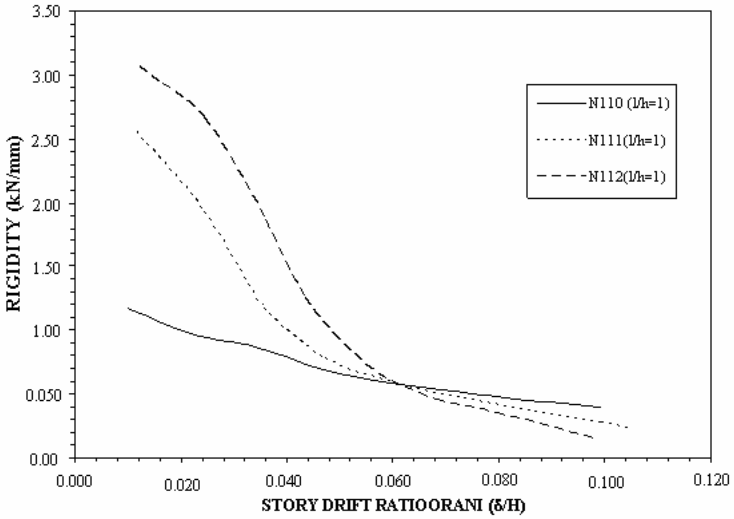

Figure 5. Rigidity Decreasing Graphics of Frame Systems with Infill Wall Length/ Infill Wall Height (l/h=1)

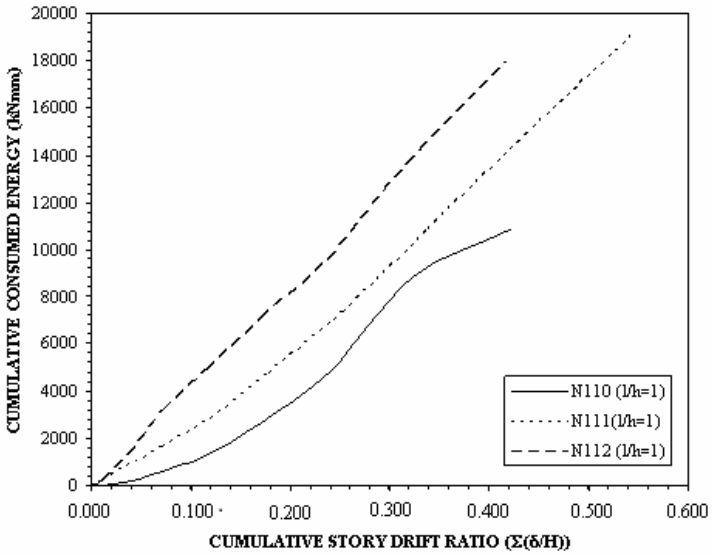

Figure 6. Cumulative Consumed Energy Graphics of Frame Systems with Infill Wall Length/Infill Wall Height (l/h=1)

As seen from Figure 7, the carried maximum horizontal loads were found as 27.15 kN (N110), 45.40 kN (N111), and 65.86 kN (N112), respectively. When the reference empty frame was considered as a base, the increase in the carried horizontal load was 67% for the brick wall infilled system and 142% for the brick wall+plaster infilled system. In the brick wall infilled and brick wall+plaster infilled systems, a general decrease was observed in the carried horizontal load after the second cycle. The rigidity decline graphics obtained from the tests are given in Figure 11.

Looking at Figure 8, while the first cycle rigidity values were 1.21 kN/mm (N110), 3.83 kN/mm (N111), and 4.19 kN/mm (N112), respectively, the rigidities decreased in the subsequent cycles. While the rigidity decrease was more rapid in the brick wall infilled and brick wall+plaster infilled systems, the rigidity decrease in the empty frame system was slower. Generally, the rigidity values in all frame systems in the fifth cycle ($\delta/H=0.0607$) decrease to approximately 0.5 – 0.7 kN/mm. Observations made during the experiments revealed that generally in the fifth cycles ($\delta/H=0.0607$) a lateral buckling began at the bottom ends of the columns. After this cycle, all systems presented empty frame behavior characteristics. In terms of rigidities obtained from the first cycle, when the reference empty frame was considered as a base, the increase in the first cycle rigidities was 216% for the brick wall infilled system and 246% for the brick wall+plaster infilled system.

The cumulative consumed energy graphics are also given in Figure 9. The cumulative consumed energy values after the eighth cycle are 13237 kNmm, 17406 kNmm, and 17886 kNmm, respectively. When the reference empty frame was considered as a base, the increase in the cumulative consumed energy became 31% for the brick wall infilled system and 35% for the brick wall+plaster infilled system.

4.1.3 Frame systems with infill wall length/infill wall height (l/h=1/2)

The test results belonging to three frame systems with infill wall length/infill wall height (l/h=1/2) are examined in this section. The test specimens are the empty frame system N110, brick wall infilled frame system N111, and the brick wall+plaster infilled frame system N112. The related specimens' strength envelopes are presented in Figure 10. The carried maximum horizontal loads were found to be 12.97 kN (N110), 23.64 kN (N111), and 28.60 kN (N112), respectively. When the reference empty frame was considered, the increase in the carried horizontal load was 82% for the brick wall infilled system and 121% for the brick wall+plaster infilled system.

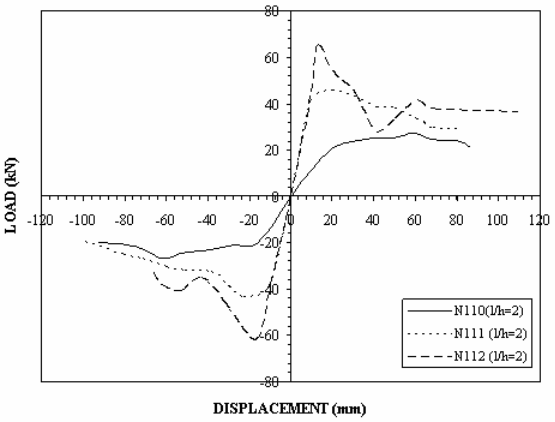

Figure 7. Strength Envelopes of Frame Systems with Infill Wall Length/ Infill Wall Height (l/h=2)

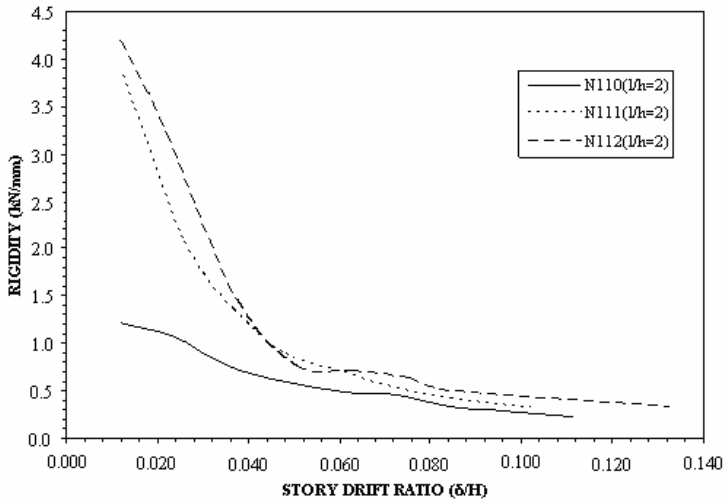

Figure 8. Rigidity Decreasing Graphics of Frame Systems with Infill Wall Length/ Infill Wall Height (l/h=2)

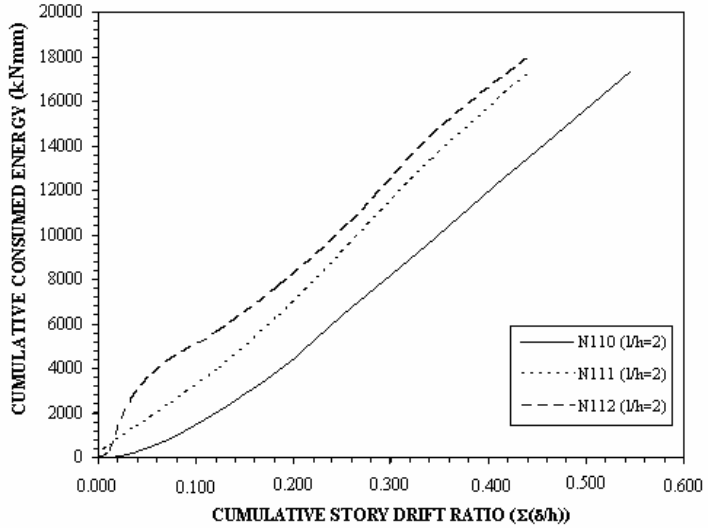

Figure 9. Cumulative Consumed Energy Graphics of Frame Systems with Infill Wall Length/Infill Wall Height (l/h=2)

The rigidity decrease graphics obtained from the specimen tests are given in Figure 11. While the first cycle rigidity values were 0.38 kN/mm/ (N110), 1.05 kN/mm (N111), and 1.18 kN/mm (N112), respectively, the rigidities decreased in the subsequent cycles. While the rigidity decrease was more rapid in the brick wall infilled and brick wall+plaster infilled systems, the rigidity decrease in empty frame system was slower. After the sixth cycle (δ/H=0.0374) the decrease in rigidity values of all frame systems was slowed and the rigidity values decreased approximately to 0.15 – 0.40 kN/mm. In terms of rigidities obtained from the first cycle, when the reference empty frame was considered as a base, the increase in the first cycle rigidities was 176% for the brick wall infilled system and 210% for the brick wall+plaster infilled system.

The cumulative consumed energy graphics determined from the tests are also given in Figure 12. The cumulative consumed energy values after the ninth cycle are 2991 kNmm (N110), 5871 kNmm (N111), and 7429 kNmm (N112), respectively. When the reference empty frame was considered as a base, the increase in the cumulative consumed energy was 96% for the brick wall infilled system and 148% for the brick wall+plaster infilled system.

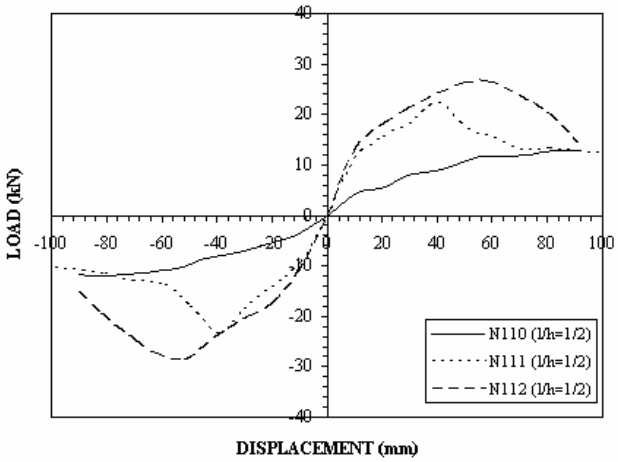

Figure 10. Strength Envelopes of Frame Systems with Infill Wall Length/ Infill Wall Height (l/h=1/2)

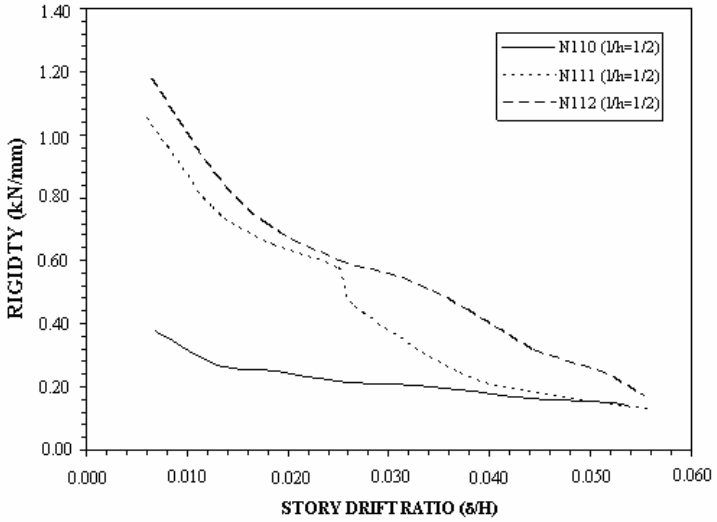

Figure 11. Rigidity Decreasing Graphics of Frame Systems with Infill Wall Length/ Infill Wall Height (l/h=1/2)

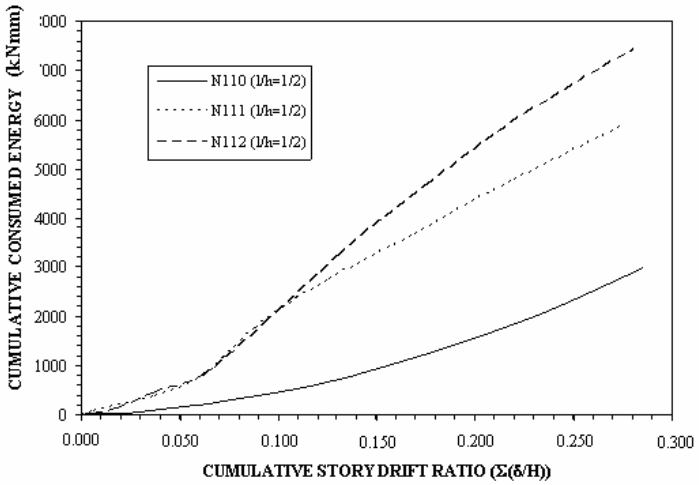

Figure 12. Cumulative Consumed Energy Graphics of Frame Systems with Infill Wall Length/Infill Wall Height (l/h=1/2)

4.2 The Effect of Infill Wall Characteristic on the Behavior of the Frame Systems

4.2.1 Empty frame systems

The results belonging to three tested empty frames with various dimensions are examined in this section. The related test specimens are N110 (l/h=1), N110 (l/h=2), N110 (l/h=1/2) frame systems of single story-single span and length/height ratios are respectively 1, 2, and ½. These specimens' strength envelopes are given in Figure 13.

As seen from Figure 13, the carried maximum horizontal load values were 32.37 kN, 27.15 kN, and 12.97 kN, respectively. The l/h = 2 frame system carries a 84% ratio and the l/h = ½ frame system carries a 40% ratio of the reference l/h=1 frame system's horizontal load.
The rigidity decline graphics determined from the aforementioned specimen tests are given in Figure 14. While the first cycle rigidity values were 1.17 kN/mm, 1.21 kN/mm, and 0.38 kN/mm, respectively, the rigidities decreased in the subsequent cycles. Considering the first cycle rigidities determined from the first cycle, the l/h=2 frame system had a 103% ratio and the l/h= ½ frame system has a 61% ratio of the l/h=1 frame system's starting rigidity value.

The first cycle rigidities decreased rapidly in the progressive cycles, in which the l/h=1 and l/h=2 frame systems had a value of 0.40 kN/mm in the eighth cycle, and the l/h= ½ frame system had a value of 0.15 kN/mm in the ninth cycle.

The cumulative consumed energy graphics obtained from the tests of the mentioned specimens are also given in Figure 15. It indicates that the cumulative consumed energy values are 10878 kNmm and 13237 kNmm for the (l/h=1) and (l/h=2) frame systems, respectively, at the end of the eighth cycle and 2991 kNmm for the (l/h= ½) frame system at the end of the ninth cycle.

In terms of consumed energy, the l/h=2 frame system consumed 22% more energy than the l/h=1 frame system. Again (at the level of δ/H=0.0277), the l/h= ½ frame system consumed 63% of the energy of the l/h=1 frame system

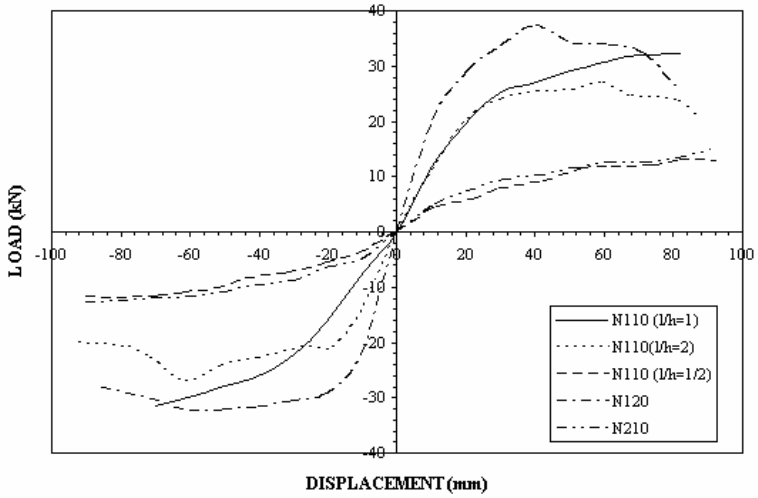

Figure 13. Strength Envelopes of Frame Systems with No Infill Wall

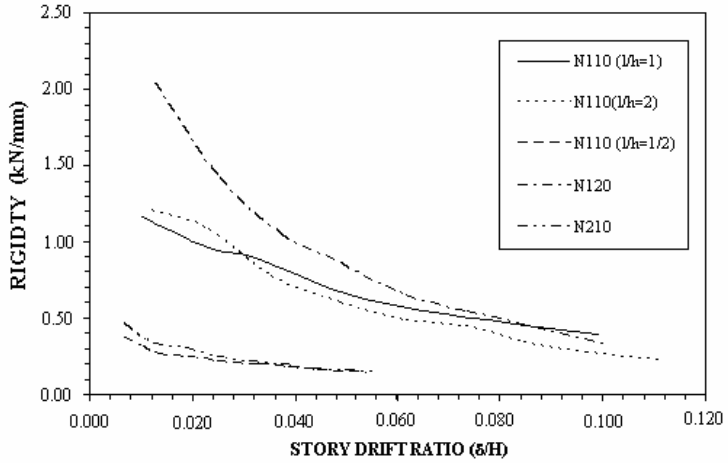

Figure 14. Rigidity Decreasing Graphics of Frame Systems with No Infill Wall

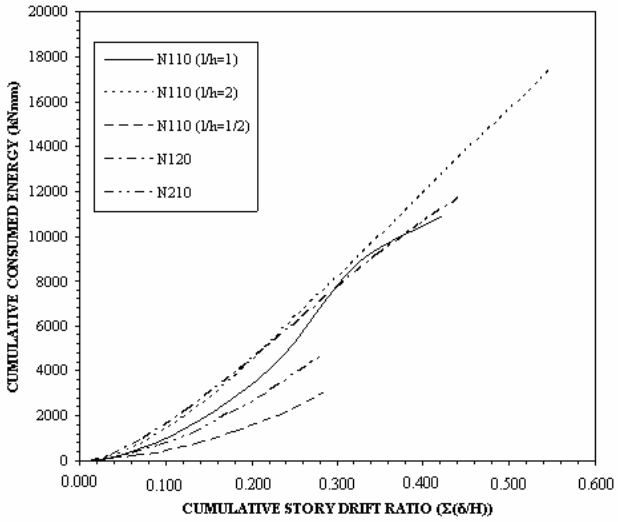

Figure 15. Cumulative Consumed Energy Graphics of Frame Systems with No Infill Wall

4.2.2 Brick wall infilled frame systems

The results of three tested brick wall infilled frame systems with various dimensions are investigated in this study. These test specimens were brick wall infilled frame systems with dimensions of (l/h=1), (l/h=2) and (l/h= ½). Their strength envelopes are given in Figure 16.
As seen from Figure 16, the carried maximum horizontal loads were found as 41.42 kN, 45.40 kN, and 23.64 kN, respectively. When the reference empty frame was considered as a base, the increase in the carried horizontal load was 82% for the brick wall infilled system and 121% for the brick wall+plaster infilled system. The l/h=2 frame system carries 110% and the l/h= ½ frame system carries 57% of the horizontal load of the reference l/h=1 frame system.

The rigidity decline graphics obtained from the aforementioned specimen tests are given in Figure 17. While the first cycle rigidity values were 2.55 kN/mm, 3.83 kN/mm, and 1.05 kN/mm (N112), respectively, the rigidities decreased in the subsequent cycles. While the rigidity decrease was more rapid in the (l/h=1) and (l/h=2) specimens, it was slower in other specimens. Considering the first cycle rigidities determined from the first cycle, the l/h=2 frame system has 150% and the l/h= ½ frame system has 41% of the starting rigidity value of the l/h= 1 reference frame system. First cycle rigidities rapidly decreased in progressive cycles in which the 0.30 kN/mm value was reached in the single story-single span l/h=1 and l/h=2 frame systems in the eighth cycle, and 0.15 kN/mm in the l/h= ½ frame system in the ninth cycle.

The cumulative consumed energy graphics obtained from these specimens' tests are also presented in Figure 18. It indicates that the cumulative consumed energy values after the eighth cycle were 14877 kNmm and 17406 kNmm, respectively for the (l/h=1) and (l/h=2) frame systems, and 5871 kNmm after the ninth cycle for the (l/h= ½) frame system.

In terms of consumed energy, the l/h=2 frame system consumed 17% more energy than the l/h=1 frame system. Again (at level of δ/H=0.0277), the l/h= ½ frame system consumed 70% of the energy of the l/h=1 frame system.

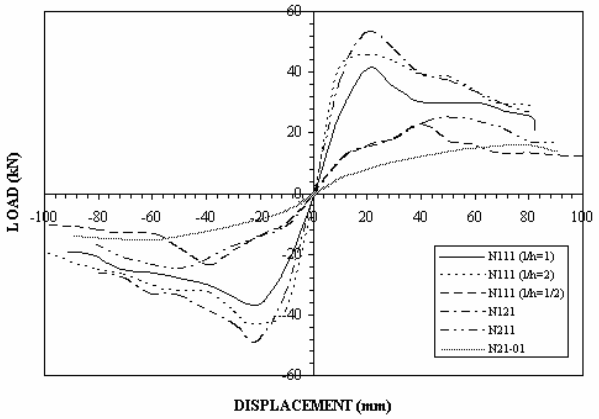

Figure 16. Strength Envelopes of Frame Systems with Infill Brick Wall

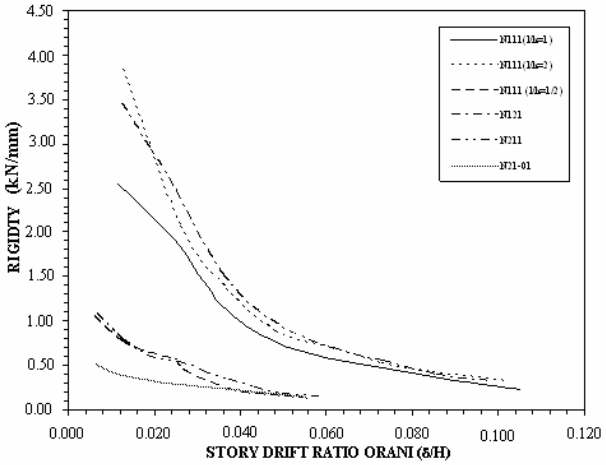

Figure 17. Rigidity Decreasing Graphics of Frame Systems with Infill Brick Wall

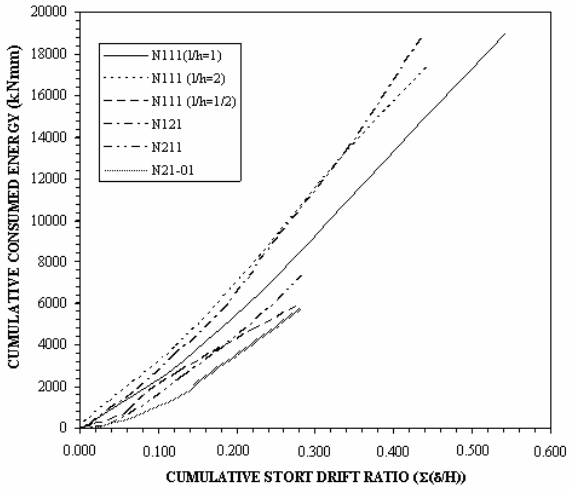

Figure 18. Cumulative Consumed Energy Graphics of Frame Systems with Infill Brick Wall

4.2.3 Brick wall+plaster infilled frame systems

The results of three brick wall+plaster infilled frame systems tested in this study and with various dimensions are investigated in this section. The test specimens are the brick wall+plaster infilled frame systems with dimensions of (l/h=1), (l/h=2), and (l/h= ½). The strength envelopes of these specimens are given in Figure 19. The carried maximum horizontal loads were found as 56.92 kN, 65.86 kN, and 28.60 kN, respectively. The l/h=2 frame system carried 116%, and the l/h= ½ frame system carried 50% of the horizontal load of the l/h=1 reference frame system.

The rigidity decline graphics obtained from the specimen tests are given in Figure 20. While the first cycle rigidity values were 3.06 kN/mm, 4.19 kN/mm, and 1.18 kN/mm, respectively, the rigidities decreased in the subsequent cycles. Considering the first cycle rigidities determined from the first cycle, the l/h=2 frame system has 136%, and the l/h= ½ frame system has 39% of the starting rigidity value of the l/h= 1 reference frame system. First cycle rigidities rapidly decreased in progressive cycles in which the 0.15-0.45 kN/mm interval was obtained for the l/h=1 and l/h=2 frame systems in the eighth cycle and a value of 0.18 kN/mm was obtained for the l/h= ½ frame system in the ninth cycle.
The cumulative consumed energy graphics obtained from these specimens' tests are given in Figure 21. Examining Figure 24, the cumulative consumed energy values after the eighth cycle are 17978 kNmm and 17886 kNmm, respectively, for the (l/h=1) and (l/h=2) frame systems, and 7429 kNmm after the ninth cycle for the (l/h= ½) frame system.

In terms of consumed energy, the l/h=2 frame system consumed 14% less energy than the l/h=1 frame system. Again (at level of δ/H=0.0277), the l/h= ½ frame system consumed 70% of the energy of the l/h=1 frame system. The obtained test results are given in Table 2.

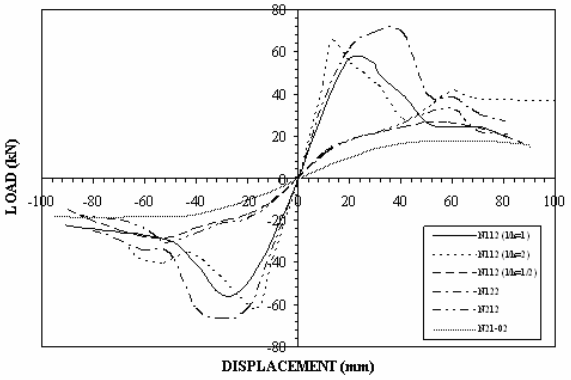

Figure 19. Strength Envelopes of Frame Systems with Brick Wall+Plaster Infilled Wall

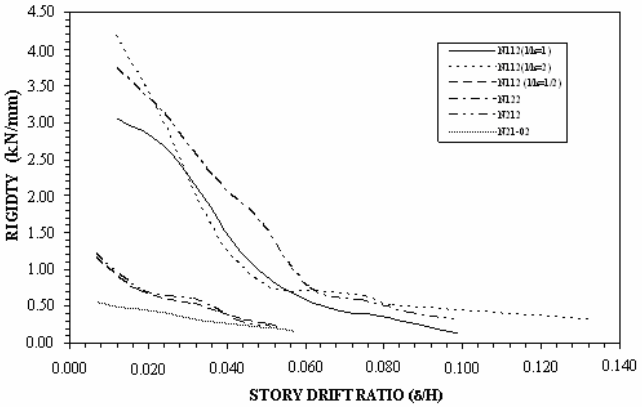

Figure 20. Rigidity Decreasing Graphics of Frame Systems with Brick Wall+ Plaster Infilled Wall

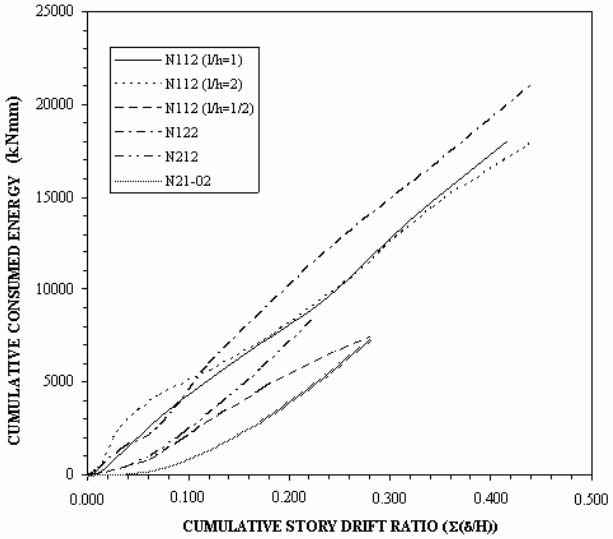

Figure 21. Cumulative Consumed Energy Graphics of Frame Systems with Brick Wall+Plaster Infilled Wall

Table 8. Tabulation of Experimental Results

Specimens	Experimental Maximum Lateral Load		Initial Rigidity (kN/mm)	Ultimate Rigidity		Energy Consumed at the End of the Test		Failure Type*
	Load (kN)	(δ/H)		Rigidity (kN/mm)	(δ/H)	Cumulative Consumed Energy (kNmm)	Cumul. Σ(δ/H)	
(1)	*(2)*	*(3)*	*(4)*	*(5)*	*(6)*	*(7)*	*(8)*	*(9)*
N110	32.37	0.099	1.46	0.40	0.0994	10878	0.422	SFF
N111	41.42	0.024	10.75	0.23	0.1108	14877	0.437	OTC
N112	56.92	0.0247	19.30	0.15	0.0986	17978	0.416	OTC
N110	27.15	0.072	1.28	0.23	0.1115	13237	0.435	SFF
N111 (l/h=2)	45.50	0.0241	13.20	0.33	0.1019	17406	0.437	OTC-CC
N112 (l/h=2)	63.23	0.0243	25.80	0.33	0.1323	17886	0.439	CC
N110	12.97	0.051	0.46	0.14	0.0538	2991	0.285	---
N111 (l/h=1/2)	23.64	0.0244	3.72	0.13	0.0560	5871	0.275	OTC-CC
N112 (l/h=1/2)	28.60	0.0322	6.10	0.17	0.0552	7429	0.281	OTC-CC

*(CC) denotes failure with compression crush, (OTC) failure with oblique tensional crack and (SFF) steel frame failure.

5. DISCUSSION OF RESULTS AND CONCLUSION

The results obtained by the experimental study are given in the following;

1. The lateral stiffness, lateral load-bearing, and energy consumption capacities of the steel frame under lateral loading considerably increased with the aid of the infill walls of various structural characteristics.
   - Depending on the L/h ratio, the unplastered and plastered infill walls increased the lateral load-bearing capacity of empty steel frames by 28% - 82% and 76% - 142% proportions, respectively.
   - Depending on the L/h ratio, the unplastered and plastered infill walls increase the initial stiffness values of empty steel frames by 118% - 216% and 160% - 246% proportions, respectively.
   - Similarly, again depending on the L/h ratio, the unplastered and plastered infill walls increase the cumulative consumed energy values of empty steel frames by 31% - 96% and 35% - 148% proportions, respectively.

2. The horizontal stiffness, lateral load-bearing, and energy consumption capacities of the frame systems are considerably affected due to the varying infill wall length/height (l/h) ratio.

3. The lateral load-bearing capacity increases when the infill wall length/height (l/h) ratio is greater than 1 and considerably decreases when (l/h) < 1.

4. As seen from the tests, the plaster application on brick walls considerably increases the lateral stiffness, energy consumption, and horizontal failure load characteristics of the infilled frame systems. Therefore, the plastering process should be absolutely required for practical applications.

REFERENCES

[1] Dawe, J.L. and Seah, C.K., “Behaviour of Masonry Infilled Steel Frames”, Can. J. Civ. Eng. 1989, Vol. 16, No. 6, pp. 856-876.

[2] Dukuze, et al., “Assessment of Diagonal and Racking Loading of RC Infilled Frames”, Proceedings of the 8th Canadian Masonry Symposium, Jasper, Alberta 1998, June, pp. 385-397.

[3] Flangan, R.D., et al., “Experimental Testing of Hollow Clay Tile Infilled Frames”, Proc. 6th Can. Masonry Symp., Univ of Saskatchewan, Canada, 1992, pp. 633-644.

[4] Hakam, Z.H.R., “Retrofit of Hollow Concrete Masonry Infilled Steel Frames using Glass Fiber Reinforced Plastic Laminates”, Ph.D. Thesis, Drexel University, 2000.

[5] Holmes, M., “Steel Frames with Brickwork and Concrete Infilling”, Proc. Inst. Civ. Engrs., 1961, Vol. 19, No. 6501, pp. 473-478.

[6] Kaltakcı, M.Y. and Koken, A., “An Experimental and Theoretical Study On The Behavior Of Infilled Steel Frames Under Reversed-Cycling Loading”, Research Project, Selcuk University, BAP, Konya, Turkey, 2003.

[7] Kaltakcı, M.Y. and Koken, A., “Cyclic Behaviour of Infilled Steel Frames”, Tubitak Project Number: Intag569, Ankara, Turkey, 2003.

[8] Köken, A., “Cyclic Behaviour of Infilled Steel Frames With Multi Storey and Multibay a Theoretical and Experimental Investigation”, PhD Thesis, Selcuk University, Natural and Applied Sci. Inst., Konya, Turkey, 2003.

[9] Mehrabi, A.B., et al., "Experimental Evaluation of Masonry Infilled RC Frames", Journal of Structural Engineering, ASCE, 1996; Vol. 122, No.3, March pp. 228-237.

[10] Mainstone, R.J. and Weeks, G.A., "The Influence of Bounding Frame on the Racking Stiffness and Strength of Brickwalls", Proc. 2nd Int Brick Masonry Conf., Stoke on Trent England, 1970, pp. 165-171.

[11] Mander, A.B., et al., "An Experimental Study on the Seismic Performance of Brick Infilled Steel Frames with and Without Retrofit", Rep. NCEER-93-0001, State Univ. of New York at Buffalo. N.Y., 1993.

[12] Moghaddam, et al., "The State of Art in Infilled Frames", ESEE Research Report No. 87-2, Civil Engineering Department, Imperial Collage of Science and Technology; August 1987.

[13] Stafford, S., "Lateral Stiffness of Infilled Frames", J. Struc. Div. ASCE, 1962, Vol. 88, No. 6, pp. 183-199.

[14] Stafford, S., "Behaviour of the Square Infilled Frames", J. Struc. Div. ASCE, 1966, Vol. 92, No. 1, pp. 381-403.

ISOLATING CORROSION OF STEEL PLATES COUPLED WITH TITANIUM

A. Patnaik[1,*], X. Shan[4], M. Adams[1], T. S. Srivatsan[2], C.C. Menzemer[1] and J. Payer[3]

[1] *Department of Civil Engineering*
[2] *Department of Mechanical Engineering*
[3] *NCERCAMP, The University of Akron, Akron, OH 44325, USA*
[4]*Research and Engineering Center, Whirlpool, Benton Harbor, MI, USA*
**(Corresponding author: E-mail:* Patnaik*@uakron.edu)*

Received: 15 November 2012; Revised: 27 January 2013; Accepted: 14 February 2013

ABSTRACT: Over twenty six percent of the bridges in the United States are structurally deficient or functionally obsolete. Corrosion of steel used in structures like bridges and buildings is a problem that has gained increased interest and focused concern. Steel is often the metal that is preferred for use in such applications due to a synergism of ease of availability, acceptable mechanical properties and cost effectiveness. Through the years, titanium has grown in strength, stature and significance to be recognized as an emerging high performance metal that is both stronger and lighter than steel. A distinctive property of titanium and its alloys is its non-corrosive nature. However, a major drawback in the selection and use of pure titanium or its alloy counterpart is the prohibitively high cost. Therefore, it may be possible to combine steel and pure titanium and/or its alloy in structures by restricting steel for bulk of the structure and selectively using titanium and its alloys for the critical but low volume elements, such as, gusset plates and bearings. A hybrid use of titanium in conjunction with steel for structural members will result in better performance while concurrently proving to be both cost-effective and economically affordable. The synergistic use of structural steel and titanium in close proximity with each other could result in accelerated corrosion of steel in the immediate vicinity of titanium. The corrosion performance of titanium plates coupled with steel members is presented. A few viable strategies for minimizing galvanic coupling effects between steel and titanium are discussed. Corrosion experiments were conducted to measure the severity of corrosion when titanium and steel form a galvanic couple, and copper and steel was a comparative system. The study revealed that adequate precautions are needed to minimize localized corrosion when titanium gusset plates are coupled with structural steel members.

Keywords: Structural members, steel, joining, gusset plate, titanium, environment, exposure, corrosion

1. INTRODUCTION

The annual highway bridge inventory (e.g., ASCE Report Card [1]) has time and again revealed that more than 20 percent of bridges in the United States are structurally deficient or functionally obsolete due to deterioration related to aging. The poor health of the infrastructure can be devastating both in terms of human toll and economic impact. Failures can be minimized or obviated through a judicious combination of appropriate choice of materials and adoption of novel and innovative structural design. A gradual loss of cross-sectional properties due to corrosion of structural steel members or connections is a well known phenomenon that has for long been documented (Figure 1). However, steel continues to be the most preferred, widely chosen and used material for cost-sensitive structures primarily because of its ease of availability, affordability, acceptable mechanical properties, familiarity, and technology readiness.

In highway bridges, the key elements that exert a noticeable influence on effective functioning of the structure are the joints between different members. Joints are often made from an assemblage of plates. Examples of connection elements or ”gusset plates” that serve to connect the ends of truss members involved using structural fasteners are shown in Figure 2. Fasteners used in newer structures are mostly bolts; and rivets were mostly used in the older structures. Failure of the joints in a bridge truss due to a gradual loss of strength as a direct consequence of environmental

degradation or corrosion can be devastating. This necessitates the need to improve the performance of gusset plates through an observable reduction of corrosion-related deterioration coupled with a concurrent increase in structural strength. Furthermore, failure of the joints, or connections, is often rapid and brittle, and the consequences can be catastrophic when compared to failure of the structural member.

Figure 1. Corrosion Affected Elements of a Steel Bridge

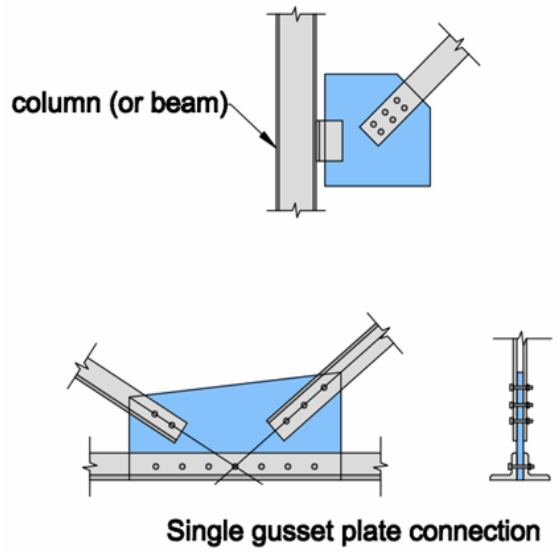

Figure 2. Schematic Showing Configuration of Two Typical Gusset Plates

In the last three decades, i.e., since the early 1980s, titanium has progressively gained increased importance based on both need and significance. This culminated in the titanium metal and its alloy counterparts being recognized as modern high performance metals that are both stronger and lighter than many of the most widely chosen and preferentially used steels in the industry. The applications span a spectrum of both load-bearing and even non load-bearing applications. Another attractive property of pure titanium metal and its alloy counterparts is its non-corrosive nature. A recent study on built-up welded beams made from both pure titanium metal and a titanium alloy demonstrated the potential for viable use of welded structures for both the defense-related and civilian applications [2-5].

On account of its light weight, excellent corrosion resistance, high strength, attractive fracture behavior coupled with high melting point, titanium is often chosen and used in a spectrum of industries dealing with both performance-critical and non-performance critical components and has gradually grown to become one of the most important non-ferrous metals for load-bearing applications. At temperatures below 300^{o}C, alloys of titanium present good formability coupled with high mechanical strength. One such alloy is Ti-6Al-4V. This alloy is often chosen and used primarily because of its excellent tensile strength and fatigue strength, adequate ductility, acceptable fracture toughness and overall good resistance to corrosion. Despite its superior structural performance and corrosion resistance, it is not cost effective to use pure titanium metal and its alloys for large structures, such as bridges. However, it may be possible to use structural steel for the main members of a large structure in combination with pure titanium metal or its alloy counterpart for the critical but low volume locations, such as: (i) connections, (ii) bearings, and (iii) similar elements.

The likelihood of failure of a gusset plate and the concomitant collapse of a bridge may be minimized if the gusset plates are made from non-corrosive and high strength pure titanium metal or its alloy counter part. The use of titanium for the entire bridge structure is not practical at this time. However, it is feasible to provide titanium gusset plates in a bridge structure primarily because of the small tonnage of the gusset plates relative to the entire structure. This implies that the main members are made from the routinely used structural steel, but the connections are made from either pure titanium or its alloy counterpart. The structural performance of gusset plates made from pure titanium metal and its alloy counter part has been the subject of a recent study, which demonstrated titanium gusset plates to be both structurally sound and an economically viable alternative to the use of steel gusset plates [6-8].

The proposed solution will necessitate the need for a synergistic use of structural steel and titanium in close proximity to each other. Use of these two metals could lead to potential galvanic effect that serves to exacerbate conditions that are conducive for the corrosion of steel. Such a problem can be overcome by isolating the parts from each other either through the prudent use of coatings or a physical barrier, i.e., a transition piece. This kind of mixing coupled with the use of a transition piece will invariably necessitate the need to use fasteners (structural bolts). The use of bolted non-corrosive high strength titanium gusset plates in highway bridges can be a potentially viable solution to minimize gusset plate failures that can occur either due to corrosion related deterioration, or inadequate strength.

The primary objective of this study was to investigate viable and prudent alternatives for isolating pure titanium metal and its alloy counterpart along with the steel parts so as to minimize or even prevent the occurrence of accelerated galvanic corrosion of steel. The specific objective of this study was to evaluate and concurrently establish a viable method to isolate titanium gusset plates from the surrounding steel elements in a connection in order to prevent the triggering of accelerated galvanic corrosion, while concurrently assessing the effects of coupling two dissimilar metals, i.e., steel and titanium. Despite high cost, the corrosion resistance of pure titanium and its alloys is an important consideration in its selection as an economical and viable structural material with acceptable mechanical properties. Titanium provides excellent corrosion resistance in a range of environments under varying degree of aggressiveness due to the stable, protective and adherent titanium di-oxide film that forms instantly when a fresh surface of the metal is exposed to a moisture-containing environment, be it aqueous or gaseous [9, 10]. Titanium is preferred due to its immunity to “MIC” (Microbiologically Influenced Corrosion). At temperatures below 180^{o}F (82^{o}C), the occurrence of both crevice corrosion and pitting corrosion are mostly non-existent [10]. Furthermore, the pure metal and its alloy counterparts are immune to stress corrosion cracking (SCC) for bridge exposure conditions, and the strength loss due to corrosion fatigue resistance is

minimal. The adherent titanium dioxide film that forms on the surface acts as an excellent barrier to the ingress of hydrogen gas. However, when titanium is coupled with other metals, there occur conditions that are “locally” conducive for the initiation of galvanic corrosion. Due to the nobility of titanium in the galvanic series, the logic of coupling titanium with other dissimilar metals will only tend to accelerate corrosion of the other metal in the couple.

Dissimilar metal joints of titanium and steel with parts in intimate contact and susceptible to galvanic corrosion were investigated in this study. For the case of a steel structure in close proximity to titanium, steel would be anodic and more active (corrosion prone) when compared to titanium. Electrical isolation of the two metals is a means to eliminate galvanic corrosion and to ensure that no accelerated corrosion of steel is due to the titanium. A careful review of the published literature was conducted and is used to identify the corrosion data for steel and titanium joints while concurrently providing useful information related to viable techniques for isolation. In general, isolation of two dissimilar metals may be accomplished by using: (i) several coats of a zinc-rich primer, (ii) bituminous paint, and in some instances (iii) a high performance isolation tape. The structural performance of a primer, paint or tape is up until now untested and is susceptible to both wear and tear.

The effects of aggressive environmental conditions on (a) titanium, and (b) dissimilar metal combinations with pure titanium or its alloy counterpart as one of the metals in a joint can generally be categorized into two types [9-23]:

(a) Galvanic Corrosion
(b) Hydrogen-Induced Damage

These two topics are briefly reviewed in this paper. A brief discussion is included on aspects pertinent to the crevice corrosion experienced by dissimilar metals. An experimental evaluation of mixed-mode use of titanium in synergy with steel is presented and briefly discussed. Copper/steel galavanic action was included as a comparative system, since copper has a well known and strong galvanic action on steel. The results of galvanic corrosion tests are included along with the precautions that need to be taken in order to either prevent or minimize problems due to corrosion related to coupling of pure titanium and/or its alloys with structural grade steel.

2. GALVANIC CORROSION

In the case of a steel structure using titanium gusset plates, steel would be expected to be anodic (more active and corrosion prone) when compared to titanium. Therefore, isolation of the two metals may be necessary in order to ensure adequate long-term performance of the structure that contains titanium gusset plates while remaining sections of the structure are made from structural steel. A brief review of the existing literature is presented in this section to identify existing corrosion data specific to steel and titanium joints and the potential use of possible isolation techniques [12-22, 24].

Galvanic corrosion happens due to the different electric potentials exhibited by dissimilar metals. When these metals are placed in contact with each other, in the presence of an electrolyte, a galvanic couple is formed due to a tendency of the electrons to flow from the more negative metal (anode) to the more positive (cathode) of the two metals. This is an important aspect to be taken into consideration when attempting to join titanium to another metal because titanium is essentially cathodic relative to a large majority of the other metals it is likely to come in contact with. If proper steps to account for and minimize galvanic corrosion are not taken, both the integrity and useful life of the structure are likely to be compromised.

If the area of titanium (cathode) is noticeably large relative to that of the other metal, severe galvanic corrosion will occur. If the need for dissimilar joints is inevitable, it is best to: (i) use two metals that are close to each other in the galvanic series, (ii) insulate the joint, and (iii) provide cathodic protection. Use of large areas of the less noble metal coupled with heavy sections to allow for reduced corrosion has also been recommended [24]. However, such approaches tend to defeat the very purpose of using titanium gusset plates.

An important consideration with specific reference to the severity of galvanic corrosion is physical separation between the two metals in the galvanic table. A typical galvanic series is summarized in Table 1 for metals in sea water from US Army Missile Command Report RS-TR-67-11, "Practical Galvanic Series" [24]. The table related to the galvanic data provides useful guidance with respect to selecting metals to be joined, such that metals having a minimal tendency to interact galvanically can be coupled with minimal galvanic effects. Alternatively, the table also provides useful information on both the need and degree of protection required to minimize the anticipated galvanic interactions. The closer a metal is to another in the galvanic series, the more compatible will be the two metals with concomitant minimum galvanic interaction. Conversely, the farther one metal is from the other then greater will be the tendency for the occurrence of galvanic corrosion. The influence of joining dissimilar metals with one of the metals being titanium is provided in a TIMET report on corrosion resistance of metals [9]. In this report, it is shown that an increase in corrosion in mils per year (or mm per year) due to coupling with the listed metals can be different by an order of magnitude. In fact, coupling of titanium with low carbon steel was found to be the worst case for facilitating ease of environmental degradation or corrosion.

Table 1. Galvanic Table from MIL-STD-889 [Reference 24]

Active (Anodic)	**Active (Anodic)**	**Active (Anodic)**	**Active (Anodic)**
1. Magnesium	24. Al 2014-0	47. Uranium 8% Mo.	70. Silicone Bronze 655
2. Mg alloy AZ-31B	25. Al 2024-T4	48. Brass, Naval, 464	71. Stainless steel 304 (passive)
3. Mg alloy HK-31A	26. Al 5052-H16	49. Yellow Brass	72. Stainless steel 301 (passive)
4. Zinc (hot-dip, die cast, or plated)	27. Tin (plated)	50. Muntz Metal 280	73. Stainless steel 321 (passive)
5. Beryllium (hot pressed)	28. Stainless steel 430 (active)	51. Brass (plated)	74. Stainless steel 201 (passive)
6. Al 7072 clad on 7075	29. Lead	52. Nickel-silver (18% Ni)	75. Stainless steel 286 (passive)
7. Al 2014-T3	30. Steel 1010	53. Stainless steel 316L (active)	76. Stainless steel 316L (passive)
8. Al 1160-H14	31. Iron (cast)	54. Bronze 220	77. AM355 (active)
9. Al 7079-T6	32. Stainless steel 410 (active)	55. Copper 110	78. Stainless steel 202 (passive)
10. Cadmium (plated)	33. Copper (plated, cast, or wrought)	56. Red Brass	79. Carpenter 20 (passive)
11. Uranium	34. Nickel (plated)	57. Stainless steel 347 (active)	80. AM355 (passive)
12. Al 218 (die cast)	35. Chromium (Plated)	58. Molybdenum, Commercial pure	81. A286 (passive)
13. Al 5052-0	36. Tantalum	59. Copper-nickel 715	82. Titanium 5A1, 2.5 Sn
14. Al 5052-H12	37. AM350 (active)	60. Admiralty brass	83. Titanium 13V, 11Cr, 3Al (annealed)
15. Al 5456-0, H353	38. Stainless steel 310 (active)	61. Stainless steel 202 (active)	84. Titanium 6Al, 4V (solution treated and aged)
16. Al 5052-H32	39. Stainless steel 301 (active)	62. Bronze, Phosphor 534 (B-1)	85. Titanium 6Al, 4V (anneal)
17. Al 1100-0	40. Stainless steel 304 (active)	63. Monel 400	86. Titanium 8Mn
18. Al 3003-H25	41. Stainless steel 430 (active)	64. Stainless steel 201 (active)	87. Titanium 13V, 11Cr 3Al (solution heat treated and aged)
19. Al 6061-T6	42. Stainless steel 410 (active)	65. Carpenter 20 (active)	88. Titanium 75A
20. Al A360 (die cast)	43. Stainless steel 17-7PH (active)	66. Stainless steel 321 (active)	89. AM350 (passive)
21. Al 7075-T6	44. Tungsten	67. Stainless steel 316 (active)	90. Silver
22. Al 6061-0	45. Niobium (columbium) 1% Zr	68. Stainless steel 309 (active)	91. Gold
23. Indium	46. Brass, Yellow, 268	69. Stainless steel 17-7PH (passive)	92. Graphite
		70. Silicone Bronze 655	
End - Noble (Less Active, Cathodic)			

The Galvanic Table (Table 1) lists metals in the order of their relative activity when exposed to seawater environment. The list begins with the more active (anodic) metal and proceeds down to the least active (cathodic) metal of the galvanic series [24]. The galvanic series in the table applies to an electrolyte solution that is representative of seawater. The series will however be different for other types of solutions.

Another important consideration for the galvanic effect is kinetic factors. Table 1 shows the tendency of possible galvanic effects thermodynamically. The galvanic effect also depends on reaction kinetics of both the anode and the cathode. For example, the potential difference between stainless steel and aluminum is larger than that of carbon steel and aluminum. However, a stronger galvanic effect is found to exist between carbon steel and aluminum couple. [25].

The environment to which the metals will be exposed is also an important consideration. Stainless steel and aluminum are far apart in the galvanic series, and the potential difference is on the order of 650 mV. However, for applications in ambient temperature (298 K) and laboratory air (Relative Humidity of 55 pct), the occurrence of galvanic corrosion is unusual [26]. For galvanic corrosion to occur, it is essential for the following three conditions to exist:

(i) Metals of dissimilar electric potentials must be present.
(ii) There must be an electrically conductive path between the two metals.
(iii) Both metals must be in contact with a continuous electrolyte.

When the two metals are in direct contact with each other, there is a tendency for the electrons to flow from the anodic metal to the cathodic metal. A progressive loss of electrons from the anodic metal causes the release of positive ions into the electrolytic solution, thereby corroding the anode. The additional electrons that are gained by the cathodic metal are consumed by an electrochemical reduction reaction. Two of the most common reactions that are favored to consume electrons at the cathode are the following:

(i) In acidic solutions, the reduction of hydrogen:

$$2H^{+} + 2e^{-} \xrightarrow{\text{yields}} H_2(\text{gas})$$

(ii) In neutral or alkaline solutions, the reduction of oxygen:

$$2H_2O + 4e^{-} + 4e^{-} + O_2 \xrightarrow{\text{yields}} 4OH^{-}$$

The rate at which galvanic corrosion occurs is often influenced by several concurrent and mutually competing factors to include the following [27]:

(a) Location of the two metals in the galvanic series and the electrolytic medium to which they are being exposed to.
(b) The relative surface areas of the two metals in use.
(c) Both the nature and kinetics of reactions occurring on the surfaces of the two chosen metals.
(d) The nature and conductivity of the electrolyte.

Galvanic corrosion is not easily favored to occur if any one of these conditions does not exist. By eliminating any one or combination of these conditions, the electric circuit is broken and the electrochemical reactions responsible for galvanic corrosion cannot easily proceed. The most effective steps taken to prevent galvanic corrosion are often those taken during the design of the structure [27].

3. PREVENTION OF GALVANIC CORROSION ON A STEEL/TITANIUM COUPLE: A FEW OPTIONS

It is preferred to avoid the selection of multiple metals during the design process. Selecting metals that have minimal difference in galvanic potential plays a key role in minimizing corrosion related problems. In situations where this is not possible, it is important to minimize the ratio of exposed surface area of the cathode to the anode. Copper/steel galvanic action is a classic case to demonstrate this. Steel bolts (more active) in a copper plate are subject to intense galvanic action, i.e., large cathode (copper) and small anode (steel). Whereas, copper bolts in a steel plate, while not desirable, have a lesser detrimental galvanic effect on steel because the anode has a larger surface area than the cathode.

Electrically insulating the anode from the cathode is another effective method to break the galvanic circuit and concurrently prevent the occurrence of galvanic corrosion. This is often achieved through the selective use of both non-conductive spacers and sleeves for situations where corrosion of the bolts is of concern. In many practical situations, use of this method of prevention may not be feasible since a large mechanical stress has to be either transferred or sustained across the two metals, and this will tend to damage the weaker material of the insulator.

Prevention of galvanic corrosion can also be achieved by exercising care to isolate the metal junction from the environment containing the electrolyte. Frequently this is made possible by applying a moisture resistant paint or moisture displacing grease on the surfaces both at and immediately surrounding the junction, thus keeping it free of contact with the electrolyte [28]. The effectiveness of this method is dependent on both the maintenance and upkeep of the coatings. Minor imperfections in the paint system can lead to a progressive intensification of corrosion that occurs “locally”, such as an imperfection, resulting in initiation and rapid progression of degradation of the protective coating.

One other attractive method that has been used to reduce galvanic corrosion on a certain metal is to take advantage of the nature of galvanic corrosion and to introduce a third metal that is more anodic into the galvanic circuit. When this is done, the third metal will selectively corrode, sparing the other two cathodic metals from environmental attack and concomitant degradation. For example, in marine environments for immersed structures, zinc anodes are used to offset the detrimental galvanic action on steel by copper alloys. The zinc, being more anodic than the other metals used in the structure behaves in a sacrificial manner, thereby preventing the occurrence of corrosion of the other two metals. If the zinc anodes are continuously replaced, then the other metals used in the structure will be spared from environmental attack and resultant degradation through corrosion.

The key determinant in the conjoint use of steel and titanium (be it pure or alloy counterpart) is the presence of moisture. The initiation and occurrence of galvanic corrosion can be minimized if moisture can be prevented from entering the metal joints. One effective and commonly used method to prevent the penetration of moisture into a gusset plate joint is to seal the joint using a suitable polymer or any other commercially available sealant subsequent to installation of the bolts. Also, for the purpose of minimizing corrosion, it is essential to avoid having a small area of the anode relative to the area of the cathode. A few other methods of protection exist and are available in the published literature. For example, Erb [24] provided a number of viable recommendations to minimize both the initiation and progress of galvanic corrosion. A few of his essential recommendations are:

1. Sacrificial–Apply a sacrificial coating having a potential similar to or near that of the anodic member to the cathodic member.

2. Sealing –Make the surfaces essentially impervious to water by sealing.
3. Resistance - Increase the resistance of the electrical circuit by either painting or coating of all the surfaces.
4. To use a large area for the anode, this will reduce the galvanic current density on the anode resulting in lowering the level of attack.
5. To design an overall small ratio of cathode-to-anode.

In seawater environment, all exposed edges must be sealed, and an interposing material that is compatible with both the anode and the cathode must be used as the non-compatible material. If allowable, an external joint can be coated on its exterior surface using an effective paint system. It is advisable to utilize as many corrosion protection techniques as possible, since the intrinsic effects of each protection technique would provide substantially better protection when compared to the use of any one technique.

Special consideration must be given to both the material and protection of bolts in a dissimilar material couple, as they are easily susceptible to corrosion and often of critical importance to the overall integrity of the connection. If the bolts are made of mild steel, they are exposed to the possibility of intense corrosion and resultant degradation essentially due to the relatively high surface area ratio of titanium to steel present in a bolted connection. Ideally, the bolts in such a situation would be made of the cathodic metal, which in this case is titanium. Another, more feasible recommendation would be to use stainless steel or galvanized bolts for this application. The galvanic behavior of stainless steel is quite similar to that of titanium so as to minimize both the initiation and occurrence of galvanic corrosion under normal operating temperatures. Galvanized steel provides a sacrificial coating of zinc on steel bolts, which will tend to preserve the underlying metal for a fixed time period until the zinc gradually corrodes away.

Substantial additional protection can also be provided using a coating of paint having low moisture/oxygen permeability. This would tend to effectively isolate the joint of the two metals from the electrolyte (even ambient air qualifies as an electrolyte once the humidity reaches a certain level), and thereby minimize the effects of galvanic corrosion. Periodic inspection coupled with maintenance of the paint would be both essential and necessary to prevent spot degradation, as this leads to intensified corrosion of the steel that is exposed at these locations. The type of paint to be used and its composition will vary based on: (i) nature of the environment to which the metal will be exposed, and (ii) performance expected from the coating .Often these requirements are unique to a specific project and the application of a coating is often dictated on a case-by-case basis.

4. HYDROGEN CRACKING IN TITANIUM-BASED ALLOYS

In most situations, titanium can be safely chosen and used without any problems in hydrogen-containing environments and under conditions where galvanic couples or cathodic protection systems favor exposure of the metal surface to gaseous hydrogen. However, there have been a few failures linked to hydrogen embrittlement caused by the formation and presence of hydrides. In most cases, the oxide film which covers the surface of titanium provides an effective barrier to the penetration of hydrogen. However, titanium has the tendency to easily absorb hydrogen from hydrogen-containing environments under some circumstances [9].

At temperatures below 170°F (77°C), the formation of hydrides tends to occur slowly and has minimal to no practical significance except in conjunction with a high tensile stress. In the presence of trace amounts (about 2%) of moisture in the hydrogen gas, passivation of the titanium metal is favored to occur such that absorption of hydrogen is prevented even at high pressures and

temperatures. A serious problem occurs when cathodically impressed or galvanically-induced currents generate atomic (nascent) hydrogen directly on the surface of the titanium metal (be it pure metal or alloy counterpart) [9].

Careful laboratory investigations and experiments have demonstrated the following three conditions to exist simultaneously for the purpose of hydriding the unalloyed titanium [9]:

1. pH of the solution is less than 3, the metal surface is damaged by abrasion, or the impressed potentials are more negative than -0.7V.
2. The temperature is above 170°F (77°C) or else only surface hydride films will tend to form, which do not adversely affect the properties of the base metal. The occurrence of failure due to hydriding is rarely encountered below this temperature.
3. There must be a mechanism for generating hydrogen. This may be through the following mechanisms: (i) galvanic couple, (ii) cathodic protection by impressed current, (iii) corrosion of titanium, and (iv) dynamic abrasion of the surface with sufficient intensity to depress the metal potential below that required for the spontaneous evolution of hydrogen.

Most of the hydriding related failures experienced by the titanium metal that have occurred while in service can be explained on this basis [29-31]. Hydriding can be either avoided or retarded by altering at least one of the three conditions listed above.

Titanium and its alloys are considered to be reasonably resistant to chemical attack. However, when exposed to a hydrogen-containing environment, both hydrogen cracking and hydrogen-induced secondary phase formation may occur. For example, Tal-Gutelmacher and Eliezer in their independent study [18] found that the fully-lamellar microstructure almost always had a tendency for higher hydrogen absorption when compared to the alloys having a duplex (i.e., α+β) microstructure. The hydrogen-induced damage experienced by both pure titanium metal and its alloy counterparts was characterized by a noticeable loss of ductility coupled with a concurrent reduction in the stress-intensity threshold for crack propagation. The presence of significant amounts of the β-phase coupled with the formation and presence of the brittle titanium hydride phases resulted in severe degradation of both the mechanical and fracture behavior of the chosen alloys. These researchers also observed that upon exposure to an electrochemical hydrogen environment, strain was induced in both the as-fabricated and/or as-received specimens and the aged counterpart [23].Their study provided the following useful information [23]:

1. Due to its affinity for hydrogen, the occurrence of hydrogen-induced cracking in titanium was observed upon exposure to a hydrogen-containing environment.
2. The key mechanism that governed hydrogen-induced cracking was the formation and presence of brittle titanium hydride phases.
3. For the case of the widely preferred, chosen and used Ti-6Al-4V alloy, the severity of hydrogen-induced cracking depended on the amount of β-phase present in the microstructure.

5. CREVICE CORROSION OF SIMILAR AND DISSIMILAR COUPLING OF TITANIUM AND ITS ALLOYS

In this section, the key and relevant findings from a few studies conducted by others on crevice corrosion are briefly summarized.

5.1 Corrosion of Metal Crevices in the Engineered Barrier System of a Potential Nuclear Waste Repository

Crevice corrosion is favored to occur when the corrosion potential (E_{corr}) exceeds the repassivation potential for crevice corrosion (E_{rcrev}). The purpose of research done by He and co-workers [14] was to evaluate the specific role of both similar and dissimilar metal-to-metal crevices on the corrosion behavior of: (i) Type 316L stainless steel, (ii) Titanium Grade 7, (iii) mill-annealed Alloy 22, and (iv) welded plus solution annealed Alloy 22, under simulated environmental conditions.

In the test assembly, the crevice specimen was sandwiched between two serrated washers, a bolt, and a nut. The crevice specimen was machined from a certain metal, while the serrated washers, bolt, and nut were machined from a dissimilar metal. The initiation of crevice corrosion and propagation occurred by galvanically coupling the crevice specimen to either an alloy (referred to in this study as Alloy 22) or titanium (Grade 7) plate. After adequate time for the propagation of corrosion, these researchers determined the following:

(i) Initiation of crevice corrosion did not occur under the coupling, and
(ii) Initiation of crevice corrosion did not occur even after the addition of a corrosion inducer.

In a companion experiment, the crevice specimen was machined from a welded plus solution annealed alloy (Alloy 22) and titanium (Grade 7) was used as the coupling plate. No crevice corrosion was evident in either of the two specimens.

5.2 Monitoring of Crevice Corrosion in Titanium and its Alloys Using Microelectrodes

Both titanium and its alloys are highly resistant to corrosion primarily because of the tendency to form surface oxide films. For this specific reason, both pure titanium metal and its alloy counterparts are frequently chosen for use in industrial and emerging biomedical applications. However, like most metals, titanium eventually becomes susceptible to crevice corrosion when exposed to environments spanning a range of aggressiveness. Other key factors that exert an influence on crevice corrosion are: (i) temperature, (ii) solution chemistry, and (iii) pH of the solution. Therefore, mechanistic aspects of crevice corrosion in both high chloride-containing and temperature-related conditions were studied by the careful measurement of crevice pH, crevice potential, crevice current, and chloride-ion concentration within a crevice of the titanium metal [16].

Upon successful completion of several monitoring experiments, the tests clearly revealed that the initiation or onset of crevice corrosion in titanium occurred at around 100°C. This initiation was ascribed to a ‘local’ increase in chloride ion content coupled with a concurrent decrease in pH within the crevice as a function of time. Continuation of the crevice corrosion was facilitated by the formation and presence of acidic ions in the crevice of the titanium metal. For the case of pure titanium, the acidity of the crevice environment was found to be high. However, presence of trace amounts of molybdenum in the titanium enables the acidity in the “local” environment to drop due to the creation and presence of a passive film immediately around the crevice. Therefore, the crevice corrosion resistance of a titanium alloy that contained molybdenum was found to be noticeably superior to the crevice corrosion resistance of pure titanium metal.

5.3 Corrosion Behavior of Titanium-Clad Carbon Steel in Weak Alkaline Solutions

Since titanium is well noted for its high corrosion resistance, it can be safely used as a material for a container, which has to hold a high-level radioactive nuclear waste for prolonged period of time.

Pure titanium metal is noted for its ability to offer a high resistance to corrosion since its surface oxide layer is chemically stable. Once the surface of the titanium metal is damaged, an oxide layer tends to form both at and immediately around the damaged area thereby protecting the base metal from the oxygen-containing environment. Researchers have measured the polarization curves for titanium, carbon steel, and titanium-clad carbon steel, which were placed in three different solutions: (a) bentonite-contact solution, (b) sodium sulfate solution, and (c) borate solution [11]. These three solutions were chosen for the purpose of testing primarily because each is representative of environmental concern for exacerbating the initiation and continued occurrence of corrosion.

The researchers used titanium (Grade 2), carbon steel, and titanium-clad carbon steel fabricated using the technique of explosive welding. Optical microscope images of the surface were taken of each of the chosen test specimens. It was observed that the specimens immersed in the solutions containing sulphate ions (SO_4) were partially covered with rust (a corrosion product), while test specimens that were immersed in the borate solution revealed no visible change. The amount of corrosion product that formed on the test specimen when exposed to the solution at 353 K was noticeably more than the amount of corrosion product that formed on the specimen surface when exposed to the same solution at ambient temperature (298 K). Upon careful removal of the corrosion products from the surfaces of the exposed specimens, it was observed that the depth of corrosion was not uniform. Also, it was observed that the corrosion loss on steel side of the titanium-clad specimen was noticeably larger than the loss due to corrosion experienced by the steel specimen. These researchers also observed that the steel side of the titanium-clad steel specimen when exposed to the SO_4 solution did undergo corrosion, but the same side did not significantly corrode when placed in a solution containing borate solution under open circuit conditions. Also, in the SO_4–containing solution, the titanium side of a titanium-clad specimen is cathodically polarized. Therefore, a ‘local’ bimetallic corrosion condition is conducive for accelerating corrosion on the steel side.

5.4 Corrosion and Micro structural Aspects of Dissimilar Joints of Titanium and Type 304L Stainless Steel

Several processes for the joining of dissimilar metals, such as 304L stainless steel and Titanium Grade 2, in an attempt to produce joints having adequate strength, ductility, and corrosion resistance have also been examined [20]. In this specific study, the researchers did make an attempt to investigate whether titanium could be used to construct the electrolytic dissolver unit, while 304L stainless steel could be safely used for components of the nuclear fuel-reprocessing plant. Since 304L stainless steel yields unacceptably high corrosion rates in the chosen environment, these researchers opted to choose titanium as the material for the purpose of construction primarily because it has shown acceptably low corrosion rates under these conditions. A high corrosion resistance in a severely corrosive environment coupled with adequate mechanical strength and ductility were the minimum requirements [20].

Considering both the size and geometry of the mechanical setup it was found that solid-state welding processes, such as: (a) friction welding, and (b) explosive welding, could be safely considered for the joining of 304L stainless steel with titanium [20]. Once the dissimilar metals were joined, a three-phase corrosion test was conducted in an environment of boiling nitric acid for test specimens created using the two welding processes. These experiments essentially involved exposing the chosen metals to the liquid, condensate, and vapor phases of nitric acid for time periods of 48 hours. Upon completion of the exposure to the environment, the corrosion rates in each of the three phases were measured. It was observed that the corrosion rates in the condensate phase were noticeably higher than in the liquid and vapor phases for both the friction welded joint

and the explosive bonded joint. The corrosion rate for the friction welded joint was found to be acceptable. However, the corrosion attack was noticeably significant at the joint interface. For the explosive bonded joint, the corrosion rate was found to be acceptable because all of the corrosion attack took place on the stainless steel portion of the joint. Based on an extensive investigation, and additionally considering corrosion resistance to be the most critical requirement, the explosive bonded joint between titanium and 304L stainless steel was validated for connecting these two dissimilar metals.

5.5 Joining of Titanium/Stainless Steel by Explosive Welding and Effect on Interface

Titanium clad steel is currently gaining acceptance and is being chosen for use in components that are exposed to environments having a range of aggressiveness. Since information pertaining to explosively welded Ti-6Al-4V to stainless steel and their corrosive behavior is lacking, the goal of the study was to examine the metallurgical properties and corrosion patterns occurring at the interfaces when joining titanium to steel.

Once the Ti-6Al-4V and stainless steel were explosively welded, the resultant titanium clad samples measuring 15mm x 15mm were held in a 3.5% NaCl solution for time duration of (i) 672 hours, (ii) 1344 hours, and (iii) 2016 hours. For each test, the weight loss or gain experienced by the test samples was determined to a precision of 1/10,000. It was observed that the mass of the test sample increased with time of exposure to the environment for both the original and titanium clad plates. Also, mass of the titanium clad plate rose quickly up to 1344 hours of exposure to the environment, while mass of the welded plates rose at a slower rate from 1344 hour to 2016 hour of exposure to the environment.

The rate of mass increase gradually slowed primarily because the surfaces of both metals were initially clean at the beginning of the corrosion tests. Consequently, the oxide layer that formed on the surfaces grew rapidly during the preliminary stages of exposure to the environment and resultant degradation due to corrosion. Therefore, the corrosion rate of titanium clad stainless steel specimens was comparatively large during the initial stage of the test, but gradually decreased with an increase in exposure time to the environment.

6. EXPERIMENTAL EVALUATION OF GALVANIC CORROSION

An experimental research effort was conducted in this study for the purpose of evaluating the existence of galvanic effects between steel and titanium. Steel and copper galvanic action was included as a reference system. Tests were performed on three different test specimen combinations. The corrosion rates experienced by the test specimens were determined from these tests so as to establish the following: (a) a test procedure, and (b) a benchmark performance measure, for continuing studies in the subsequent phase of this project.

6.1 Materials

Copper was chosen to be the reference metal in the galvanic corrosion experiments primarily because of strong, detrimental galvanic effects on steel. The copper chosen was high-strength copper (Alloy 182), which is also known as RMA Class 2 chromium-copper. High-strength copper is stronger, harder, and more resistant to wear than pure copper. This copper alloy is often chosen for use in industrial applications including mold making, cable shields, and welding electrodes and is commercially available. The Ti-6Al-4V alloy was chosen for use in the experiments. This alloy was provided by Allegheny Technologies Inc., (ATI Wah Chang, based in

Albany, OR) in the form of plates in the size 0.25 in (thickness) x 12 inch (width) x 36 in (length). The chemical composition of the alloy is given in Table 2. The third metal used in the experiments was steel, whose chemical composition is given in Table 3. Other physical and mechanical properties related to the test plates are given in Tables 4 and 5.

Table 2. Nominal Expected Chemical Composition of Ti-6Al-4V (in weight percent)

Material	Ti	Al	N	V	C	Fe	H	O
Ti-6Al-4V	90.0	6.0	0.05	4.0	0.1	0.4	0.02	0.20

Table 3. Chemical Composition (in weight %) of Experimental Steel

Iron	Fe	Balance
Carbon	C	0.50
Manganese	Mn	0.69
Phosphorus	P	0.016
Sulfur	S	0.008
Silicon	Si	0.44
Chromium	Cr	3.15
Nickel	Ni	0.10
Molybdenum	Mo	1.45
Columbium	Cb	0.005
Aluminum	Al	0.008
Copper	Cu	0.13
Vanadium	V	0.03
Titanium	Ti	0.001

Table 4. Summary of Relevant Mechanical Properties of the Chosen Materials

Material	Orientation	Elastic Modulus		Yield Strength		UTS		Elongation GL=0.5" (%)	Reduction in Area (%)	Tensile Ductility $\ln(A_o/A_f)$ (%)
		msi	GPa	ksi	MPa	Ksi	MPa			
Ti-6Al-4V	Longitudinal	18	126	137	948	154	1060	7.8	23.8	27.0
	Transverse	20	137	152	1047	171	1181	11.5	21.7	25.0
Commercially Pure (Grade 2)	Longitudinal	16	115	63	431	81	561	14.7	43.4	57.0
	Transverse	15	108	55	381	67	465	18.9	47.0	63.0

Table 5. Summary of Relevant Physical Properties of the Chosen Materials

Material	Density gm/cc	Coefficient of Thermal Expansion per degree C	Poisson's Ratio	Shear Modulus	Flexural Toughness
Ti-6Al-4V Titanium Alloy	4.42	8.8 to 9.2 x 10^{-6}	0.29 to 0.39	41 GPa	40 to 60%
Commercially Pure Titanium	4.5	8.6 to 9.2 x 10^{-6}	0.29 to 0.39	41 GPa	70% or more

6.2 The Test Specimen and Experimental Procedures

Three different test specimen combinations were used during the galvanic corrosion experiments:
(a) Titanium alloy and Steel
(b) Titanium alloy and Copper
(c) Copper and Steel

Copper was used as a reference to facilitate comparison with titanium. For each combination of the chosen test specimens, the cathode surface area measured 23.25 in^2, while the anode surface area measured 1.375 in^2, resulting in a cathode to anode surface area ratio of 17:1. The electrolyte used was 5 M NaCl solution at ambient temperature (298 K). The test setup is shown in Figure 3.

Figure 3. The Experimental Setup for Conducting Galvanic Corrosion Tests

Each galvanic corrosion test was run for 24 hours and the potential (V) and current (A) recorded at periodic intervals. Two experiments were performed for each of the three combinations of test materials chosen. Faraday's Law was used to calculate the corrosion rate (mils per year) for each galvanic corrosion experiment. According to this law, the corrosion rate (mpy) is determined using the expression:

$$Corrosion\ Rate\ (mpy) = \frac{0.13\ Icorr\ (E.W.)}{d}$$

In this expression, I_{corr} is the corrosion current density, *(E.W.)* is the equivalent weight in grams/equivalent, *d* is the density, and the corrosion rate constant is taken to be 0.13 derived based on milli-inches (amp-cm-year). The resulting corrosion rate works out to be in mils per year (0.001 inch per year) when this expression is used.

Prior to the initiation of the galvanic corrosion tests, the test specimens were mechanically ground on progressively finer grades of silicon carbide (SiC) impregnated emery paper using copious amounts of water both as coolant and lubricant. For the titanium and copper specimens, 240-grit, 400-grit, and 600-grit SiC impregnated emery paper was used for mechanical grinding and polishing. The same combination along with 1200-grit emery paper was used for the steel specimen. Each specimen was initially wet ground on all six faces until a mirror-like surface finish was obtained. The polished specimens were then cleaned using methanol with subsequent immersion in an ultrasonic cleaner. The polished and cleaned surfaces were then rinsed in de-ionized water prior to the initiation of exposure to the chosen environment.

The galvanic corrosion tests were conducted in a 2 liter glass test cell. The reference electrode was a saturated calomel electrode (SCE). In order to saturate the 5M NaCl solution with air, an air bubble machine was used in the experiment. A glass tube was connected to the gas wash bottle. Subsequently, the gas wash bottle was connected to the air bubble machine.

Prior to initiation of the galvanic test, the open circuit potentials (OCP) were measured on both electrodes. During the galvanic corrosion tests, the combined potential and galvanic current were both recorded using a potentiostat meter [Gamry PC4/750].

6.3 Results and Discussion

The test results are summarized in Table 6. Variation of the potential with time for the galvanic combination of titanium and steel for time duration of 24 hours is shown in Figure 4. The corresponding variation of galvanic current density with time is shown in Figure 5. The corrosion process for steel can be expressed as:

$$Fe = Fe^{2+} + 2e-$$

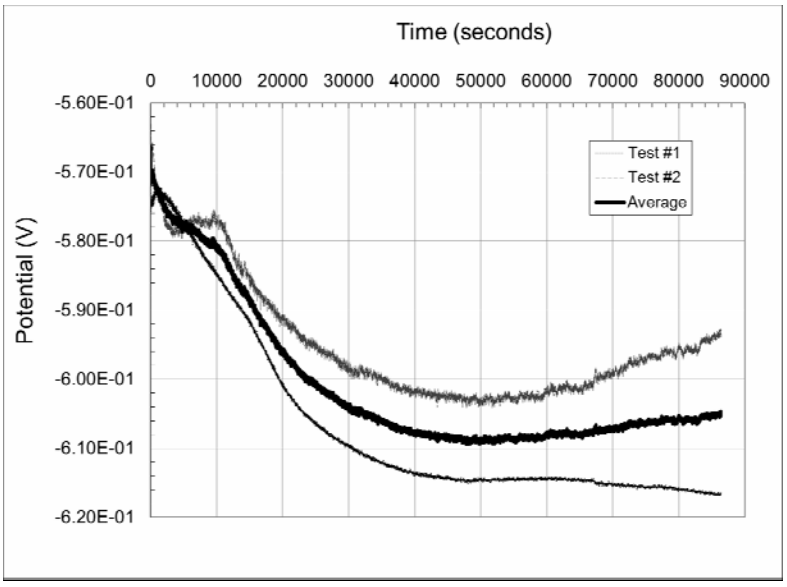

Figure 4. Potential Changes with Time for the Titanium-steel Galvanic Couple

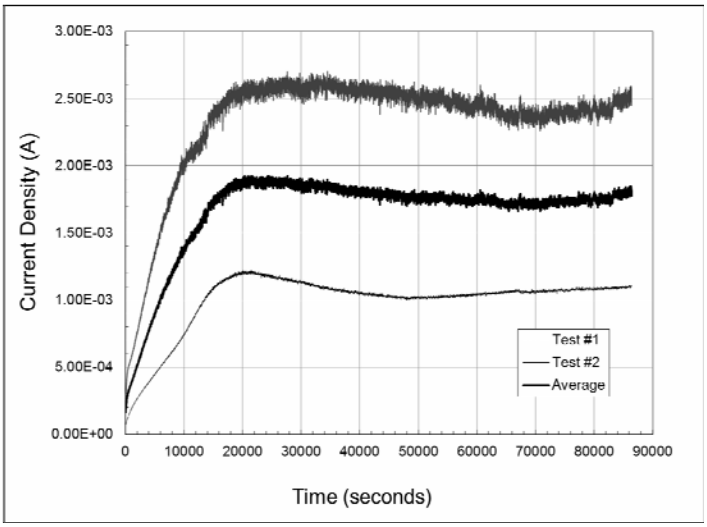

Figure 5. Readings of Current Density as a Function of Time
for the Titanium-steel Galvanic Corrosion Tests

Table 6. Corrosion Rate in mils (Thousandths of an Inch) per Year

Titanium and Steel	
Test #1	Test #2
78.8	177.6
Average:	128

Titanium and Copper	
Test #1	Test #2
2.3	1.4
Average:	2

Copper and Steel	
Test #1	Test #2
163.4	177.6
Average:	171

Assuming the initiation and progression of corrosion to occur uniformly, the corrosion rate (mils per year) can be estimated using Faraday's law.

Since occurrence of galvanic corrosion between the titanium gusset plates and connecting members made of steel could be an issue, the galvanic corrosion tests were performed in order to effectively determine if future testing was needed. Copper was used as the reference metal. After performing two sets of galvanic corrosion tests for each of the three metal combinations chosen, the following are the key findings:

1. Even though titanium is more noble (greater positive potential) than copper in the galvanic series, the galvanic current of the titanium/steel couple is noticeably smaller than the copper/steel couple. This indicates that titanium is more readily polarized and has smaller cathodic reaction kinetics, with a concomitant reduction in the galvanic effect when compared to that of the copper/steel couple.
2. On account of titanium being more noble than copper, the galvanic effect between Ti/Cu was found to be negligible as shown in Table 6.
3. In addition to the potential difference in the galvanic series, the nature and kinetics of the reactions occurring on the surfaces of the two metals is a critical factor in controlling the galvanic effect of the two different metals.

Additional testing is planned for the near future with the prime objective of both developing and consolidating the key strategies to study galvanic corrosion of titanium and steel. The preliminary tests reported in this paper have formed the basis for continued tests. Similar tests are also being conducted using both coatings and other isolating films in order to develop a cost-effective solution for the joining of titanium and steel.

7. CONCLUSIONS

The use of titanium alloys on a steel structure is feasible provided steps are taken to limit the exposure of steel to galvanic corrosion. A careful selection of the bolt materials when using titanium gusset plates will be essential to ensure integrity of the structure when exposed to a corrosive environment. Additional corrosion protection can be gained by the isolation of titanium/steel joints from the environment through the application and maintenance of an impermeable paint or physical barriers. Every research endeavor involving the use of a titanium/steel couple will present unique environmental conditions, and the specific decision regarding protection against galvanic corrosion should be made on a case-by-case basis depending on both nature of the environment and service requirements of the structure. In this paper is presented and discussed the key findings from an experimental study that evaluated the galvanic corrosion of titanium and steel couple.

ACKNOWLEDGMENT

This work is associated with NCERCAMP at The University of Akron and in participation with the DoD University Corrosion Collaboration supported by the U.S. Department of Defense Office of Corrosion Policy and Oversight. The overall research program was administered by the US Air Force Academy under agreement number FA7000-10-2-0013.

REFERENCES

[1] ASCE Report Card, "The 2013 Report Card for America's Infrastructure", American Society of Civil Engineers, March 2013.

[2] Patnaik, A.K., and Srivatsan, T.S., "A Study Aimed at Evaluating, Understanding, and Rationalizing the Strength, Endurance and Performance of Structures Made from Titanium and Titanium Alloy", Final Report, submitted to US Army ARDEC, Picatinny Arsenal, Oct. 2009, 256 pages.

[3] Patnaik, A.K., Poondla, N., Menzemer, C.C., Srivatsan, T.S., "Understanding the mechanical response of built-up welded beams made from commercially pure titanium and a titanium alloy", Materials Science & Engineering: A, Volume 590, 10 January 2014, pp. 390-400.

[4] Patnaik, A.K., Poondla, N., Bathini, U., and Srivatsan, T.S., "On the Use of Gas Metal Arc Welding for Manufacture of Beams of Commercially Pure Titanium and a Titanium Alloy", Materials and Manufacturing Processes, Volume 26, Issue 2, 2011, Pages 311-318.

[5] Patnaik, A.K., Poondla, N., Bathini, U., and Srivatsan, T.S., "Fatigue Behavior of Built-up Welded Beams of Commercially Pure Titanium", Journal of Materials Engineering and Performance, Vol. 20, No. 7, Oct. 2011, pp. 1247-1255.

[6] Menzemer, C.C., Srivatsan, T.S., and Patnaik, A.K., "Studies on the Use of Non-Corrosive Titanium Gusset Plates to Mitigate Bridge Collapses", Final Report Submitted to US Army ARDEC, Picatinny Arsenal, July 2011, 101 pages.

[7] Tinl, N., Menzemer, C.C., Patnaik, A., and Srivatsan, T.S., "The Bolt Bearing Response and Tensile Deformation Capacity of Plates Made from a Titanium Alloy", Journal of Materials Engineering and Performance, August 2012, Volume 21(8), pp. 1696-1702.

[8] Hurtuk, T., Menzemer, C.C., Patnaik, A., Srivatsan, T.S., Manigandan, K., and Quick, T., "The Quasi Static Deformation, Failure and Fracture Behavior of Titanium Alloy Gusset Plates Containing Bolt Holes", Journal of Materials Engineering and Performance, Volume 21(11) Nov. 2012, pp. 2363-2374.

[9] Timet Report, "The Corrosion Resistance of Titanium,", Titanium Metals Corporation, Timet, Denver, Co, 40 pages, 1997

[10] International Titanium Association, “Why are Marine Engineers Turning to Titanium for Corrosion Resistance ?”, Marine Data Sheet IO301 10/99, ITA Boulder, CO, 2 pages, 1999.
[11] Azumi, K. and Seo, M., “Corrosion Behavior of Titanium-clad Carbon Steel in Weakly Alkaline Solutions” Corrosion Science, 2003, Vol. 45, No. 2, pp. 413-426.
[12] Beidokhti,, B., Koukabi, A.H. and Dolati, A., “Effect of Titanium Addition on the Microstructure and Inclusion Formation in Submerged arc Welded HSLA Pipeline Steel”, Journal of Materials Processing Tech, 2009, Vol. 209, No. 8, pp. 4027-4035.
[13] Essenmacher, D., et al., “Cavitation-Induced Erosion of Ti-6Al-4V”, Metallurgical Transactions A 9.8, 1978, pp. 1069 - 1074.
[14] He, X., Dunn, D.S. and Csontos, A.A., “Corrosion of Similar and Dissimilar Metal Crevices in the Engineered Barrier System of a Potential Nuclear Waste Repository”, Electrochemical Acta, 2007, Vol. 52, No. 27, pp. 7556-7569.
[15] Itoh, Y. and Kim, I., “Accelerated Cyclic Corrosion Testing of Structural Steels and Its Application to Assess Steel Bridge Coatings”, Anti-Corrosion Methods and Materials, Vol. 53, No. 6, pp. 374-381.
[16] Kahraman, N., Gülenç, B. and Findik, F., “Joining of Titanium/Stainless Steel by Explosive Welding and Effect on Interface”, Journal of Materials Processing Tech., 2005, Vol. 169, No .2, pp. 127-133.
[17] Kihira, H., Senuma, T., Tanaka, M., Nishioka, K., Fujii, Y. and Sakata, Y., “A Corrosion Prediction Method for Weathering Steels”, Corrosion Science, 2005, Vol. 47, No. 10, pp. 2377-2390.
[18] Lin, C. and Wang, C., “Correlation between Accelerated Corrosion Tests and Atmospheric Corrosion Tests on Steel”, J. of Applied Electrochemistry, 2005, V. 35, No. 9, pp. 837-843.
[19] Liu, C.C., Ou, C.L. and Shiue, R.K., “The Microstructural Observation and Wettability Study of Brazing Ti-6Al-4V and 304 Stainless Steel using Three Braze Alloys”, Journal of Materials Science, 2002, Vol. 37, No. 11, pp. 2225-2235.
[20] Mudali, U.K., Rao, A., Shanmugam, K., Natarajan, R. and Raj, B., “Corrosion and Microstructural Aspects of Dissimilar Joints of Titanium and Type 304L Stainless Steel”, Journal of Nuclear Materials, 2003, Vol. 321, No. 1, pp. 40-48.
[21] Rajendran, N. and Nishimura, T., “Crevice Corrosion Monitoring of Titanium and Its Alloys using Microelectrodes”, Materials and Corrosion, 2007, Vol. 58, No. 5, pp. 334-339.
[22] Starikov, R.S. and Joakim, N., “Quasi-static Behaviour of Composite Joints with Protruding-head Bolts”, Composite Structures, 2001, Vol. 51, No. 4, pp. 411-425.
[23] Tal-Gutelmacher, E. and Eliezer, D., “Hydrogen Cracking in Titanium Based Alloys”, Journal of Alloys and Compounds, 2005, Vol. 404-406, pp.621-625.
[24] Erb, L., “Corrosion Control – Galvanic Table”, An On-line Resource, 2010.
[25] Mansfeld, F., “Galvanic Corrosion of A1 Alloys”, Werkstoffe und Korrosion 25, Jahrg. Heft 8/1974, pp. 578-586.
[26] Vargel, C., “Corrosion of Aluminium”, Elsevier Ltd., 2004, ISBN 0 08 044495 4.
[27] Shreir, L.L., Jarman, R.A. and Burstein, G., “Corrosion”, Four-Volumes, 3rd Edition, Butterworth Heinemann, 1995.
[28] Richardson, T.J.A. (Ed), “Shreir's Corrosion”, Elsevier Ltd., Amsterdam: Academic Press, 2010.
[29] Covington, L.C., “The Influence of Surface Condition and Environment on the Hydriding of Titanium,” Corrosion, 1979, Vol. 35, No. 8, pp. 378-382.
[30] Satoh, H., Fukuzuka, T., Shimogori, K. and Tanabe, H., “Hydrogen Pickup by Titanium Held Cathodic in Seawater” Paper presented at 2nd International Congress on Hydrogen in Metals, June 6-11, 1977, Paris, France.
[31] Phillips, I.I., Pool, P. and Shreir, L.L., “Hydride Formation During Cathodic Polarization of Ti.-II. Effect of Temperature and pH of Solution on Hydride Growth,” Corrosion Science, 1974, Vol. 14, pp. 533-542.

A COMPARATIVE STUDY ON SQUARE AND CIRCULAR HIGH STRENGTH CONCRETE-FILLED STEEL TUBE COLUMNS

S. Guler [1,*] A. Çopur[2] and M. Aydogan [3]

[1] *PhD, Department of Civil Engineering, Istanbul Technical University, Istanbul, Turkey*
[2] *MSc, Department of Civil Engineering, Istanbul Technical University, Istanbul, Turkey*
[3] *Professor, Department of Civil Engineering, Istanbul Technical University, Istanbul, Turkey*
**(Corresponding author: E-mail: : gulersoner@yandex.com)*

Received: 19 December 2012; Revised: 5 February 2013; Accepted: 28 February 2013

ABSTRACT: This paper investigates the behavior of axially loaded square and circular high strength concrete-filled steel tube (CFST) columns. The effects of steel tube thickness and bond strength between the steel tube and the concrete core on axial load capacity and ductility are studied. The performance indices named ductility index (DI), strength enhancement index (SI) and concrete contribution ratio (CCR) are also evaluated for the square and the circular high strength CFST columns. The experimental results are compared with the values estimated by current design codes such as Eurocode 4 (EC4) and AISC-LRFD (1999). The results show that the difference of the axial load capacity due to loss of bonding is significant for both of the square and the circular high strength CFST columns. However, this difference is equal for both of the square and the circular columns with H/t or D/t smaller than 20. The EC4 design code, contrary to the AISC-LRFD (1999), generally overestimates the axial load capacity of the square and the circular high strength CFST columns.

Keywords: High strength concrete, concrete-filled steel tube stub columns, axial load capacity, D/t ratio, bond effect, design codes, performance indices

1. INTRODUCTION

Concrete-filled steel tube (CFST) columns are widely used in the construction of high-rise buildings, bridges, subway platforms, and barriers. The CFST columns provide excellent static and earthquake-resistant properties such as high strength, high ductility, high stiffness, and large energy-absorption capacity. The CFST columns provide some advantages of both steel and concrete. The steel tube assists to carry the axial load and confines the concrete core. Furthermore, the steel tube annihilates the permanent formwork, which reduces construction time, while the concrete core takes the axial load and avoids or delays local buckling of the steel tube (Lu and Zhao [1]).

Recently, there is an increase in use of high strength concrete (HSC) in major construction projects such as high-rise buildings, offshore oil platforms and bridges. HSC is known as a material that is generally associated with low water to cement ratio, high durability, low permeability and a high compressive strength in the range of over 60 MPa. In the recent years using chemical admixtures and silica fumes that partially replace cement as well as applying improved design methods and mixing techniques allows the engineers to produce concrete with much higher compressive strength. Concrete with a compressive strength over 100 MPa can be easily produced commercially using conventional methods and materials. As a result, today HSC has much better performance compared to normal strength concrete. That is why it is commonly used in the construction practice in many countries all over the world (Shah and Ribakov [2]).

One of the major concerns related to HSC is the need of sufficient confinement. Poisson ratio is slightly less and the amount of shrinkage is higher of HSC compared with low and normal strength concrete. Because of those effects, the confining effect of the steel tube to the high strength concrete is not as much as the low and normal strength concrete. Hence, the difference of the axial

load capacity due to loss of bonding is critical for high strength CFST columns. There are many studies to investigate the bond effect for CFST columns with concrete compressive strength up to 100 MPa. Roeder et al. [3] investigate that the importance of bond stress and interface conditions on the axial load capacities of the circular CFST columns with concrete compressive strength varies from 28.6 MPa to 47.2 MPa. The test results show that the bond capacity, for the circular CFST columns, is smaller with large diameter tubes and large diameter-to thickness (D/t) ratios. An experimental study is conducted on circular high strength CFST columns with cylinder concrete strength of 65 MPa by (Johansson and Gylltoft [4]). The test results imply that the bond strength has no influence on the behavior when the steel and concrete sections are loaded simultaneously. On the contrary, for the columns with the load applied only to the concrete section, the bond strength highly affected the confinement effects and, consequently, the mechanical behavior of the columns. Giakoumelis and Lam [5] examine 15 circular CFST columns with concrete compressive strength of 30, 60, and 85 MPa. Contrary to the results of Johansson and Gylltoft [4], the results reveal that the difference of the axial load capacity due to loss of bonding is negligible for low or normal concrete strength while it is critical for the high strength concrete. The difference of the axial load capacity for the high strength CFST columns is 17%. Although there are lots of studies on CFST columns with concrete compressive strength up to 100 MPa, there still needs further analyses on the CFST columns with concrete strength over 100 MPa. To fill such a gap in the literature, Guler et al. [6] study the bond effect on the behavior of the square high strength CFST columns with concrete compressive strength of 115 MPa depending on the different steel tube thickness. The test results clearly show that the difference of the axial load capacity due to loss of bonding is significant for the square high strength CFST columns. The biggest difference of the axial load capacity is 14% for the square high strength CFST columns with 3 mm steel tube thickness.

1.1 Objective

The first aim of this study is to compare the difference of the axial load capacity due to the bond effect for the square and the circular high strength CFST columns with concrete strength over 100 MPa depending on the different steel tube thickness. Secondly, some important parameters the ductility index (DI), the strength enhancement index (SI) and the concrete contribution ratio (CCR) are compared and evaluated for the square and the circular high strength CFST columns. Finally, the axial load capacities of the high strength CFST columns are compared with the values predicted by the EC4 [7]; the American Institute of Steel Construction- Load Resistance Factor Design AISC-LRFD [8] design codes.

2. EXPERIMENTAL PROGRAM

Totally, 40 the square and the circular high strength CFST columns are tested under monotonic axial compression. The steel tube and the concrete are simultaneously loaded. To achieve this, the steel plates with thickness of 10 mm are welded top and bottom surfaces of the square and the circular CFST columns. The specimens are separated as greased and non-greased specimens to investigate the bond effect depending on the different steel tube thickness. The nominal steel tube thickness of the specimens is selected 3 mm, 4 mm, and 5 mm for the square columns and 3 mm, 4 mm, and 6 mm for the circular ones. The height-to-thickness (H/t) ratio of the square columns and diameter-to-thickness ratio (D/t) ratio of the circular columns vary from 19 to 37.9. All the specimens are 400 mm in length to prevent the slenderness effect and to ensure that the specimens behave as stub columns. A thin layer of non-shrinkage cementitious mortar is poured on the top surface of the concrete to provide the concrete core and the steel tube are loaded simultaneously. All the tests are performed three months after casting of concrete. The square and the circular specimens before concrete-filled are shown in Figure 1.

Figure 1. The Square and Circular Column Specimens before Concrete Filled

2.1 Concrete Properties

A batch of concrete is mixed for this study. The regular CEM I PÇ 42.5R is used as cement material in the mix. Dramix ZP 305 steel fibers with hooked ends are used in the mix at two percent (2%) by volume. The fibers in the mix have a diameter of 0.55 mm, length of 30 mm, and tensile strength of 1100 MPa. Standard cylindrical (150 mm x 300 mm) concrete samples are tested in accordance to Turkish Standard TS EN 206 [9] and TS EN 12390 [10] to determine the compressive strength. The average compressive strengths of the concrete (f_{cm}) at the time of test are 115 MPa for cylindrical samples. Cylindrical samples are tested at a loading rate of 250 kN / min. Water-binder (cement + silica fume) ratio is kept constant at 0.13. The typical mix composition of the high strength concrete is given in Table 1.

Table 1. High Strength Concrete Composition

Mix proportions kg (for 1 m^3 concrete)							
Cement	Siliceous Sand (0.5-2mm)	Siliceous Powder (0-0.5mm)	Silica fume	Super Plasticizer	Water	ZP305 Dramix steel fiber	Total
1000	325	500	250	30	165	160	2430

2.2 Steel Properties

All the steel tubes are manufactured from mild steel. In order to determine the actual material properties, three coupons are cut from each steel tube with different steel tube wall for the square and the circular specimens according to Turkish Standard TS 138 EN 10002 [11]. The average yield stress, tensile strength, and modulus of elasticity for the square and the circular specimens are given in Table 2.

Table 2. The Material Properties of the Steel Tubes Obtained from the Coupon Tests

	f_y (MPa)	**f_u (MPa)**	**E_s (MPa)**
Square 3 mm	300	369	200000
Square 4 mm	304	375	200000
Square 5 mm	310	383	200000
Circular 3 mm	311	400	200000
Circular 4 mm	306	389	200000
Circular 6 mm	314	418	200000

2.3 Test Setup

All the tests are performed at the Istanbul Technical University, Civil Engineering Department in Structure and Earthquake Laboratory. Testing of the square and the circular high strength CFST stub columns are tested using a 5000 kN capacity INSTRON testing machine. Two linear variable differential transducers ($LVDT_s$) are placed at diametrically opposite positions to measure the axial deformation. Four strain gauges are used for each specimen to measure strains at the middle height, two strain gauges at the top and two strain gauges at the bottom. The data is acquired at each 30 kN load until the yield point. After this point, data is sampled at 10 kN intervals. The test setup is shown in Figure 2a, 2b and Figure 3a, 3b.

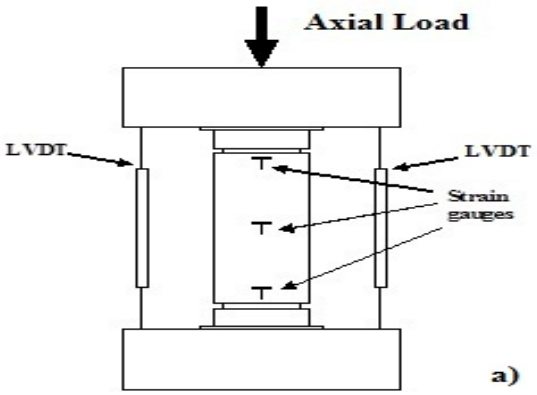

Figure 2a. The Schematic View of Test Set Up

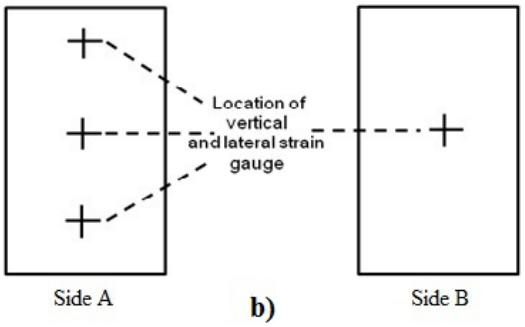

2b. Location of Strain Gauges

Figure 3a. The Test Setup for the Circular Columns

3b. The Test Setup for the Square Columns

The specimens filled with concrete are labeled according to their shape, thickness of steel tube, greased or non-greased and their order. For instance, S3G-1, denotes that the specimen is square (S), the steel tube has a thickness of 3 mm, the specimen is greased (G), and it is the first specimen in this group. Similarly, C5NG-2, denotes that the specimen is circular (C), the steel tube has a thickness of 5 mm, the specimen is non-greased (NG), and it is the second specimen in this group. The square and the circular hollow specimens (unfilled concrete) were labeled similarly except the greased or the non-greased label. The test properties and the axial load capacities (N_{ue}) obtained from the tests of the square and the circular specimens are given in Table 3 and Table 4, respectively.

3. EXPERIMENTAL RESULTS

3.1 Loads versus Axial Shortening

Axial load – axial shortening curves for the square and the circular specimens are shown in Figures 4. As seen in these figures, all the square and the circular high strength CFST columns have no obvious axial shortening during the initial linear elastic period of the loading process, which is the cooperation of steel tube and the concrete core. When the axial load reaches about 90 to 95% of the peak load, the steel tube starts yielding, micro-cracking is initiated and propagated in concrete core, and the local buckling slightly occurs. Therefore, the axial and lateral strains measured at mid-height start to increase notably. The axial load of the square and the circular high strength CFST columns rapidly decrease after the peak load with increased axial shortenings.

As expected, the difference of the axial load capacity is much higher for the circular columns than the square ones with same steel tube wall. However, the difference of the axial load capacity is gradually reduced when the steel tube wall is increased and same for both of the square and the circular high strength CFST columns with H/t or D/t ratio smaller than 20. As seen from Figures 4, it can be clearly said that the bond effect on the axial load capacity is more and more reduced for the square and the circular high strength CFST columns with H/t or D/t ratio smaller than 20. The difference of the average axial load capacity between the greased and the non-greased square and circular high strength CFST columns is shown in Figure 4, Figure 5, and Figure 6.

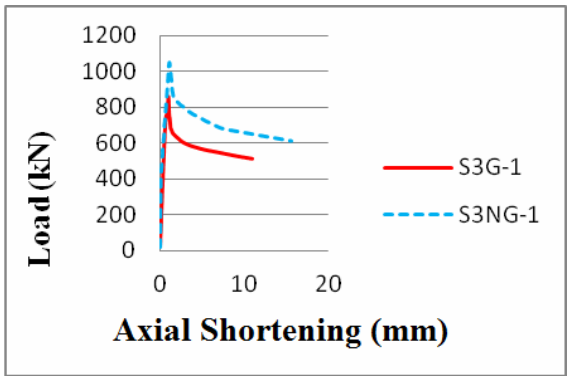

Figure 4a. The Square Columns with 3mm Steel Tube Wall

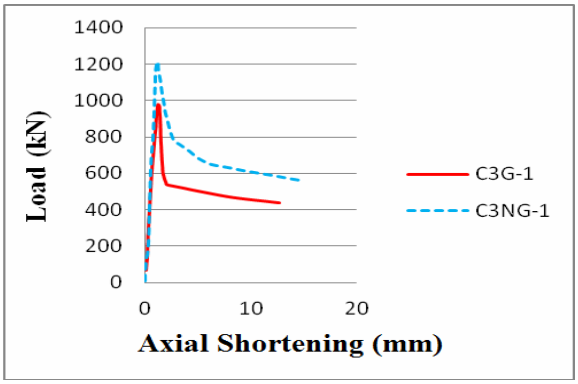

b. The Circular Columns with 3mm Steel Tube Wall

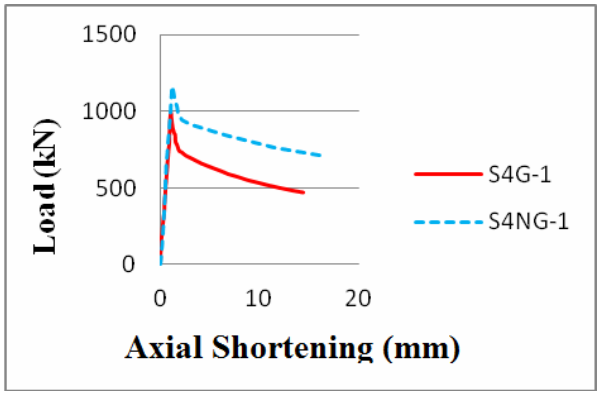

c. The Square Columns with 4 mm Steel Tube Wall

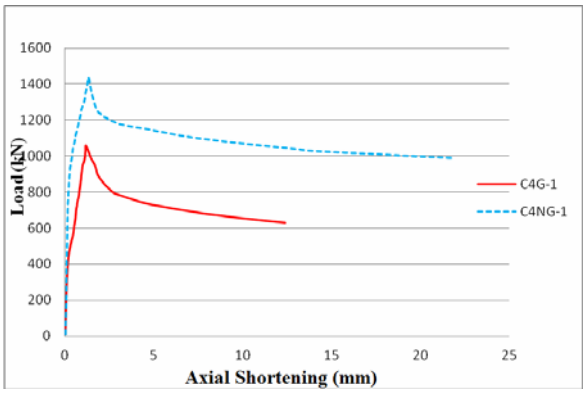

d. The Circular Columns with 4 mm Steel Tube Wall

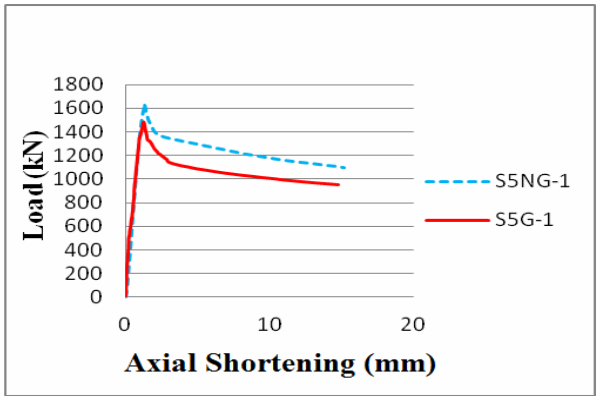

e. The Square Columns with 5 mm Steel Tube Wall

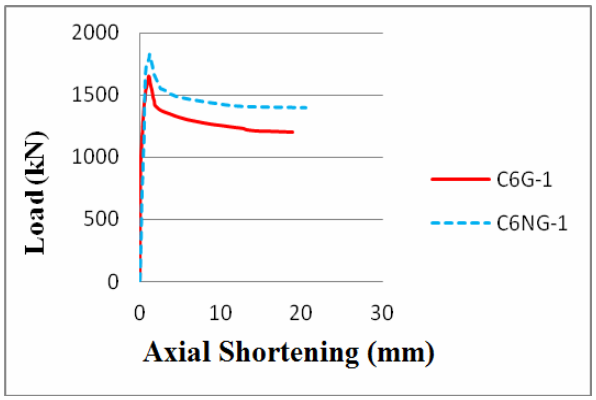

f. The circular columns with 6 mm steel tube wall

Table 3. Measured Square Specimen Results

Specimen	H x B x t (mm)	L (mm)	H/t	f_{cm} (MPa)	f_y (MPa)	A_s (mm^2)	A_c (mm^2)	N_{ue} (kN)
S3G-1	100.08 x 99.86 x 3.01	400	33.2	115	300	1167	8827	856
S3G-2	100.06 x 99.91 x 3.02	400	33.1	115	300	1171	8826	920
S3G-3	100.06 x 99.93 x 3.01	400	33.2	115	300	1168	8831	902
S3NG-1	100.08 x 100.05 x 3.03	400	33	115	300	1176	8837	1049
S3NG-2	100.07 x 100.06 x 3.02	400	33.1	115	300	1172	8841	1017
S3H-1	99.89 x 99.95 x 3.02	400	33.1	-	300	1171	-	295
S3H-2	99.91 x 99.97 x 3.02	400	33.1	-	300	1171	-	322
S4G-1	100.12 x 100.21 x 3.97	400	25.2	115	304	1528	8505	990
S4G-2	100.06 x 100.08 x 3.99	400	25.1	115	304	1533	8481	980
S4NG-1	101.05 x 101.23 x 3.98	400	25.4	115	304	1547	8683	1160
S4NG-2	101.03 x 101.08 x 4.01	400	24.9	115	304	1556	8656	1100
S4H-1	99.96 x 99.87 x 4.02	400	24.9	-	304	1542	-	442
S4H-2	99.95 x 99.84 x 4.01	400	24.9	-	304	1538	-	460
S5G-1	100.02 x 101.04 x 4.98	400	20.1	115	310	1903	8201	1481
S5G-2	100.05 x 101.23 x 4.97	400	20.1	115	310	1902	8226	1474
S5NG-1	100.11 x 100.16 x 5.02	400	19.9	115	310	1910	8117	1642
S5NG-2	100.17 x 100.21 x 4.97	400	20.2	115	310	1893	8145	1636
S5H-1	99.97 x 99.88 x 5.05	400	19.8	-	310	1916	-	685
S5H-2	99.96 x 99.87 x5.02	400	19.9	-	310	1905	-	712

Table 4. Measured Circular Specimen Results

Specimen	D x t (mm)	L (mm)	D/t	f_{cm} (MPa)	f_y (MPa)	A_s (mm^2)	A_c (mm^2)	N_{ue} (kN)
C3G-1	114.24 x 3.02	400	37.8	115	311	1055	9190	980
C3G-2	114.21 x 3.02	400	37.8	115	311	1054	9185	909
C3G-3	114.19 x 3.01	400	37.9	115	311	1051	9185	940
C3NG-1	114.26 x 3.02	400	37.8	115	311	1055	9194	1214
C3NG-2	114.23 x 3.02	400	37.8	115	311	1055	9188	1233
C3H-1	114.21 x 3.03	400	37.7	-	311	1058	-	402
C3H-2	114.24 x 2.99	400	38.2	-	311	1044	-	416
C4G-1	114.18 x 3.98	400	28.6	115	306	1377	8857	1060
C4G-2	114.22 x 3.99	400	28.7	115	306	1381	8860	1221
C4G-3	114.27 x 3.98	400	28.5	115	306	1378	8872	1116
C4NG-1	114.29 x 4.01	400	28.5	115	306	1389	8865	1436
C4NG-2	114.26 x 4.02	400	28.4	115	306	1392	8857	1315
C4NG-3	114.23 x 4.01	400	28.5	115	306	1388	8855	1420
C4H-1	114.27 x 4.02	400	28.4	-	306	1392	-	624
C4H-2	114.25 x 4.01	400	28.5	-	306	1388	-	642
C6G-1	114.21 x 5.99	400	19.1	115	314	2035	8204	1650
C6G-2	114.28 x 5.98	400	19.1	115	314	2034	8219	1615
C6NG-1	114.32 x 5.98	400	19.1	115	314	2034	8225	1830
C6NG-2	114.33 x 5.98	400	19.1	115	314	2035	8226	1810
C6H-1	114.28 x 6.02	400	19	115	314	2046	-	832
C6H-2	114.27 x 6.02	400	19	115	314	2046	-	850

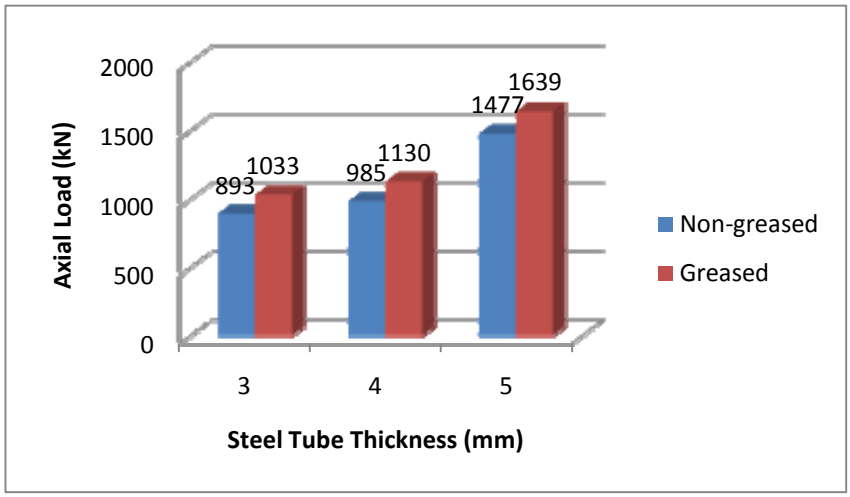

Figure 5. The Difference of the Average Axial Load Capacity for the Greased and the Non-greased Square Specimens

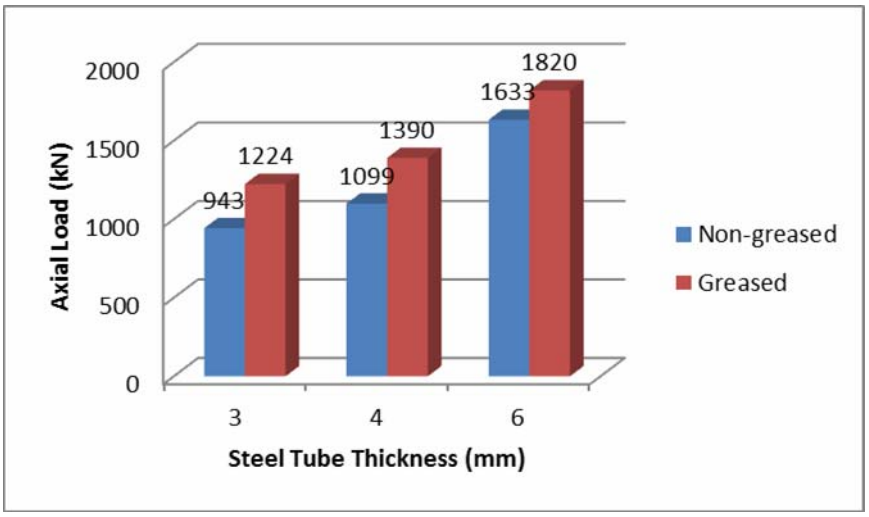

Figure 6. The Difference of the Average Axial Load Capacity for the Greased and the Non-greased Circular Specimens

3.2 Performance Indices

Some important parameters are defined to compare the ductility and the strength enhancement of the CFST columns by Han et al. [12]; and Yang et al. [13]. Those parameters are the ductility index (DI), the strength enhancement index (SI), and the concrete contribution ratio (CCR). They are defined from Eq.1 to Eq.3.

$$DI = \frac{\delta_{85\%}}{\delta_u} \tag{1}$$

$$SI = \frac{N_{u,filled}}{A_s f_y + A_c f_{ck}} \tag{2}$$

$$CCR = \frac{N_{u,\,filled}}{N_{u,hollow}} \tag{3}$$

Here, $N_{u,filled}$ is the ultimate load reached in the tests; $N_{u,\,hollow}$ is the ultimate load of the un-filled steel tubes; δ_u is the axial shortening at the ultimate load; $\delta_{85\%}$ is the axial shortening when the load falls to 85% of the ultimate load; A_s and A_c is the cross-sectional area of the steel tube and the concrete, respectively; f_y and f_{ck} is the yielding stress of the steel tube and the characteristic compressive strength of the concrete, respectively.

The ductility of the specimens is assessed in terms of the ductility index (DI) depicted in Eqn.1. The strength enhancement index (SI) can be described as the ratio the axial load capacity of the composite section to the sum of the strengths of the steel tube and the concrete core. The level of strength enhancement arising from the concrete filling is represented by the CCR that is defined as the ratio the maximum load of composite column to the hollow column. The relationships between the constraining factor and the ductility index, strength enhancement index and the concrete contribution ratio are shown in Figures 6.

As seen from Figures 7 and Table 5, there is a significant increase in the DI when the D/t ratio is reduced for both of the square and the circular CFST columns. However, the increase in the DI is notably higher for the circular CFST columns than the square ones. The average increase in the DI for the square and the circular columns, compared with the 3 mm and 5 mm and 6 mm steel tube wall, is 29% and 63%, respectively. This proves that when the D/t ratio of both of the high strength CFST columns is reduced, the circular high strength CFST columns significantly exhibit more ductile behavior than the square ones after the peak load. Similarly, there is a significant increase in the SI when the H/t or D/t ratio of the square and the circular high strength CFST columns is reduced. However, the increase in the SI is only valid for the square and the circular CFST columns with 5 mm and 6 mm steel tube wall. As seen, there is no any enhancement in the SI for the thinner (3 mm and 4 mm) CFST columns. Compared with the increase in the DI, the increase in the SI is slightly larger for the circular columns than the square ones. The average increase in the SI for the square and the circular high strength CFST columns, compared with the 3 mm and 5 mm or 6 mm steel tube wall, is 38% and 48%, respectively. Contrary to the DI and the SI performance indices, the CCR performance indices that represent the benefit of concrete filling into the hollow steel tube is much more critical for the square high strength CFST columns than the circular ones. The average increase in the CCR for the square and the circular columns, steel tube wall is reduced from 6 mm or 5 mm to 3 mm, 41% and 22%, respectively. This is due to fact that the square hollow steel tubes are more vulnerable to local buckling and has significantly smaller axial load capacities than the circular ones. Furthermore, compared with the same steel tube wall, the non-greased square and the circular CFST columns have higher performance indices than the greased ones due to stronger bond effect between the steel tube and the concrete core.

Table 5. Values of Performance Indices

Specimen	DI	SI	CCR	Specimen	DI	SI	CCR
S3G-1	1.28	0.62	2.74	C3G-1	1.39	0.71	2.08
S3G-2	1.32	0.67	2.95	C3G-2	1.36	0.66	1.93
S3G-3	1.3	0.66	2.89	C3G-3	1.38	0.68	2.00
S3NG-1	1.41	0.77	3.36	C3NG-1	1.42	0.88	2.58
S3NG-2	1.38	0.74	3.26	C3NG-2	1.46	0.89	2.62
S4G-1	1.51	0.69	2.36	C4G-1	1.67	0.74	1.68
S4G-2	1.49	0.68	2.33	C4G-2	1.7	0.85	1.93
S4NG-1	1.61	0.8	2.76	C4G-3	1.69	0.77	1.77
S4NG-2	1.58	0.76	2.62	C4NG-1	1.79	0.99	2.27
S5G-1	1.71	0.98	2.08	C4NG-2	1.81	0.91	2.08
S5G-2	1.69	0.97	2.07	C4NG-3	1.83	0.98	2.25
S5NG-1	1.74	1.09	2.31	C6G-1	2.23	1.05	1.79
S5NG-2	1.78	1.08	2.30	C6G-2	2.21	1.03	1.75
				C6NG-1	2.38	1.17	1.98
				C6NG-2	2.36	1.16	1.96

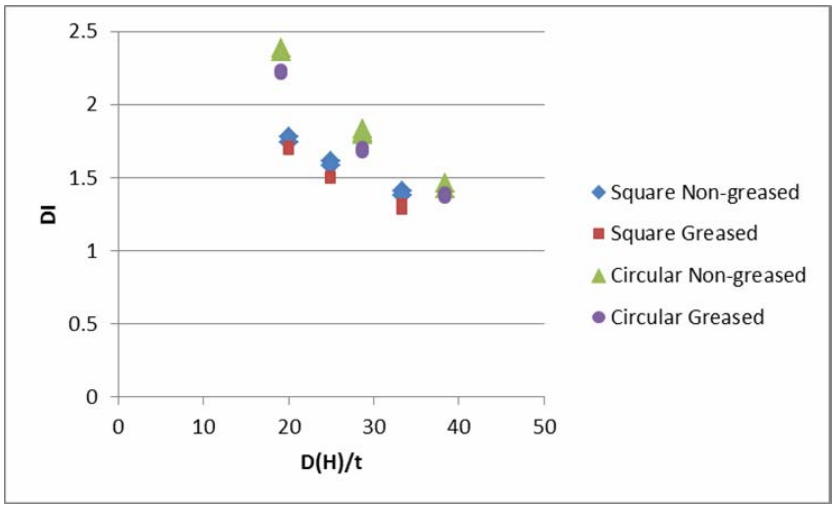

Figure 7a. DI versus D (H)/t Relationship

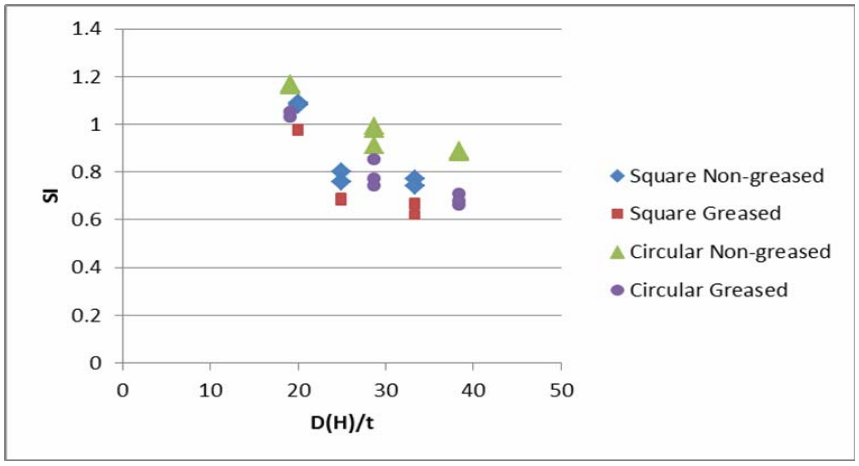

Figure 7b. SI versus D(H)/t Relationship

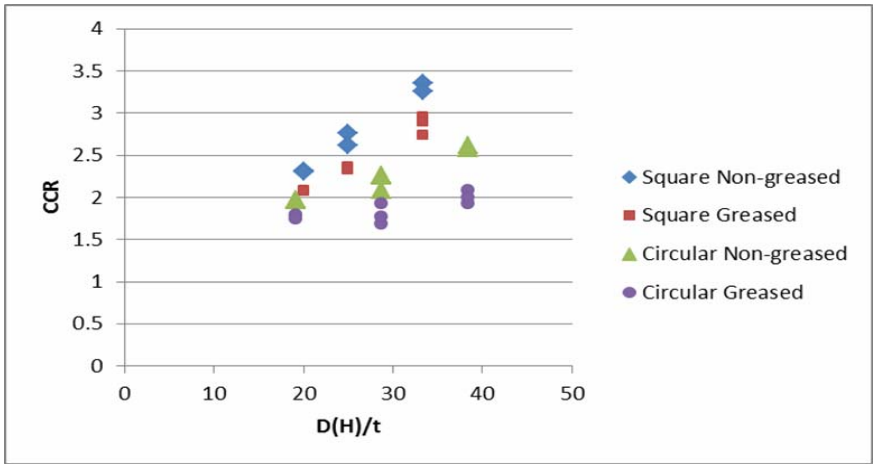

Figure 7c. CCR versus D(H)/t Relationship

4. DESIGN CODES

4.1 Eurocode 4:

The EC4 (2004) design code is the most lately completed international standard in composite construction. EC4 covers concrete encased and partially encased steel sections and concrete- filled sections with or without reinforcement. The EC4 approach is limited to CFST columns with concrete strength of 50 MPa. The axial load capacity of the square CFST columns according to the EC4 is given by Eq. 4:

$$N_{u,EC4} = A_c f_{ck} + A_s f_y \tag{4}$$

The EC4 takes account the confining effect by the steel tube calculating the axial load capacity of the circular CFST columns. If the relative slenderness does not exceed 0.5 and e/D is smaller than 0.1, the axial load capacity of the circular CFST columns can be calculated from Eq.5 to 11:

$$N_{u,EC4} = \left(1 + \eta_c \frac{t}{D} \frac{f_y}{f_{ck}}\right) f_{ck} A_c + \eta_a f_y A_s \tag{5}$$

$$\eta_c = 4.9 - 18.5\lambda + 17\lambda^2 \qquad (\eta_c \geq 0) \tag{6}$$

$$\eta_a = 0.25(3 + 2\lambda) \qquad (\eta_a \leq 1) \tag{7}$$

$$\lambda = \sqrt{\frac{N_{pl,R}}{N_{cr}}} \leq 0.5 \tag{8}$$

$$N_{pl,R} = A_c f_{ck} + A_s f_y \tag{9}$$

$$N_{cr} = \frac{\pi^2 (EI)_e}{l^2} \tag{10}$$

$$(EI)_e = A_s E_s + 0.6 E_{cm} A_c \tag{11}$$

Here, η_c is the coefficient of confinement for the concrete; η_a is the coefficient of confinement for the steel tube; λ is the relative slenderness; l is the buckling length of the CFST column; E_{cm} is the secant elastic modulus of concrete; $(EI)_e$ is the effective flexural stiffness; f_{ck} is the characteristic concrete cylinder strength,; and f_y is the yield strength of the steel.

As seen from Table 6 and Figure 8, although the EC4 overestimate the axial load capacity for the square and the circular high strength CFST columns with thinner steel tube wall (especially nominal D/t or H/t is greater than 33), it can reliably predict the axial load capacity for the square and the circular high strength CFST columns with nominal D/t or H/t ratio smaller than 20. In addition, due to loss of bonding and little confinement by the steel tubes, the axial load capacity of greased the square and the circular high strength CFST columns obtained from test results, compared with the non-greased columns, are lower than the values predicted by the EC4. This difference is much greater for the columns with the thinner steel tube wall than the thicker ones. Furthermore, the EC4 is more conservative for the square high strength CFST columns than the circular ones. This is due to the fact that although the EC4 take account the confinement effect of the steel tube to the concrete core for the circular high strength CFST columns, it doesn't consider the confinement effect for the square ones. The average $N_{ue} / N_{u,EC4}$ for greased the square and the circular CFST columns is 0.75 and 0.62, respectively. In addition, the average $N_{ue} / N_{u,EC4}$ for non-greased the square and the circular columns is 0.87 and 0.79, respectively.

4.2 AISC-LRFD

The axial load capacity of the square and the circular CFST columns according to AISC-LRFD (1999) design code is given from Eq.12 to Eq.16:

$$F_{my} = f_y + 0.85 f_c (A_c / A_s) \tag{12}$$

$$E_m = E_S + 0.4 E_c (A_c / A_s) \tag{13}$$

$$\lambda_c = \frac{KL}{\pi r_m} \sqrt{\frac{F_{my}}{E_m}} \tag{14}$$

$$F_{cr} = 0.658^{\lambda_c^2} F_{my} \tag{15}$$

$$N_u = A_s F_{cr} \tag{16}$$

As seen From Table 6 and Figure 9, it can be said that the AISC-LRFD, similarly EC4, is not safe for the square and the circular columns with the thinner steel tube wall compared to the thicker ones. The average Nue / Nu, AISC-LRFD for the greased square and the circular columns is 0.97 and 1.05, respectively. In addition, the average Nue / Nu, AISC-LRFD for the non-greased square and the circular columns is 1.12 and 1.28, respectively. The axial load capacities obtained from the test results for the square and the circular high strength CFST columns are compared with the values predicted by the EC4 and the AISC-LRFD is given in Table 7, Figure 8, and Figure 9.

Table 6. Comparisons of Axial Load Capacities between Test Results and Design Codes

Specimen No	**$N_{ue\ (kN)}$**	**$N_{ue}/N_{u,\ EC4}$**	**$N_{ue}/N_{u,\ AISC}$**	**Specimen No**	**$N_{ue\ (kN)}$**	**$N_{ue}/N_{u,EC4}$**	**$N_{ue}/N_{u,AISC}$**
S3G-1	856	0.63	0.82	C3G-1	980	0.59	0.93
S3G-2	920	0.67	0.88	C3G-2	909	0.55	0.87
S3G-3	902	0.66	0.87	C3G-3	940	0.56	0.90
S3NG-1	1049	0.77	1.00	C3NG-1	1214	0.73	1.16
S3NG-2	1017	0.74	0.97	C3NG-2	1233	0.74	1.17
S4G-1	990	0.69	0.88	C4G-1	1060	0.59	0.96
S4G-2	980	0.68	0.88	C4G-2	1221	0.68	1.10
S4NG-1	1160	0.79	1.02	C4G-3	1116	0.62	1.01
S4NG-2	1100	0.75	0.97	C4NG-1	1436	0.80	1.29
S5G-1	1481	0.97	1.23	C4NG-2	1315	0.73	1.18
S5G-2	1474	0.96	1.22	C4NG-3	1420	0.79	1.28
S5NG-1	1642	1.08	1.37	C6G-1	1650	0.79	1.32
S5NG-2	1636	1.07	1.37	C6G-2	1615	0.77	1.29
Mean		0.8	1.04	C6NG-1	1830	0.88	1.46
St.Dev.		0.15	0.19	C6NG-2	1810	0.87	1.45
				Mean		0.71	1.16
				St. Dev.		0.11	0.19

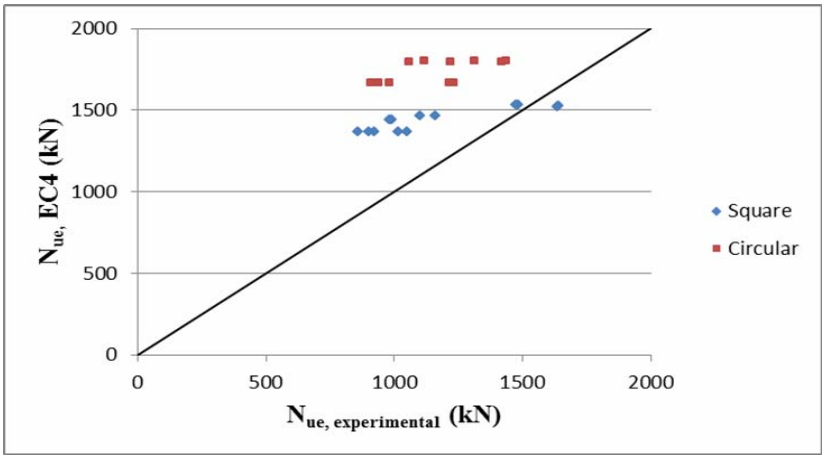

Figure 8. Comparison of test results with EC4

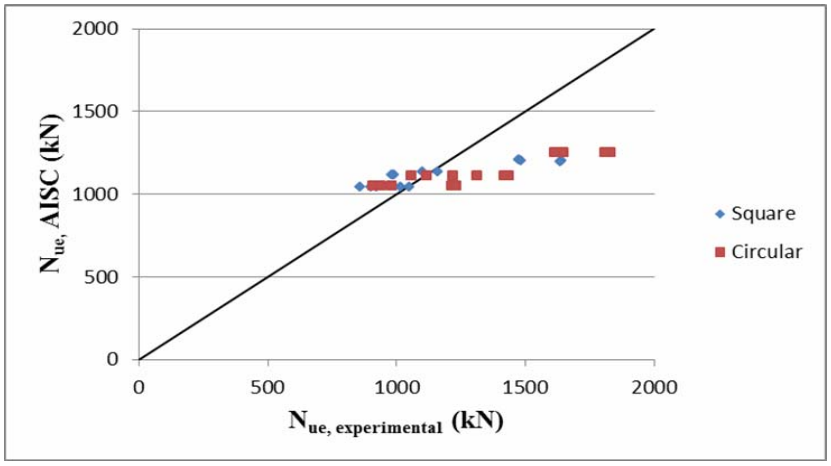

Figure 9. Comparison of Test Results with AISC-LRFD

5. CONCLUSIONS

The present study is an attempt to investigate the bond effect on axial load capacity and performance indices of axially loaded the square and the circular high strength CFST columns with regard to different steel tube thickness. The test results are also compared with the results of present design codes such as the EC4 and the AISC-LRFD. The main conclusions obtained from this study can be drawn as below:

As known, plastic, autogenous, and drying shrinkage of high strength concrete is higher than low and normal strength concrete. As a result of this, the bond stresses between the steel tube and the concrete core is weaker for the high strength CFST columns than the low and normal strength CFST columns. Thus, the reduction on the axial load capacity due to loss of bonding is not negligible for both of the square and the circular high strength CFST columns. Furthermore, the circular high strength CFST columns have higher bond stress capacity than the square ones. As a result of this study, the D (H)/t ratio of 20 may be considered as a separation point for the bond effect on the axial load capacity of the square and the circular high strength CFST columns. The biggest difference of the axial load capacity for the circular and the square high strength CFST columns is 23% and 14%, respectively.

To decrease the D (H)/t ratio significantly improves the ductility performance of the square and the circular high strength CFST columns. However, there is no much benefit to enhance the axial load capacity of the square and the circular high strength CFST columns. Hence, enhancement in ductility is more pronounced than gain in axial load capacity for both of the square and the circular high strength CFST columns. This proves that the square and the circular high strength CFST columns exhibit more ductile behaviour peculiarly after the peak load when the D (H)/t ratio is reduced. The average increase in the DI and the SI performance indices for the square and the circular high strength CFST columns, steel tube wall is increased from 3 mm to 5 mm or 6 mm, is 29% and 63%; 38% and 48%, respectively.

The square hollow steel tubes are much more vulnerable to local buckling and much less confinement effect to the concrete core than the circular ones. Hence, the benefit of concrete filling, as indicated by the CCR, is much more critical for the square sections than the circular ones. The average increase in the CCR for the square and the circular high strength CFST columns, steel tube wall reduced from 6 mm or 5 mm to 3 mm, is 41% and 22%, respectively.

The EC4 design code take into account the confinement effect by the steel tube to the concrete core if the relative slenderness does not exceed 0.5 and e/D is smaller than 0.1. The EC4 approach is limited to CFST columns with concrete strength of 50 MPa. Based on the test results, the EC4 overestimate the axial load capacity of the square and the circular high strength CFST columns. However, when the D (H)/t ratio decrease, the EC4 is more conservative and reliable to predict the axial load capacity of the high strength CFST columns. Besides, due to radial expansion of the concrete and, thus, effective confinement by the steel tube to the concrete core occurs in the circular sections, the EC4 is safer for predicting the axial load capacity of the circular high strength CFST columns than the square ones. Furthermore, the EC4 limitation on concrete cylinder strength cannot be safely extended to concrete compressive strength of over 100 MPa. The EC4 may use a reduction coefficient to consider the weak confinement effect of the steel tube to the concrete core and obtain a better agreement with the test results. The biggest difference between the test results and the EC4 for the square and the circular specimens is 37% and 41%, respectively.

The AISC-LRFD is too conservative for predicting the axial load capacity of the square and the circular high strength CFST columns with D (H)/t ratio smaller than 20. However, the predictions of this design code are not safe when the D (H)/t ratio increase. The biggest difference between test results and the AISC-LRFD design codes for the square and the circular specimens is 37% and 46%, respectively.

REFERENCES

[1] Lu, Z.H. and Zhao, Y.G., “Mechanical Behavior and Ultimate Strength of Circular CFT Columns Subjected to Axial Compression Load”, The 14th World Conference on Earthquake Engineering, Beijing, China, 2008.

[2] Shah, A.A. and Ribakov, Y., “Recent Trends in Steel Fibered High-strength Concrete”, Materials and Design, 2011, Vol. 32, No. 8-9, pp. 412-415.

[3] Roeder, C.W., Cameron, B. and Brown, C.B., “Composite Action in Concrete Filled Tubes”, Journal of Structural Engineering, ASCE, 1998, Vol. 125, No. 5, pp. 477-484.

[4] Johansson, M. and Gylltoft, K., “Mechanical Behavior of Circular Steel-concrete Composite Stub Columns”, Journal of Structural Engineering, ASCE, 2002, Vol. 128, No. 8, pp. 1073-1081.

[5] Giakoumelis, G. and Lam, D., “Axial Capacity of Circular Concrete-filled Tube Columns”, Journal of Constructional Steel Research, 2004, Vol. 60, No. 7, pp.1049-68.

[6] Guler, S., Lale, E. and Aydoğan, M., “Behaviour of SFRC Filled Steel Tube Columns under Axial Load”, International Journal of Advanced Steel Construction, 2013, Vol. 9, No. 1, pp. 14-25

[7] Eurocode 4 “Design of Composite Steel and Concrete Structures, Part 1.1, General R\rules and Rules for Buildings”, EN 1994-1-1, European Committee for Standardization: British Standards Institution, 2004.

[8] American Institute of Steel Construction, AISC, “Load and Resistance Factor Design Specification for Structural Steel Buildings”, American Institute of Steel Construction, Chicago, IL, 1999.

[9] Turkish Standard Institution, TS EN 206. “Concrete-Part 1: Specification, Performance, Production and Conformity”, Ankara,Turkey, 2002.

[10] Turkish Standard Institution, TS EN 12390, “Testing Hardening Concrete- Part 1, Shape, Dimensions and Other Requirements for Specimens and Moulds”, Ankara, Turkey, 2002.

[11] Turkish Standards Institution, TS 138 EN 10002-1, “Metallic Materials – Tensile Testing – Part 1”, Ankara, Turkey, 2004.

[12] Han, L.H., “Tests on Stub Columns of Concrete-filled RHS Sections”, Journal of Constructional Steel Research, 2002, Vol. 58, No. 2, pp. 353-72.

[13] Yang, H., Lam, D. and Gardner, L. “Testing and Analysis of Concrete-filled Elliptical Hollow Sections”, Engineering Structures,2008, Vol. 30, No. 12, pp. 3771-3781.

ORDER FORM

Advanced Steel Construction, an international journal

From: _____

To: ***Secretariat, Advanced Steel Construction, an international journal***
Fax: (852) 2334-6389

I/ We would like to enter a subscription to the ***International Journal of Advanced Steel Construction (IJASC)*** *published by The Hong Kong Institute of Steel Construction.*

Please complete the form and send to:

International Journal of Advanced Steel Construction
c/o Department of Civil and Environmental Engineering
The Hong Kong Polytechnic University
Hunghom, Kowloon, Hong Kong

Fax: (852) 2334-6389 Email: ceslchan@polyu.edu.hk

Published by : The Hong Kong Institute of Steel Construction
Website: http://www.hkisc.org/

Please tick the appropriate box

- ❑ Please enter my subscription **(4 issues per year)**.
- ❑ Please send me a complimentary copy of the *Advanced Steel Construction, an International Journal (IJASC).*

Please tick the appropriate box(es)

	Print only	**On-line only**	**Print & On-line**
Personal	❑ US$ 100	❑ US$ 100	❑ US$ 125
Institutional	❑ US$ 250	❑ US$ 250	❑ US$ 280
Postage	❑ Surface mail	(no charge)	
	❑ Air mail	(US$ 30)	
Total Amount	**US$** _____		

Methods of payment *(please tick the appropriate box(es))*

❑ Please invoice me
❑ Cheque enclosed for US$ _____ payable to
Hong Kong Institute of Steel Construction Limited
(No personal cheque accepted)

Ship to

Name (Prof./ Dr./ Mr./ Ms.) _____
Address _____
_____
_____
City/ State/ Postal Code _____
Country _____
Email _____ Fax _____